

# RECOVERY OF THICKENED KAOLINITE SUSPENSION PROPERTIES THROUGH SHEAR

---

by  
Yijia Sun

A thesis submitted in partial fulfillment of the requirements for the degree of

Master of Science  
in  
Chemical Engineering

Department of Chemical and Materials Engineering  
University of Alberta

# Abstract

The production of a tailings waste stream is ubiquitous to mining and mineral processing operations, especially in Alberta's oil sands industry. Due to the presence of colloidal clays such as kaolinite, which do not naturally sediment in suspension, water recycling and land reclamation remain both a priority and a challenge. To facilitate the separation of fine solids by gravity, tailings are commonly treated with additives to promote the formation of large, fast-settling aggregates. Unfortunately, shearing forces inherent to pipeline transport are known to fracture these aggregates, ultimately reducing the effectiveness of any tailings thickening efforts. However, under certain conditions, aggregates have been observed to re-form after rupture, though the circumstances under which this happens are not well understood. Therefore, the foremost objectives of this study are to determine the suspension conditions which have the greatest impact on the potential for fragmented kaolinite aggregates to re-form, and to establish a connection between suspension rheology and the shear energy required to induce re-aggregation.

A number of re-aggregation experiments were performed to determine the extent of shear-induced re-configuration possible. Kaolinite clay suspensions of varying solids concentration (28 wt% to 42 wt%), thickening additive dosage, and suspension pH (4.3 to 9.8) were sheared using precisely defined protocols in a concentric cylinder rheometer. As fractured aggregate fragments collide, a combination of hydrodynamic and surface forces produce an equilibrium particle agglomerate size. Since the rheological properties of a suspension are strongly dependent on the apparent volume fraction of flocs, monitoring the torque response to constant shear provides insight into the evolution of clay aggregate size. The results established that suspensions with the highest clay solids fraction were the most amenable to re-aggregation, while polymer-dosed suspensions showed the least potential for structural recovery, even at relatively high solids concentration of 40 wt%. Furthermore, it was concluded that the energy input required to induce structural changes in kaolinite aggregates can be inferred from a measurement of the initial suspension rheological properties through a reference point defined as the hysteresis loop closure. Despite differences in initial composition and conditions, this reference point consistently

identified the shear energy necessary to produce the greatest rheological increase in any shear history-dependent kaolinite suspension.

This study establishes a connection between suspension rheology and re-aggregation. It has been shown that previously degraded rheological properties in kaolinite suspensions can be restored by applying the appropriate level of shear in a concentric cylinder rheometer. From these results, it can be inferred that the undesirable rupture of thickened tailings aggregates in pipe flow is possible to reverse under certain conditions. Most importantly, the energy required to produce aggregate restructuring can be determined from a relatively simple bench scale test, and warrants further investigation.

# Preface

This thesis is an original work by Yijia Sun. No part of this thesis has previously been published.

*Dedicated to my parents, Ruijun and Jinghui, and my sister, Gloria,  
for their constant loving support in all my endeavors.*

# Acknowledgements

I am indebted to many people who have assisted me over my academic career, and influenced my life for the better.

I wish to give my utmost gratitude to my supervisor, Dr. Sean Sanders, for his patient guidance, showing me how to conduct research and solve problems, and for providing me with opportunities to develop my own interests and passions. Dr. Sanders demonstrated to me what it means to be a great teacher and mentor, and always challenges me to strive for my full potential.

I am deeply obliged to Dr. David Breakey, for his tireless efforts in support of all facets of my research. David has been a constant source of friendship, wisdom, and advice, and has taught me skills which I will always cherish.

I have much appreciation for the Pipeline Transport Processes research group, which I have had the honour of being a part of. I would like to recognize Ms. Terry Runyon for her administrative expertise and assistance. I am also thankful for the advice and experience shared by my colleagues, especially Maedeh Marefatallah, Ameneh Shokrollahzadeh, César Montilla Perez, Abiodun Olayode, Akash Saxena, Aaron Cheung, and Brad Zhang.

Many thanks to our industrial sponsors, and to the NSERC Industrial Research Chair in Pipeline Transport Processes, whose financial support made this work possible.

All my accomplishments and achievements are owed in some way to my parents Ruijun Sun and Jinghui Shen, and my sister, Gloria, for their limitless encouragement and unconditional love. My profound thanks to Liyuan Feng, who never fails to be the best part of each of my days. Thank you for believing in me even during times when I did not believe in myself.

Finally, I am vastly grateful, of course, to my friends across Canada and beyond. Although we may find ourselves spread around the globe, the ties of camaraderie know no geographical bounds.

# Contents

<b>List of Figures</b>	<b>xi</b>
<b>List of Tables</b>	<b>xiii</b>
<b>List of Symbols</b>	<b>xiv</b>
<b>1 Introduction</b>	<b>1</b>
1.1 Background: Oil Sand Tailings . . . . .	1
1.2 Problem Statement: Challenges in Tailings Management . . . . .	3
1.3 Objectives . . . . .	4
1.4 Thesis Outline . . . . .	4
1.5 Significance of Contributions . . . . .	5
<b>2 Literature Review</b>	<b>7</b>
2.1 Introduction . . . . .	7
2.2 Rheology models and definitions . . . . .	7
2.2.1 Time-independent rheological models . . . . .	8
2.2.2 Time-dependent rheological models . . . . .	9
2.2.3 Rheological hysteresis . . . . .	10
2.3 Mechanisms for Aggregate Formation . . . . .	11
2.3.1 Kaolinite surface charges . . . . .	13
2.3.2 Colloidal forces governing kaolinite particle aggregation . . . . .	14
2.3.3 Aggregate formation through charge neutralization . . . . .	15
2.3.4 Preferred kaolinite structural configuration . . . . .	15
2.3.5 Relationship of aggregate size to rheology . . . . .	16
2.3.6 Aggregate formation through polymer flocculation . . . . .	17
2.4 Tailings Thickening and Degradation . . . . .	17
2.4.1 Sources of shear in pipeline transport . . . . .	18

---

2.4.2	Shear-induced rheology reduction	19
2.5	Shear-Induced Re-aggregation	22
2.6	Concentric Cylinder Rheometry	25
2.7	Complications with Concentric Cylinder Rheometry	27
2.7.1	Onset of Taylor vortices	27
2.7.2	Incomplete shearing of a sample	27
2.7.3	Wall slip	28
2.8	Vane yield stress measurements	29
2.9	Scope of the Current Study	30
<b>3</b>	<b>Experimental Method</b>	<b>32</b>
3.1	Introduction	32
3.2	Materials	33
3.2.1	Kaolinite clay	33
3.2.2	Water and pH adjustment	33
3.2.3	Thickening additives	34
3.3	Equipment	34
3.3.1	Sample Preparation	34
3.3.2	Rheometer	35
3.4	Procedures	36
3.4.1	Experimental conditions investigated	36
3.4.2	Kaolinite suspension preparation	37
3.4.3	Flocculant preparation	38
3.4.4	Flocculated kaolinite suspension preparation	39
3.4.5	Rheological measurements	40
3.4.6	Re-aggregation experiment program	41
3.5	SEM Imaging	41
<b>4</b>	<b>Results and Discussion</b>	<b>43</b>
4.1	Introduction	43
4.2	Kaolinite Suspension Rheology	44
4.2.1	Interpretation of Bingham parameters from rheometer data	44
4.2.2	Impact of suspension variation on Bingham parameters	45
4.3	Shear Stress Hysteresis	48
4.3.1	Hysteresis loop closure	50

---

4.4	Development of Re-aggregation Experiments . . . . .	51
4.4.1	Interval shearing experiments . . . . .	52
4.4.2	Determination of time required for each interval . . . . .	54
4.4.3	Effect of multiple shearing cycles . . . . .	54
4.5	Sources of Error . . . . .	56
4.5.1	Wall slip . . . . .	56
4.5.2	Change in bulk suspension properties over time . . . . .	56
4.6	Shear-Induced Kaolinite Re-aggregation . . . . .	58
4.6.1	Relationship between re-aggregation and energy dissipation rate . . . . .	58
4.6.2	Maximum torque increase achieved through conditioning . . . . .	61
4.6.3	Connection between re-aggregation and rheology . . . . .	63
4.6.4	Application of theory to pipe flow results . . . . .	65
4.7	Summary . . . . .	66
<b>5</b>	<b>Conclusion and Recommendations for Future Work</b>	<b>67</b>
5.1	Conclusions . . . . .	67
5.2	Recommendations for future work . . . . .	69
	<b>References</b>	<b>71</b>
	<b>Appendix A Rheometer calibration data</b>	<b>78</b>
	<b>Appendix B Safe work procedures</b>	<b>79</b>
B.1	Safe Work Procedure for preparing 35 wt% kaolinite suspension . . . . .	80
B.2	Safe Work Procedure for rheometer operation . . . . .	83
	<b>Appendix C Rheological data for tested samples</b>	<b>85</b>
C.1	Raw data for 35 wt% kaolinite suspension, base case . . . . .	86
C.2	Raw data for 28 wt% kaolinite suspension . . . . .	87
C.3	Raw data for 42 wt% kaolinite suspension . . . . .	88
C.4	Raw data for 35 wt% kaolinite suspension, pH = 7.3 . . . . .	89
C.5	Raw data for 35 wt% kaolinite suspension, pH = 9.8 . . . . .	90
C.6	Raw data for 35 wt% kaolinite suspension, no additives . . . . .	91
C.7	Raw data for 40 wt% kaolinite suspension, flocculated . . . . .	92
	<b>Appendix D Rheological variation of sample over testing period</b>	<b>93</b>
D.1	Rheological variation of 35 wt% kaolinite suspension over 2 hours . . . . .	94

<b>Appendix E Sample calculation for energy dissipation in pipeline</b>	<b>96</b>
E.1 Determination of $\epsilon_{HLC}$ from viscometry data . . . . .	96
E.2 Determination of shearing from pipe flow . . . . .	98

# List of Figures

1.1	Generalized schematic for the surface mining of oil sands . . . . .	2
1.2	Qualitative representation of clay aggregate response to shearing. . . . .	3
2.1	Qualitative rheograms for four time-independent rheological models . . . . .	8
2.2	Comparison of Bingham predicted yield stress and actual value. . . . .	9
2.3	Comparison of two time-dependent rheological models with Newtonian behaviour at constant shear rate . . . . .	11
2.4	Shear stress response to increasing, then decreasing shear rate . . . . .	11
2.5	Rheopectic suspension rheogram with hypothesized evolution in microstructure . . . . .	12
2.6	Zeta potential of edge and face surfaces of kaolinite. . . . .	13
2.7	Combination of attractive van der Waals forces and repulsive electric double layer forces collectively describe DLVO theory . . . . .	14
2.8	Preferred orientation of kaolinite aggregate structure at varying ionic concentration and pH . . . . .	16
2.9	Laminar flow of a yield stress fluid. . . . .	19
2.10	Yield stress reduction as a function of energy dissipated for three types of flocculant . . . . .	20
2.11	Use of concentric cylinder viscometer to measure rheology reduction as a function of time . . . . .	21
2.12	Yield stress reduction of two batches of thickened oil sands tailings in viscometer and pipe loop geometries . . . . .	22
2.13	Evolution of particle size distribution due to different levels of shear . . . . .	24
2.14	Side and end views of the key dimensions in a concentric cylinder rheometer with DIN spindle geometry. . . . .	26
2.15	Use of a vane to measure the true yield stress of a fluid. . . . .	29

---

3.1	Experimental procedure flowchart. . . . .	33
3.2	Typical mixing geometry used in the preparation of all kaolinite suspensions. . . . .	35
4.1	Typical rheogram for 35 wt% kaolinite clay. . . . .	45
4.2	Variation of plastic viscosity with changes in suspension conditions. . . . .	46
4.3	Variation of Bingham yield stress with changes in suspension conditions. . . . .	46
4.4	Rheograms for 35 wt%, 42 wt% and pH 9.8 kaolinite suspensions all show a distinct difference in hysteresis. . . . .	49
4.5	Variation of $\epsilon_{HLC}$ with changes in sample conditions. . . . .	51
4.6	Continuous torque increase over time for constant spindle speed for base case 35 wt% kaolinite suspension . . . . .	52
4.7	Typical results from 3-phase interval shearing test . . . . .	52
4.8	Torque decrease over breakdown period with respect to non-dimensionalized energy dissipation, $\epsilon_{HLC}$ . . . . .	53
4.9	Torque increase trends for 35 and 42 wt% suspensions are similar in shape. . . . .	55
4.10	Torque response over repeat intervals of high and low shear. . . . .	55
4.11	Comparison of rheology measurements using smooth and roughened spindles. . . . .	57
4.12	Torque increase as a function of non-dimensionalized energy dissipation rate, $\epsilon_{HLC}$ , for 35 wt% kaolinite suspension. . . . .	59
4.13	SEM characterization shows differences in kaolinite aggregate structure before and after exposure to conditioning shear energy. . . . .	60
4.14	10,000X magnification shows an abundance of face/face particle orientation in small kaolinite flocs following structural breakdown. . . . .	61
4.15	Maximum increase in torque achievable over a 300 second conditioning phase for the conditions tested in this study. . . . .	62
4.16	Comparison of torque increase by shear conditioning at various multiples of $\epsilon_{HLC}$ for all tested sample conditions. . . . .	64
4.17	Multiple of $\epsilon_{HLC}$ required to achieve maximum re-aggregation for all tested sample conditions. . . . .	64
4.18	Continuous increase in pipeline pressure drop observed in pipe flow of concentrated kaolinite mixture. . . . .	65
E.1	Viscometer data at initial mixture conditions. . . . .	97
E.2	Viscometer data after 4 hours pipe loop flow. . . . .	97
E.3	Pipe loop pressure drop data. . . . .	99

# List of Tables

2.1	Common rheological models to illustrate 1-D time-independent fluid behaviour . . . . .	8
3.1	Overhead mixer impeller types and sizes. . . . .	35
3.2	DHR-2 rheometer technical specifications. . . . .	36
3.3	Range of values tested for all experimental parameters. . . . .	37
3.4	Initial impeller speeds to ensure complete mixing, but no vortex formation. . . . .	39
4.1	Torque increase values for 35 and 42 wt% suspensions . . . . .	55
4.2	Comparison of rheological parameters obtained using smooth vs. roughened geometry. . . . .	57
E.1	Haake RV3 viscometer geometry and kaolinite mixture specifications. . . . .	97
E.2	Pipe loop geometry specifications. . . . .	98
E.3	Summary of calculated $\epsilon_{HLC}$ in comparison to pipe loop shearing. . . . .	100

# List of Symbols

Symbol	Description	Units
$C$	Mixing impeller clearance	m
$D$	Mixing impeller diameter	m
$D_V$	Vane diameter	m
$H$	Vane geometry height	m
$H_T$	Mixing tank fluid height	m
$K$	Power law flow consistency index	$\text{Pa}\cdot\text{s}^n$
$L$	Rheometer spindle length	m
$R$	Pipe radius	m
$R_1$	Rheometer spindle radius	m
$R_2$	Rheometer cup radius	m
$T$	Torque	$\text{N}\cdot\text{m}$
$T_T$	Mixing tank diameter	m
$V_c$	Vane constant	$\text{m}^3$
$\dot{W}_l$	Lost power due to friction	W
$\dot{\gamma}$	Shear rate	1/s
$\dot{m}$	Mass flow rate	kg/s
$\ell_w$	Lost work due to friction	J
$\mu$	Viscosity	$\text{Pa}\cdot\text{s}$
$\mu_p$	Viscosity, Bingham plastic	$\text{Pa}\cdot\text{s}$
$\omega$	Rheometer spindle speed	rad/s
$\omega_{crit}$	Rheometer spindle speed, onset of Taylor vortices	rad/s

Symbol	Description	Units
$\phi_F$	Volume fraction, flocs	-
$\rho$	Density	kg/m <sup>3</sup>
$\tau$	Shear stress	Pa
$\tau_B$	Yield stress, Bingham	Pa
$\tau_w$	Wall shear stress	Pa
$\tau_y$	Yield stress, true	Pa
$\tau_{HB}$	Yield stress, Herschel-Bulkley	Pa
$\theta$	Rheometer spindle cone angle	°
$\varepsilon$	Energy dissipation rate	W/kg
$\zeta$	Zeta potential	V
$m$	Mass	kg
$n$	Power law flow behaviour index	-
$r$	Radial position	m
$t$	Time	t

**Acronyms**

AER	Alberta Energy Regulator
DLVO	Derjaguin, Landau, Verwey, Overbeek
EDL	Electric Double Layer
FBRM	Focused Beam Reflectance Measurement
HLC	Hysteresis Loop Closure
MFT	Mature Fine Tailings
OSRIN	Oil Sands Research and Information Network
PAM	Poly-Acrylamide
PBT	Pitched Bladed Turbine
PSV	Primary Separation Vessel
rpm	Rotations Per Minute
SEM	Scanning Electron Microscopy

## LIST OF SYMBOLS

---

Symbol	Description	Units
TMF	Tailings Management Framework	
VDW	van der Waals	

# Chapter 1

## Introduction

### 1.1 Background: Oil Sand Tailings

The province of Alberta, Canada, boasts the third largest natural crude oil reserves in the world [1]. The majority of this crude oil exists in the form of oil sands, and is located in the Athabasca, Peace River, and Cold Lake deposits, with a total of some 165 billion barrels of bitumen in place recoverable by today's technologies [1]. The production of crude oil from these sources was 2.4 million barrels per day in 2016, and projected to grow to 3.7 million barrels per day by 2030 [2]. Although the reserves are vast, and represent a significant contribution to global energy, Canadian oil sands pose certain unique challenges to extraction, production, and especially waste management.

Oil sand deposits which lie less than 75 m below the surface of the earth are available to be mined using industrial sized shovels and trucks [3]. After the oil sand ore is crushed, it is mixed with water and delivered to the bitumen extraction facility using hydrotransport pipelines. It is estimated that nearly 0.5 million tonnes of solids are moved in this manner every day [4]. During hydrotransport, crushed ore is further reduced in size by shear forces, and additives such as sodium hydroxide (NaOH) encourage the liberation of bitumen from the sand grains. [Figure 1.1](#) shows a generalized schematic of the surface mining and bitumen extraction process. At each of the primary and secondary separation stages of bitumen extraction, as well as froth treatment, a waste stream known as tailings is produced. For every barrel (0.159 m<sup>3</sup>) of bitumen extracted from oil sands surface mining,

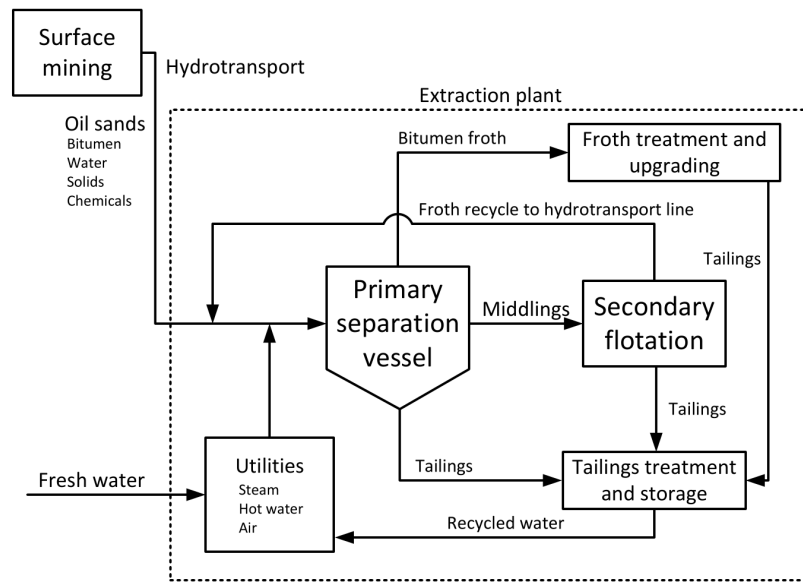


Figure 1.1: Generalized schematic for the surface mining of oil sands. Adapted from Masliyah et al. [5].

3.3 m<sup>3</sup> of tailings waste is generated [5].

Oil sands tailings are composed of water, sand, silts, clays, and unrecovered bitumen, and are collected in massive engineered impoundment areas known as tailings ponds [5, 6]. As of 2013, oil sands tailings ponds in Alberta covered some 220 km<sup>2</sup>, and accounted for over 975 million m<sup>3</sup> of impounded tailings [1]. Although 78-86% of the water used in oil sand mining is recycled [7], an estimated 2.5 m<sup>3</sup> of fresh water is still required in the production of each cubic meter of bitumen [8]. For numerous reasons, oil sand mine operators are strongly motivated to recycle process water from tailings to reduce fresh water draw, and reclaim the land occupied by tailings ponds.

In October 2017, the Alberta Energy Regulator (AER) introduced Directive 85 and the Tailings Management Framework (TMF), which requires tailings producers to ensure all tailings containment dams are ready to be reclaimed within 10 years of an associated project's end [9]. The TMF grants operators the flexibility to define a tailored performance criteria based on deposit characteristics, surrounding landform, and other factors [9]. Finally, from an economic perspective, the potential for rapid separation of solids means warm process water is more readily available to be reused before cooling in outdoor confinement, thereby reducing the emission of greenhouse gases, and the costs associated with heating the recycled water.

## 1.2 Problem Statement: Challenges in Tailings Management

Of the solids species found in tailings, particles less than  $44\ \mu\text{m}$  in diameter are defined as the “fines” fraction, while any solids with greater diameter are referred to as “coarse” particles [10]. Although coarse particles quickly settle, the fines form a stable colloidal system, and do not easily segregate from water by gravity alone. Instead, the fine particles remain as a gel-like suspension with approximately 30 wt% solids called Fluid Fine Tailings (FFT) [5]. The majority of FFT is composed of clays, with kaolinite clay as the main constituent [11–18]. To promote the formation of naturally settling fine particle agglomerates, tailings are treated using a combination of charge neutralizing coagulants and polymer flocculants either using a thickener unit operation, or in-line injection and mixing. Under carefully formulated dosages, these additives have been shown to capture over 99.5% of clay solids, and produce large, fast-settling particle aggregates [19]. However, as shown qualitatively in Figure 1.2A, large volumes of water are trapped in the interstitial spaces between clay particles during flocculation [20]. As the thickened tailings are transported from the treatment facility to the storage area, it is well established that unavoidable pipeline shearing causes the undesired rupture of clay aggregates [21–23] and releases some of the the trapped water [24] (Figure 1.2B). The result is a tailings product which does not meet the intended yield stress specifications, and resources spent on treating tailings are wasted.

In 2012, Gillies et al. [22] showed that the yield stress of polymer flocculated thickened oil sands tailings decreased exponentially when exposed to shear in a pipe loop, reaching

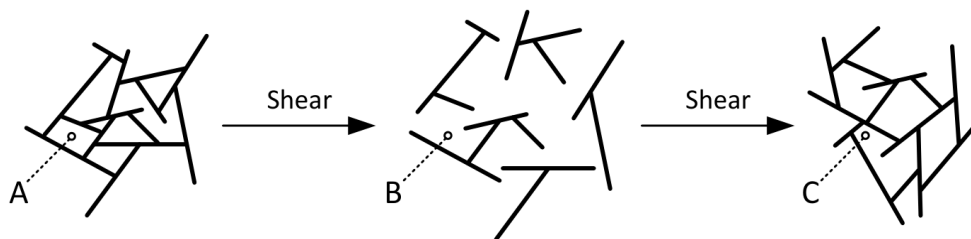


Figure 1.2: Qualitative representation of clay aggregate response to shearing.

- A) Large, porous aggregates trap interstitial water [20].
- B) Aggregate rupture due to shearing, releasing trapped water.
- C) Induced reversal of aggregate rupture.

50% the original value after exposure to a cumulative 1500 kJ per cubic meter of tailings slurry. Other studies on mine tailings demonstrated the rheology reduction is only a function of the energy input, and completely independent of the shear geometry [24, 25]. However, it has also been shown that periods of lower shear can reverse the initial shear-induced degradation of aggregates, and result in structural re-growth for various dilute particulate suspensions [26–28]. This re-aggregation is represented in [Figure 1.2C](#).

### 1.3 Objectives

The ability to reverse shear-induced aggregate breakdown would be highly beneficial to producers of treated oil sand tailings. However, at present, there are no studies which attempt to define the conditions under which aggregate re-growth is induced. Furthermore, a connection should be established between time-dependent rheological behaviour and shearing to structural re-aggregation at the particle scale in thickened tailings suspensions. Previous research has confirmed that the rheological behaviour of a kaolinite suspension is similar to that of oil sands tailings at similar solids mass fractions and surface chemistry [29]. For this reason, the present study uses a concentrated kaolinite suspension as an analog for oil sands tailings. Therefore, the objectives of this study are:

1. To investigate the effect of shearing on the breakdown and re-formation of kaolinite aggregate structure;
2. To establish a connection between kaolinite suspension rheology and shear energy required to reverse the rheology reduction caused by pipeline transport shearing; *and*
3. To determine the effect of varying pH, solids concentration, and coagulant/flocculant dosage on the re-aggregation potential of kaolinite suspensions, as a function of shear energy input.

### 1.4 Thesis Outline

The present study investigates the effect of shearing on kaolinite aggregates, and the potential for clay structures to undergo re-formation and enlargement after their inevitable

and undesired breakage during pipeline transport. This thesis is composed of four chapters, in addition to the current introduction. The literature review ([Chapter 2](#)) summarizes the relevant present understanding in this field of research, and establishes knowledge gaps that the current study will attempt to fill. [Chapter 3](#) provides a detailed explanation of the materials, equipment, and procedures used in this research. Rheometer operation, including technical specification, is also described in this chapter. The results from this study are presented in [Chapter 4](#). The rheological properties of kaolinite clay slurry under various conditions are discussed. The emphasis of this chapter is on the degree to which the rheological properties of the clay suspensions are increased in response to shear. The maximum shear resistance increase is compared at varying clay solids concentrations, suspension pH, coagulant dosages, and with or without polymer flocculant use. The energy requirement to break down the aggregate structures as much as possible is also discussed. The results are shown to be consistently repeatable over multiple runs. The final chapter provides a summary of the key findings in this study. Recommendations for improving the experimental method and expanding this research through future studies bring the thesis to a close.

### **1.5 Significance of Contributions**

The contributions from this thesis can be summarized as follows:

1. Quantifies the changes to aggregate size and resistance to breakage as a result of shearing in kaolinite clay suspensions;
2. Demonstrates the effect of suspension pH, solids concentration, electrolyte addition and flocculant dosage on the potential for kaolinite clay aggregate structure re-growth after breakage; *and*
3. Establishes a link between rheological measurements, shearing, and structural changes in clay particle structure, showing the energy required for both structural strengthening and breakdown in clay suspensions can be predicted as a function of the initial suspension's rheological measurements.

## 1.5. SIGNIFICANCE OF CONTRIBUTIONS

---

Finally, although this work was undertaken in the context of oil sands tailings transport, the findings could have broad implications for other fine particle suspensions exhibiting shear history-dependent characteristics.

## Chapter 2

# Literature Review

### 2.1 Introduction

This chapter summarizes the relevant literature with regards to the behaviour of kaolinite clay aggregates. The review begins with an overview of rheological concepts and definitions, and establishes a foundation on which aggregate suspensions may be characterized. Next, mechanisms for aggregate formation through colloidal force manipulation and mechanical ties are discussed. Understanding the expected configuration of particles under various suspension conditions is particularly important, as it allows one to form the connection between rheology measurements and aggregate structure. A synopsis of previous research into both aggregate breakdown and restructuring highlights the knowledge gaps which this study will fulfill, and provides useful tools. Specifically, the concentric cylinder rheometer is confirmed as a viable, flexible instrument for shear energy input, and the measurement of rheological parameters. Finally, with the context provided in this chapter, the goals and importance of the present research are further clarified.

### 2.2 Rheology models and definitions

The study of the flow and deformation of matter in response to applied shear is called rheology [30]. The ratio of a substance's shear stress response to a shear rate is known as viscosity. Newtonian fluids are those whose viscosity is a constant value under constant

temperature and all shearing conditions. Newtonian behaviour is commonly exhibited by “pure” fluids, such as water, oils, and gases. Often, with the introduction of aggregating particulate matter, or for substances containing polymers, gels, creams, and emulsions, a fluid’s viscosity will no longer be constant [31]. Such fluids are aptly called “non-Newtonian”.

### 2.2.1 Time-independent rheological models

There are countless models to describe non-Newtonian behaviour. Figure 2.1 shows the qualitative shear stress ( $\tau$ ) vs. shear rate curves ( $\dot{\gamma}$ ) — also known as rheograms — for four illustrative time-independent, non-Newtonian models. The curve for a Newtonian fluid is also shown for comparison. The mathematical models for these fluids in one dimensional flow are provided in Table 2.1. Pseudoplastic fluids, also known as “shear-thinning”, are

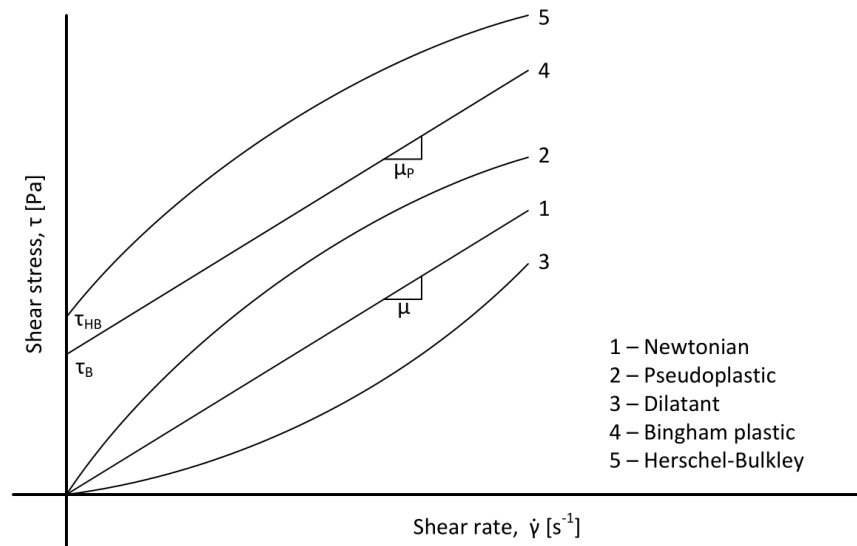


Figure 2.1: Qualitative rheograms for four time-independent rheological models. Adapted from [32, 33].

Table 2.1: Common rheological models to illustrate 1-D time-independent fluid behaviour [33].

Rheological model	Mathematical relationship
Newtonian	$\tau = \mu \dot{\gamma}$
Pseudoplastic	$\tau = K \dot{\gamma}^n; n < 1$
Dilatant	$\tau = K \dot{\gamma}^n; n > 1$
Bingham plastic	$\tau - \tau_B = \mu_p \dot{\gamma}$
Herschel-Bulkley	$\tau - \tau_{HB} = K \dot{\gamma}^n; n < 1$

those whose viscosity decreases with increasing shear rate. Conversely, dilatant fluids exhibit an increase in viscosity with increasing shear rate. Bingham and Herschel-Bulkley fluids are distinguished by the presence of a yield stress,  $\tau_B$  or  $\tau_{HB}$ . The yield stress of a fluid is the shear stress threshold which must be surpassed before the onset of flow. At shear stresses below the yield stress, these types of fluids behave as pseudo-solids. Once the yield stress is overcome, Bingham plastics exhibit a plastic viscosity,  $\mu_p$ , while Herschel-Bulkley fluids show shear-thinning characteristics. It is important to note that  $\tau_B$  and  $\tau_{HB}$  are fitted parameters, not true material properties, and rely on the applicability of the model to the fluid being studied. Figure 2.2 highlights the distinction between  $\tau_B$  and true yield stress ( $\tau_y$ ). The Bingham predicted yield stress is always greater or equal to the true property. That being said, the Bingham model is commonly used in the design of tailings-related systems, and is well suited to represent the concentrated suspensions of kaolinite clay used in the present study [21, 34].

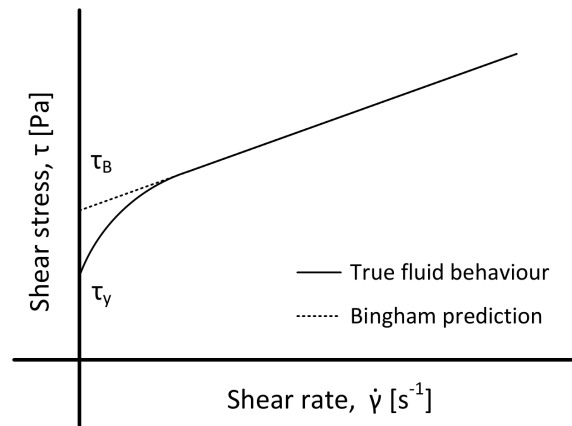


Figure 2.2: Comparison of Bingham predicted yield stress and actual value.

### 2.2.2 Time-dependent rheological models

Significant rheological complexity arises when the properties of a fluid are sensitive to shear history. This so-called time- or shear history-dependence is a long documented — yet still poorly understood — phenomenon in which the viscosity of a fluid is affected by the amount of time it is exposed to shear [35]. A comparison of a Newtonian fluid's shear stress response over time at constant shear rate to two types of time-dependent fluid models is

provided in [Figure 2.3](#). Specifically, thixotropic fluids exhibit a decrease in viscosity over time when exposed to shear. Although this is reminiscent of the pseudoplastic characteristic described above, the difference lies in the timescale; time-independent pseudoplastic behaviour is instantaneous. Over time and exposure to shear, the microstructure of a thixotropic substance undergoes re-orientation to align in the direction of shear [36]. This results in an overall reduction of the fluid viscosity. Brownian motion gradually restores the original microstructure upon cessation of shear [36].

Rheopexy, or anti-thixotropy, can be considered the opposite of thixotropy. Rheopexy is observed as the increase of a fluid's apparent viscosity over time under shear [35], due to the formation of microstructural elements which dissipate through Brownian motion when shear is removed [36]. Reversibility of the changes in apparent viscosity is the hallmark of thixotropic and rheopectic fluids [36]. In the case where permanent decrease or increase to fluid rheology is effected, either negative or positive *rheomalaxis*, respectively, is the correct term [37].

### 2.2.3 Rheological hysteresis

Both thixotropy and rheopexy are examples of rheological hysteresis, where the rheology of the system depends on the shear history of the substance. Rheological hysteresis is commonly investigated by imposing a continuously increasing, then decreasing shear rate in a rotational viscometer [38]. Time-dependent behaviour is observed when the shear stress response to these two phases do not coincide, as the fluid properties have been altered over the shearing period [38]. Thixotropy and rheopexy are illustrated in [Figure 2.4](#). Both the shapes of the curves, and the area enclosed by the hysteresis loop are characteristics specific to the time-dependent substance being considered [35].

Shear stress hysteresis provides insight into the re-arrangement of the microstructure of the particulates in the fluid under shear over time [39]. In the case of a rheopectic fluid, the higher shear stress of the return curve is an indication that changes have occurred at the particle level, forming aggregate structures that have made the bulk fluid more resistant to flow. At sufficiently high shear rates, aggregates may be broken down into clusters of individual particles which resist further degradation, or "primary flocs" [37]. Though

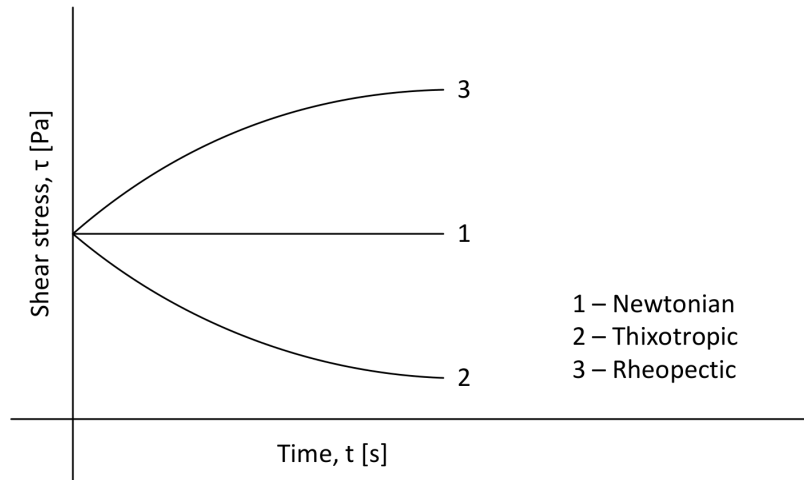


Figure 2.3: Comparison of two time-dependent rheological models with Newtonian behaviour at constant shear rate. Adapted from de Nevers [30].

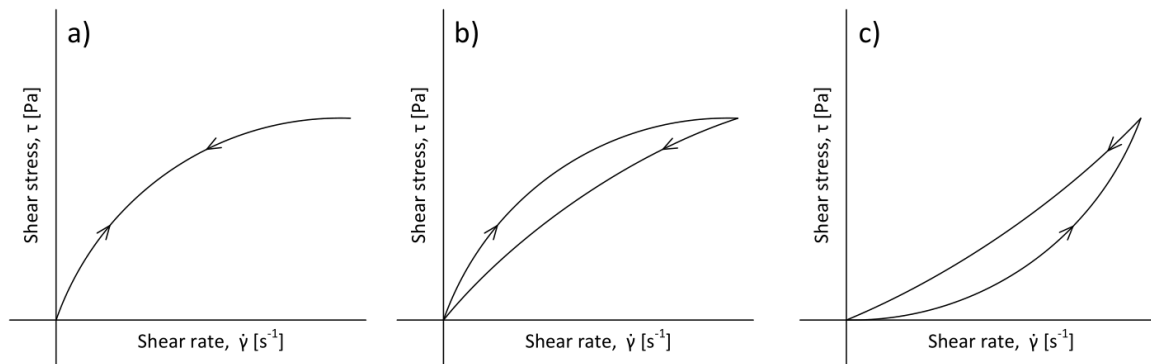


Figure 2.4: Shear stress response to increasing, then decreasing shear rate, illustrating examples of a) Time-independent pseudoplastic behaviour; b) Time-dependent thixotropic behaviour; c) Time-dependent rheopectic behaviour [39].

collisions between flocs may result in temporary aggregates, they do not last [40]. At this point, it is observed that the suspension will exhibit time-independent behaviour [37, 40].

Figure 2.5 shows the proposed structural formation of a suspended particle network, and the accompanying rheogram showing rheopectic behaviour.

### 2.3 Mechanisms for Aggregate Formation

Due to the high surface area to mass ratio of the fine particles, oil sands fluid fine tailings form a colloidal suspension in water, and particle-particle interactions are dictated by a combination of attractive and repulsive surface forces. Depending on the relative

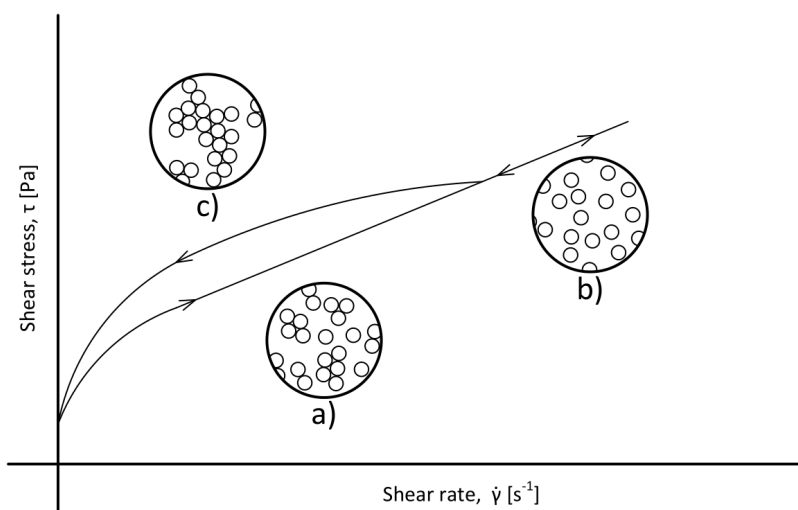


Figure 2.5: Rheopectic suspension rheogram with hypothesized evolution in microstructure [41] showing a) Initial suspension microstructure; b) Complete dissociation into primary flocs [40]; c) Larger, shear-resistant structures formed.

magnitude of these forces, the rheology of colloidal suspensions may range from nearly Newtonian, to a complex combination of non-Newtonian and shear history-dependent properties. In the case of industrial FFT, it is almost always the latter. Tailings in the oil sands industry are dosed with a variety of thickening additives with the purpose of capturing fine particulate matter into large, fast-settling flocs. The additives fall under two broad categories: inorganic salts, which dissociate in water to provide charge-neutralizing ions, and polymers, which mechanically bind aggregates through physical adsorption, entanglement, and bridging. In this thesis, the former is referred to as a “coagulant”, and the latter as a “flocculant”. The terminology is consistent with the Oil Sands Research and Information Network (OSRIN) [42], but it is important to state the distinction. In literature, there is often an overlap of definition between the terms due to the two commonly being used in conjunction.

Many previous studies agree that of the clay species present across all oil sands process streams, kaolinite is the most dominantly abundant [11–18]. Derakhshandeh [29] compared the rheological properties of FFT samples from Shell Canada Inc. operations in Ft. McMurray, Alberta with a kaolinite suspension at identical solids concentration and surface chemistry. The author concluded that under these conditions, the rheological behaviour of the two suspensions were quite similar [29]. For these reasons, a suspension

of kaolinite was used as a surrogate for industrial tailings in the present research. The following sections explain the forces involved in, and the mechanisms by which aggregates are formed.

### 2.3.1 Kaolinite surface charges

Kaolinite particles take the form of thin hexagonal plates [43], with a diameter of 0.1 to 2  $\mu\text{m}$  [44]. Each particle unit is composed of a tetrahedral siloxane layer, and an octahedral aluminum oxide layer [5]. Through cation exchange, the particles acquire a net negative charge [5].

Understanding the expected surface charges of kaolinite particles is crucial to predicting the conditions favorable for aggregation, and the aggregate configuration. Due to relative ease of measurement, the zeta-potential ( $\zeta$ ) is often used as a surrogate for surface charge, and can demonstrate the pH dependency of kaolinite particle surface charge [45]. Zeta-potential analysis, provided in Figure 2.6 shows the iso-electric point for the edge surface of kaolinite exists at  $\text{pH}=7$  [45], below which the zeta-potential is positive. As suspension pH increases, the edge surfaces of kaolinite adsorb aqueous  $\text{OH}^-$  ions, and acquire a negative charge [44]. For pH values between 4 and 10, the zeta-potential of the siloxane

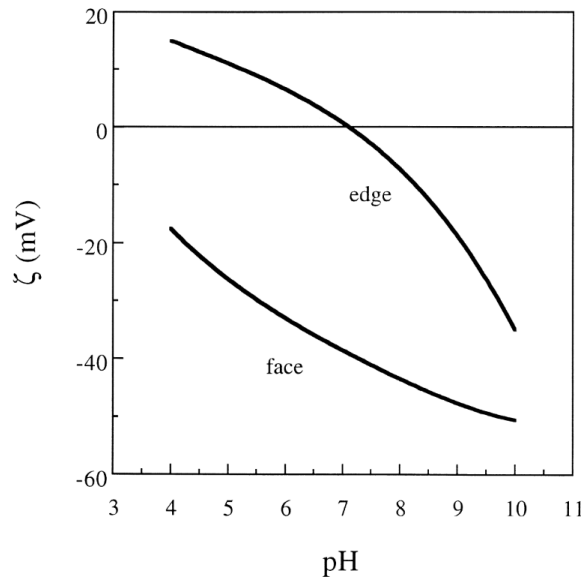


Figure 2.6: Zeta potential of edge and face surfaces of kaolinite. Reproduced from Johnson et al. [45].

face plane remains negative [45], indicating the negative charge on the siloxane face is permanent for this pH range.

### 2.3.2 Colloidal forces governing kaolinite particle aggregation

The surface charge on kaolinite particles gives rise to a surrounding Electric Double Layer (EDL), composed primarily of counter-ions of the opposite electrical sign to the charged surface. The thickness of this ionic cloud is called the Debye length and is proportional to temperature, and inversely proportional to the counter-ion valency and concentration [46]. The repulsive force between EDLs of the same electrical sign is responsible for stabilizing dispersed particles in a suspension, and is one of the two forces described by Derjaguin, Landau, Verwey, and Overbeek in what is known commonly as “Classic DLVO” theory [47]. The other force is the attractive van der Waals (VDW) force. The relative magnitude of these DLVO forces determines the aggregation behaviour of colloidal systems [47]. Generally, between two particles of identical composition, DLVO theory illustrates a weak long-range attraction, mid-range repulsion, and a strong short-range attraction. Figure 2.7 shows the electrostatic barrier formed by repulsive EDL forces, which is reduced when ionic concentration is increased, and allows particles to approach closer to one another [48]. At sufficient ionic concentration, rapid aggregation is expected [46].

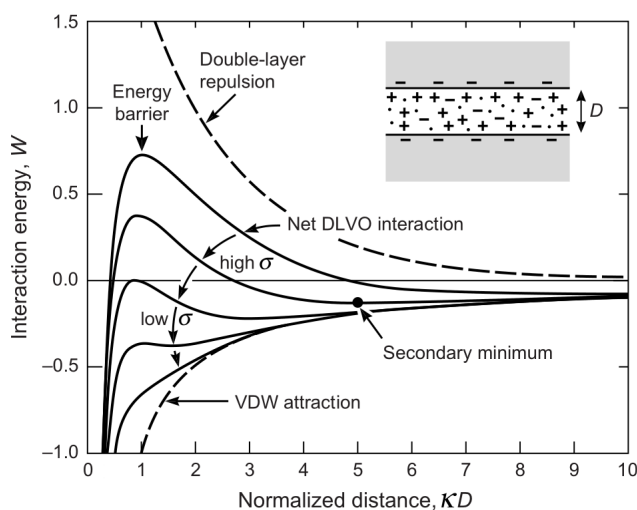
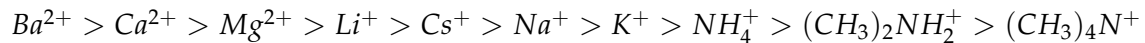


Figure 2.7: Combination of attractive van der Waals forces and repulsive electric double layer forces collectively describe DLVO theory. Reproduced from Israelachvili [46].

### 2.3.3 Aggregate formation through charge neutralization

Metal salts, when dissociated in water, provide the cations that serve to compress the negative EDL of kaolinite clay. This effectively lowers energy barrier and allows short-range attractive VDW forces to dominate. The relative effectiveness of cations at collapsing the EDL is known as the Hofmeister series [49]:



Based on the empirical Schulze-Hardy rule, the effectiveness of a coagulant predominantly depends on the valency of the cation, rather than the elemental species: higher valency ions are more effective at inducing coagulation in suspensions where the colloidal solids carry an opposite charge [50]. Therefore, the coagulating power of divalent cations such as calcium should not be understated. In 2003, Litzenberger [51] showed that by sequestering  $Ca^{2+}$  through the addition of Tetrasodium Pyrophosphate (TSPP), a suspension of kaolinite could be made to exhibit essentially Newtonian behaviour even at high solids concentrations. For this reason, calcium based salts (e.g. calcium chloride) are commonly used as coagulants.

### 2.3.4 Preferred kaolinite structural configuration

By combining what is known about surface charges and DLVO theory, kaolinite particle/particle structural configuration at varying pH and ionic strength may be surmised, and an idealized representation is provided in [Figure 2.8](#) [52]. The dashed lines and charges represent the relative thickness of the EDL and the electric charge carried on the kaolinite face and edge surfaces in each quadrant. Under alkaline conditions (zones B and D), kaolinite edge and face surfaces carry a negative charge and repulsive forces dominate. At high pH, dissociation between particles favor stable, dispersed colloidal systems (zone D), and is reflected by drastically reduced yield stress and viscosity values [20]. However, Nasser and James [44] observed that the maximum packing fraction of kaolinite at high pH increased with the addition of an NaCl electrolyte, indicating that in the presence of high pH and cation concentration, kaolinite particles preferentially form small, compact structures in face-face and edge-edge orientation (zone B). When the pH is low (zones

A and C), the positive charge on the edge surface coupled with the still-negative face surfaces results in a preference for “cardhouse” configuration. These structures tend to have a high void fraction [53]. Under acidic conditions when the ionic strength in the suspension is high (zone A), all combinations of face and edge connections can be seen [54]. Establishing a connection between preferred aggregate structural orientation and ionic and pH conditions allows further investigation into the relationship between aggregate size and configuration, and their influence on rheological properties.

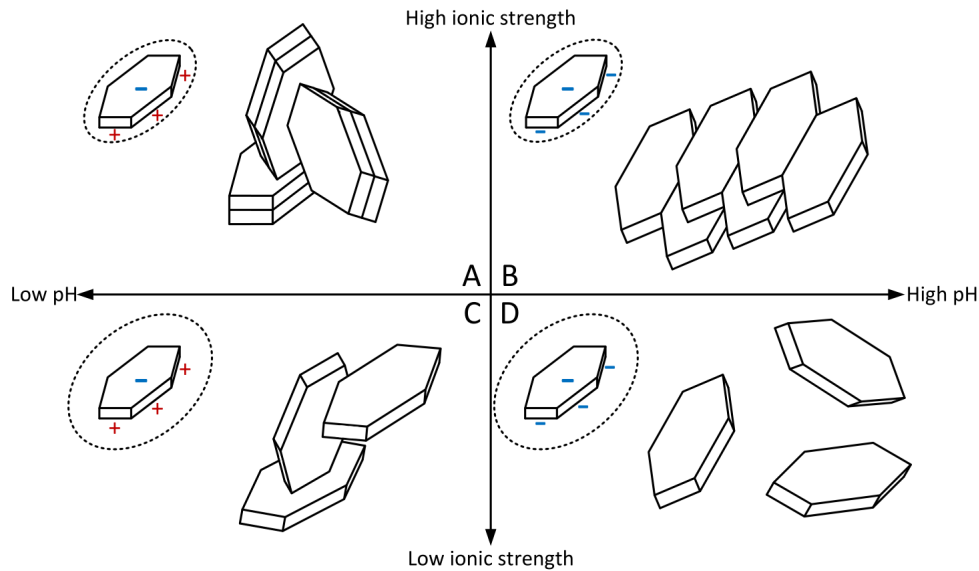


Figure 2.8: Preferred orientation of kaolinite aggregate structure at varying ionic concentration and pH [44, 52].

### 2.3.5 Relationship of aggregate size to rheology

Due to the opposing charge on kaolinite edge and face surfaces at low pH, large, loose “cardhouse” structures are obtained (Figure 2.8C) [44]. Despite only containing 10% solids by volume, these aggregates were found to be present in suspensions with relatively high yield stress and viscosity [20]. Although it may seem paradoxical that dense structures exhibit lower apparent viscosities and yield stresses compared to porous aggregates, previous study shows that no such contradiction exists. In their 1962 studies, Michaels and Bolger [40, 43] emphasize that the basic flow unit in shear should be considered clusters of primary particles, or flocs, rather than the individual particles alone. The authors conclude

that floc parameters such as floc volume fraction are more appropriately used to predict rheological properties [40, 43]. This conclusion was further confirmed by Shamirzadi [55], who showed that it is the volume concentration of aggregates, not total solids, which is the key predictor of suspension viscosity.

### 2.3.6 Aggregate formation through polymer flocculation

Flocculants are commonly composed from high molecular weight, anionic poly-acrylamides (PAM), which form long linear chains when dissolved in water [56]. Contrary to the electrostatic barrier suppressing action of cationic coagulants, flocculants rely on adsorption [56] and the formation of physical links — or bridging — between particulate matter [42]. In a 1972 study, Kitchener [57] concluded that the aggregates formed through flocculation were stronger than those produced by coagulation. However, the same study goes on to warn that overdosing a suspension with polymer can inadvertently cause colloidal stabilization; an undesirable effect that was not fully understood at the time [57]. Biggs [58], in 1995, used atomic force microscopy to measure the interaction force of poly-acrylic acid adsorbed on a surface. It was determined that the saturation of a surface by polymer results in repulsive forces arising from steric interaction.

In practice, coagulation and flocculation are commonly used in conjunction to form aggregates [42]. Inorganic salts are first added to destabilize the colloids. Polymers are then dispensed to provide strength in the form of flexible, elastic bonds [57]. Cryo-SEM analysis by Zbik et al. [53] revealed the addition of flocculant to a previously coagulated system does little to alter the structural configuration of the aggregates—the role of the flocculant is merely to provide strength and preserve the state of the pre-existing aggregates.

## 2.4 Tailings Thickening and Degradation

In industry, coagulants and flocculants are introduced into tailings slurry either in a thickening unit operation, used by operators such as Canadian Natural's Horizon Oil Sands Project [59], or through in-line flocculation, found at projects like Syncrude Canada Ltd.'s operations in northern Alberta [60]. The ultimate goal of thickening tailings is to

promote rapid consolidation of solids so warm process water can be efficiently recycled, and to produce a trafficable surface which can be reintegrated into the surrounding boreal forest ecosystem [9]. However, in the thickening process, large volumes of water are trapped interstitially within aggregates. In a study conducted by Vaezi et al. [61] in 2011, it was shown that as the size of a kaolinite aggregate increases, so does the void fraction. The authors concluded the largest aggregates formed were over 1000  $\mu\text{m}$  in diameter, and were composed of just 5% solids by volume [61]. In practice, shearing of the thickened tailings during pipeline transport leads to the fracture of aggregates [23, 61]. As a result, some of the trapped water is released, and the rheological characteristics of the tailings suspension are negatively affected [21, 22, 24, 25].

#### 2.4.1 Sources of shear in pipeline transport

The pipeline transport of thickened tailings from the bitumen extraction plant to the containment facility exposes the mixture to two primary sources of shearing. The foremost source of shear is within the large capacity slurry pumps which provide the driving force for pipeline transport. The second is shearing due to friction as the slurry travels along the pipeline itself. Due to the high yield stress of the thickened tailings, flow is generally expected to be limited to the laminar regime [62]. For the laminar flow of a fluid through a pipe with circular cross section, the shear stress is at a maximum at the pipe wall, and decays linearly to 0 at the pipe centerline. This is commonly known as the shear stress decay law. However, it is critical to note that for fluids exhibiting a yield stress, there will be a certain radial position at which the local shear stress falls below the yield stress. As a result, the laminar pipe flow of paste tailings is characterized by an unyielded core, borne by a surrounding annular yielded region. Figure 2.9 shows the annulus and core of a yield stress fluid in a pipe.

The radius of the unyielded core plug region  $r_{plug}$ , obtained by substituting the fluid yield stress into the shear stress decay law is given by:

$$r_{plug} = \frac{\tau_y}{\tau_w} R \quad (2.1)$$

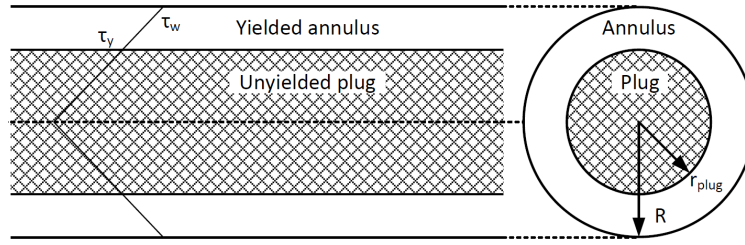


Figure 2.9: Laminar flow of a yield stress fluid.

The rate of shear energy dissipated by wall friction is calculated with:

$$\dot{W}_l = \ell_w \dot{m}_{total} \quad (2.2)$$

where  $\dot{m}_{total}$  is the total mass flow rate in the line, and  $\ell_w$  is the frictional lost work in a pipe in laminar flow:

$$\ell_w = \frac{4\tau_w L}{\rho D} \quad (2.3)$$

Finally, since the unyielded plug is unaffected by shearing, it is not influenced by the energy dissipated through friction. The lost power is therefore divided by the mass of the annular region only:

$$\varepsilon = \frac{\dot{W}_l}{m_{an}} \quad (2.4)$$

where the annular mass is given by:

$$m_{an} = \pi (R^2 - r_{plug}^2) L \rho \quad (2.5)$$

### 2.4.2 Shear-induced rheology reduction

As previously mentioned, the rupturing and overall degradation of aggregate structure due to shearing is a particular problem in the field of tailings transport. In a 2004 study, Schaan et al. [21] observed that for flocculated thickener underflow passing through a single booster pump, the yield stress was decreased from 50 Pa to 19 Pa. After flowing through a second, similar pump and 300 m of 75 mm pipeline, the slurry yield stress was further reduced to only 5 Pa [21]. Despite the relative strength of flocculant bonds over van der Waals forces, sufficient shearing will still cause them to rupture [57].

## 2.4. TAILINGS THICKENING AND DEGRADATION

In 2009, Salinas et al. [25] studied the effect of shear energy input on thickened copper mine tailings using an in-line shearing device with three unique rotor configurations connected to a thickener underflow stream. A variable speed drive was used to control shear energy input to the suspension passing through the device. Vane yield stress measurements were made before and after shearing by the device, and again after the suspension had been sufficiently sheared independently to reach a “fully-sheared” state [25]. Yield stress reduction was then correlated with the energy absorbed from the shearing device per unit volume of slurry [25]. Based on the results from Salinas et al. [25]’s study, shown in Figure 2.10, shear energy drastically reduced the yield stress of the tailings suspension: 600 kJ/m<sup>3</sup> of energy absorbed was sufficient to reduce the suspension yield stress to approximately 20% its original value. Furthermore, it was concluded that shearing device geometry had little impact on rheology reduction; energy dissipation was the determining factor in yield stress degradation [25].

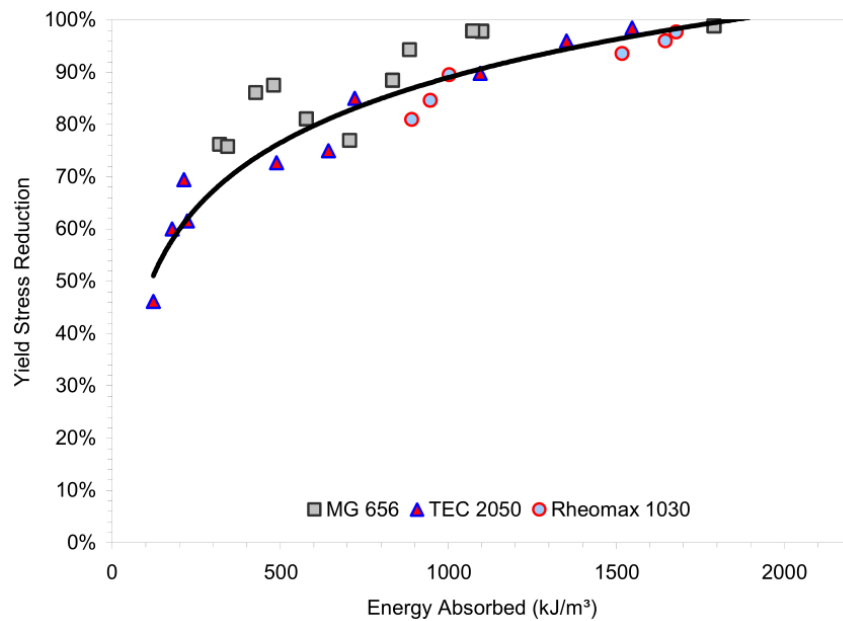


Figure 2.10: Yield stress reduction as a function of energy dissipated for three types of flocculant. Reproduced from Salinas et al. [25].

Once the independence of energy input on geometry was established, Treinen et al. [24] furthered the work by Salinas et al. [25] in 2010 by incorporating a bench top concentric cylinder viscometer as the shear input device. The viscometer offers a distinct advantage

over the shearing apparatus used by Salinas et al. [25]: Figure 2.11 shows that by measuring the torque required to maintain a constant rotor speed, the rheology reduction of a sample could be monitored in real time. The research by Treinen et al. [24] demonstrated the concentric cylinder viscometer as a viable dual-purpose device to simultaneously input shear energy and quantify rheological evolution [24]. These principles serve as the inspiration for the present study.

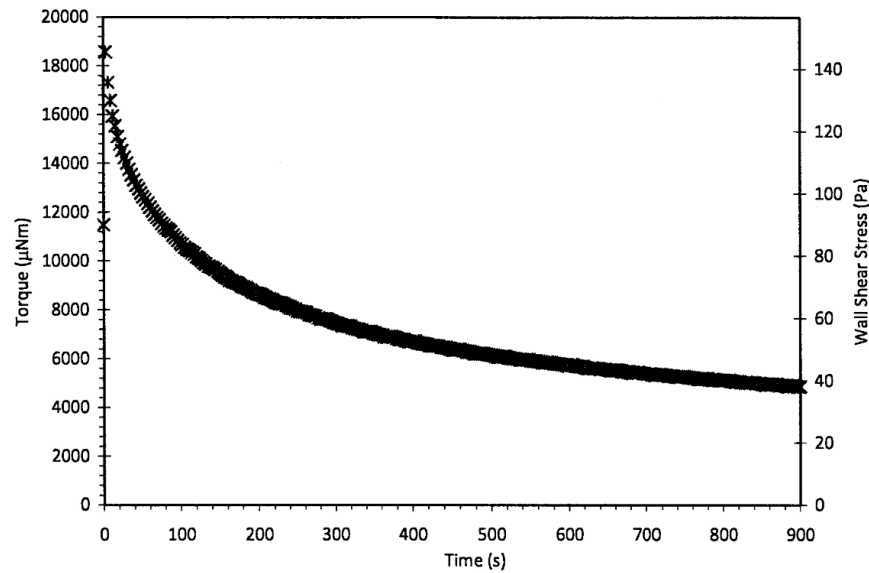


Figure 2.11: Use of concentric cylinder viscometer to measure rheology reduction of 43 wt% bench scale thickener underflow as a function of time. Shear rate held constant at  $120 \text{ s}^{-1}$ . Reproduced from Treinen et al. [24].

The concentric cylinder viscometer method of energy input was used again in a 2012 study on the pipeline transport of thickened tailings by Gillies et al. [22]. Two batches of oil sand flotation tailings were diluted, flocculated, and subjected to shear energy in both concentric cylinder viscometer and a 265 mm pipeline loop. Despite differences in composition and initial rheological properties, both batches showed a 50% yield stress reduction after exposure to a cumulative  $1500 \text{ kJ/m}^3$  of shear energy [22]. Both unique batches displaying an identical yield stress reduction after exposure to equal energy input was likely a coincidence, especially when considering the flocculated copper mine tailings studied by Salinas et al. [25] showed an approximate 95% yield stress reduction after  $1500 \text{ kJ/m}^3$  of energy dissipation (see Figure 2.10). Nevertheless, Gillies et al. [22]'s study concluded that good agreement was found between the yield stress ratio obtained from

viscometer and pipe loop geometries. The results, presented in Figure 2.12, indicate that suspension response to shearing in concentric cylinder and pipe geometries are comparable [22].

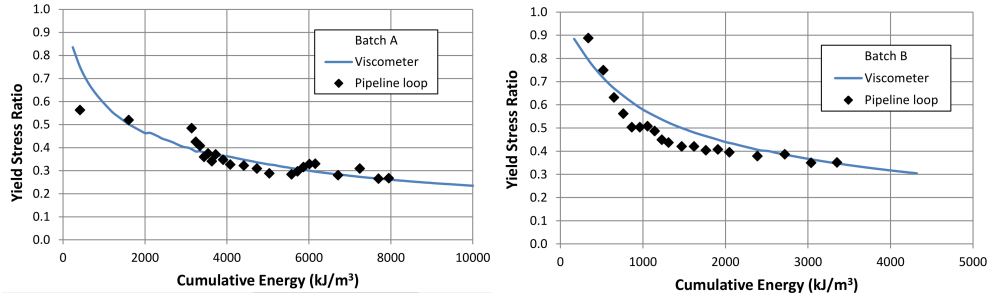


Figure 2.12: Yield stress reduction of two batches of thickened oil sands tailings in viscometer and pipe loop geometries. Reproduced from Gillies et al. [22].

Most recently in 2018, Neelakantan et al. [63] connected shear energy input to aggregate size and structural changes in concentrated, polymer dosed kaolinite suspensions. Using a custom-built concentric cylinder shearing apparatus to provide shear, shear-induced evolution in aggregate size distributions were monitored using Focused Beam Reflectance Measurement (FBRM). When coupled with vane yield stress measurements, the authors concluded that aggregate size and suspension yield stress are directly related, and shearing causes a decrease to both parameters. In other words, the fracturing of aggregates by shear energy and subsequent decrease in apparent solids volume fraction through the release of trapped water was directly responsible for the reduction in measured yield stress.

## 2.5 Shear-Induced Re-aggregation

An early fundamental study in 1959 by Reich and Vold [64] presents the average floc size in a shear field as a dynamic equilibrium between growth and destruction. Therefore, there should exist some shearing conditions where aggregate growth is favored. Michaels and Bolger [40] state that for structural equilibrium to exist:

$$\left( \frac{\text{No. of bonds broken}}{\text{second}} \right) = \left( \frac{\text{No. of collisions}}{\text{second}} \right) \left( \frac{\text{No. bonds formed}}{\text{collision}} \right)$$

The collision probability of flocs (assumed to be spheres) in laminar Couette flow is given by Mason and Bartok [65]:

$$\text{Collision Probability} = \frac{2}{\pi} \dot{\gamma} \phi_F \quad (2.6)$$

where  $\phi_F$  is the volume fraction of flocs. When the steady state is not reached during shear, it is expected that aggregate structure will continue to change over time [40].

The concept of floc re-formation after breakage has been thoroughly studied by researchers in the field of wastewater treatment. The preponderance of these studies utilize the “jar test” apparatus, typically comprised of a shearing impeller with an on-line optical size measurement instrument [27, 28, 66–70]. In 2004, McCurdy et al. [71] used such a device with an on-line photometric dispersion analyzer to assess the turbidity of raw water dosed with aluminum based coagulants as it passed through a series of varied shearing intervals. The goal was to compare the effectiveness of alum, poly-aluminum chloride, and a combination of the two as coagulants [71]. The experiments focused on imposing long periods of gentle mixing with inter-dispersed bursts of intense agitation. The aggregate size analysis results showed that structural recovery was possible, and a combination of the two coagulants displayed the most potential for aggregate size recovery after breakage [71]. This was credited to the greater charge neutralization capacity of the combination of coagulants [71].

A 2009 study by Kim and Park [72] investigated the ability for particles to re-aggregate in a pipeline after being sheared apart by a pump. Dilute suspensions were prepared using mono-sized polystyrene particles dosed with aluminum based coagulant. Samples were withdrawn for size analysis at 4 points: after a mixing tank, where the coagulant is dosed; before and after a centrifugal pump; and after a section of straight pipe. Overall, particles leaving the high shear environment of the pump have the smallest size, but were observed to grow as they were exposed to lower shear in the pipe section.

In 2013, Vaezi [26] studied the structural evolution of dilute flocculated aggregates in response to laminar tube flow. The shear environment was controlled by varying the tube diameter and length in three sections: a flocculation section where PAM flocculant was

dosed; a breakdown section characterized by high shear; and a conditioning section of similar shear to the first section. Aggregate sizes were determined by measuring settling rates in a quiescent chamber. Results indicated that the floc breakdown dominated at higher shear rates, with fragmentation of aggregates identified as the main mechanism. Initial floc breakdown was observed independent of shear rate, which shows primary aggregates are fragile and easily ruptured. However, after time and lower shear, re-flocculation began to compete with structural degradation. Re-flocculation was accompanied by a decrease in aggregate density. The frequency distribution of aggregate diameter ( $f_{nd}$ ) in each of the three sections is provided in Figure 2.13, and indicates that aggregate size distribution in the re-flocculation zone approached that of the pre-sheared conditions, albeit without representation from the smallest particle sizes. This indicates the smallest floc fragments in the population were incorporated into larger flocs through collisions.

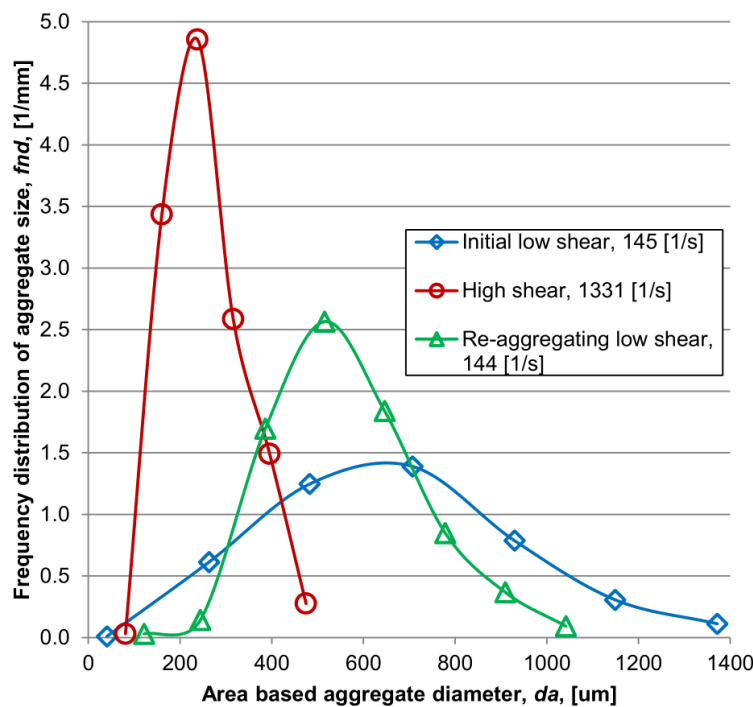


Figure 2.13: Evolution of particle size distribution due to different levels of shear. Reproduced from Vaezi [26].

Litzenberger [51] studied the rheological properties of concentrated kaolinite clay suspensions in pipe loop and concentric cylinder geometries in 2003. It was unexpectedly observed that periods of shear exposure to samples greater than 17 vol% solids resulted in

an irreversible increase in measured pipeline pressure drop. Although this was attributed to an increase in rheological parameters, laboratory investigation ruled out any change to particle size, electrophoretic mobility, calcium ion concentration, or pH. An adequate explanation for the mysterious thickening behaviour remained elusive.

## 2.6 Concentric Cylinder Rheometry

Several previous studies [22–24] have established the concentric cylinder geometry as well suited to determining the effect of shear energy input on rheology reduction in thickened tailings. The present research seeks to further what was learned by investigating the shearing conditions which allow for the recovery of rheological properties in a concentric cylinder rheometer. In addition to the ability to input precisely controlled shear, non-Newtonian and time-dependent fluid behaviour are accurately characterized using a rotational rheometer. Rotational rheometers typically operate under the principles of the Taylor-Couette flow of a fluid trapped between two concentric cylinders, and the key dimensions are shown by the schematic in Figure 2.14. To obtain rheological measurements, the freely turning inner cylinder, with a radius of  $R_1$  and length  $L$ , is rotated at a defined range of spindle speeds ( $\omega$ ), while the torque ( $T$ ) required to produce this rotation is recorded. One popular type of spindle known as a DIN rotor terminates with a shallow cone tapering at angle  $\theta$ . This angle is defined such that error due to end effects is reduced [55]. Other spindles may feature a recessed end with the same purpose.

The integrated equation to describe Newtonian fluid behaviour is [73]:

$$\omega = \frac{T}{4\pi L\mu} \left( \frac{1}{R_1^2} - \frac{1}{R_2^2} \right) \quad (2.7)$$

For a Bingham plastic fluid, the integrated equation is [73]:

$$\omega = \frac{T}{4\pi L\mu_p} \left( \frac{1}{R_1^2} - \frac{1}{R_2^2} \right) - \frac{\tau_B}{\mu_p} \ln \left( \frac{R_2}{R_1} \right) \quad (2.8)$$

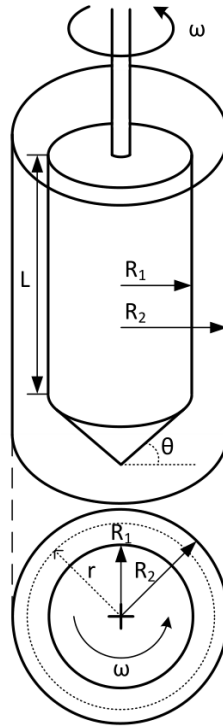


Figure 2.14: Side and end views of the key dimensions in a concentric cylinder rheometer with DIN spindle geometry.

which can be rearranged to give:

$$T = 4\pi L \frac{R_1^2 R_2^2}{R_2^2 - R_1^2} \mu_p \omega + 4\pi L \ln \left( \frac{R_2}{R_1} \right) \frac{R_1^2 R_2^2}{R_2^2 - R_1^2} \tau_B \quad (2.9)$$

Therefore, the Bingham parameters  $\tau_B$  and  $\mu_p$  can be determined by applying linear regression to a plot of  $T$  vs  $\omega$ .

Finally, the rate of energy dissipated into the rheometer sample,  $\varepsilon$  [W/kg], can be calculated using the following equation:

$$\varepsilon = \frac{T\omega}{m} \quad (2.10)$$

where  $m$  represents the mass of the tested sample.

## 2.7 Complications with Concentric Cylinder Rheometry

### 2.7.1 Onset of Taylor vortices

The chief requirement for rheological measurements is that the energy dissipated must strictly be viscous, i.e. rheological parameters may only be interpreted from laminar flow conditions. At high spindle speeds, a system of stacked toroidal vortices is formed [31]. The presence of these vortices, including their undulations at increasingly higher inner cylinder rotational velocities, represent a secondary means of energy dissipation in the fluid. Therefore, rheological data must only be limited to spindle speeds below the onset of Taylor vortices. Shook and Roco [73] describe one method of calculating this critical angular velocity:

$$\omega_{crit} = \frac{45\mu}{\left[\frac{(R_1+R_2)}{2}\right]^{\frac{1}{2}} (R_2 - R_1)^{\frac{3}{2}} \rho} \quad (2.11)$$

A second method is provided by Bird et al. [31], which gives a similar, but more conservative estimation.

$$\omega_{crit} = \frac{41.3\mu}{R_2^2 \left(1 - \frac{R_1}{R_2}\right)^{\frac{3}{2}} \rho} \quad (2.12)$$

It should be emphasized that these predictions for the onset of Taylor vortices were developed for Newtonian fluids only. There are no available correlations for the formation of secondary flows in non-Newtonian fluids. However, Equation (2.11) has been used in the past for the prediction of the critical spindle angular velocity for Taylor vortex formation in a Bingham fluid, using the plastic viscosity ( $\mu_p$ ) as a substitute for Newtonian viscosity ( $\mu$ ) [74].

### 2.7.2 Incomplete shearing of a sample

It can be shown that the torque at any radial position,  $r$  (see Figure 2.14) is a constant value, and described by:

$$T = 2\pi r^2 L \tau_{r\theta} \quad (2.13)$$

This becomes a critical consideration in the testing of any fluid which possesses a yield stress. If the shear stress at any radial position  $r$  falls below the fluid yield stress, there will exist a portion of unyielded fluid between  $r$  and  $R_2$ . Therefore, a minimum torque must be provided such that  $\tau_{R_2} \geq \tau_y$ :

$$T_{min} = 2\pi R_2^2 L \tau_y \quad (2.14)$$

If the true yield stress of the fluid is unknown, it may be substituted with the Bingham yield stress. Doing so gives a conservative estimate of  $T_{min}$ , as the true yield stress is always less than or equal to the Bingham fitted parameter (see [Figure 2.2](#)). Determination of true yield stress is discussed in [Section 2.8](#).

### 2.7.3 Wall slip

One of the major sources of error in any rheological measurement of suspensions and pastes is wall slip [75–77]. Slip occurs in multi-phase, homogeneous suspensions due to a combination of steric, hydrodynamic, viscoelastic, and chemical forces [76]. These forces tend to cause attraction between suspended particles, pulling them from container boundaries and causing a depletion of the dispersed phase near smooth surfaces [76]. The result is the formation of a thin layer of the suspending fluid at container walls. Since this solids-lean phase generally has a lower rheology than the bulk suspension, there is a large velocity gradient in the fluid layer [78], giving rise to the eponymous wall slip effect.

In concentric cylinder rheometry, wall slip is exacerbated by smooth instrument surfaces and a narrow gap between inner and outer cylinder [79], especially when the sample is also composed of large aggregates and has high solids concentration [76]. Due to the “lubrication” of the rotating spindle by the low-viscosity fluid layer, rheometer slip is characterized by a false under-prediction of yield stress and viscosity measurements.

Despite these drawbacks, concentric cylinder rheometry should still be accepted as a viable rheological measurement technique. Wall slip can be detected by repeating experiments with different gap widths [80]. Slip can also be mitigated by increasing the friction of the cup and spindle surfaces through sandblasting, applying a rough coating [81,

82], or cutting vertical grooves into the geometries [83, 84]. In practice, rectifying wall slip at the inner rotating surface sufficiently reduces the source of error [75]. It is not necessary to take further steps to eliminate slip at the outer rheometer boundary [75]. Finally, slip can be precluded altogether through the use of the vane geometry, though the trade-off is the requirement for larger sample volumes and the loss of some measurement flexibility.

## 2.8 Vane yield stress measurements

Pioneered by researchers Nguyen and Boger [85] in the 1980's, the vane technique allows for the accurate measurement of the true yield stress of a paste or suspension, and does not rely on an accurate model fit. A vane is constructed of 4 or more blades spaced around a thin central shaft, as shown in Figure 2.15. After insertion into the sample, the device is rotated slowly at constant speed, typically less than 0.1 rpm while torque is monitored. Immediately prior to yielding, torque reaches a maximum. The yield stress of the sample is calculated using the following relationship [85]:

$$\tau_y = \frac{T_{Max}}{V_c} \quad (2.15)$$

where  $V_c$  is a vane dimension-dependent constant [85]:

$$V_c = \frac{\pi D_v^3}{2} \left( \frac{H}{D_v} + \frac{1}{3} \right) \quad (2.16)$$

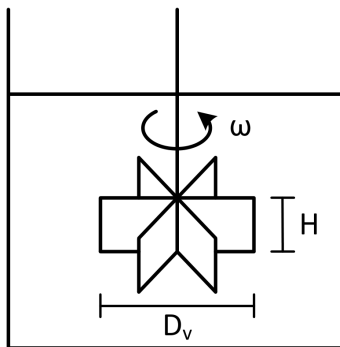


Figure 2.15: Use of a vane to measure the true yield stress of a fluid.

The dimensions of the vane and its placement within the sample container must obey the criterion outlined by Nguyen and Boger [86].

In addition to measuring the yield stress as a model-independent true material property, vane rheometry offers a few other distinct advantages. Due to the thin vanes, there is significantly less disturbance to samples associated with inserting the geometry into the test medium [87]. This is especially important when the test samples exhibit shear-sensitive thixotropic or rheopectic behaviour. Furthermore, since the plane of yielding occurs within the fluid itself, as opposed to at a solid boundary, wall slip is all but eliminated [87].

Ultimately, vane devices are used to provide an excellent measurement of a sample's yield stress as a true material characteristics. The vane can also be used to assess other rheological properties. A 2007 study by Fisher et al. [87] compared rheological measurements obtained from a capillary rheometer with vane geometry values, with favorable results. However, in addition to relatively large sample size requirements, significant complications can arise when the samples to be tested exhibit shear history-dependent characteristics. One major consideration is that as the viscosity and yield stress of these fluids change in response to time under shear, so does the volume of the fluid which is affected by the shearing. In the present study, knowing the volume of the sheared sample is crucial. Therefore, so long as care is taken to recognize and minimize sources of error, the concentric cylinder rheometer remains a viable and preferred option for the determination of rheological parameters and study the effects of shear energy on kaolinite suspension properties.

## 2.9 Scope of the Current Study

A review of the relevant literature presented in this chapter highlights the connection between aggregate size and non-Newtonian properties. The life cycle of the floc has been discussed, from conception through electrostatic charge neutralization and polymer bridging, to growth through collision, and to rupture due to exposure to excess shear energy. Rupture is not final, as the potential for re-aggregation and structure reformation exists. The concentric cylinder Taylor-Couette flow rheometer has been showcased as a

versatile instrument capable of measuring complex rheological parameters, and providing acute manipulation over shear energy input into a control volume.

This review also highlights a few deficiencies in the existing body of knowledge requiring further exploration:

1. While yield stress degradation and rheological breakdown has been a phenomenon well studied in the field of tailings management, similar levels of attention have not been paid to the re-aggregation of broken flocs, especially at high suspension concentrations. Previous re-aggregation studies tend to rely on limited and inflexible optical particle size measurement tools, and dilute suspensions which are only indirectly relevant to industrial tailings.
2. There has generally been insufficient focus on the time- and shear history-dependent rheological properties of kaolinite clays, and on the advantages of understanding such properties on the design of tailings transport and management solutions.
3. No efforts have been made to establish an energy input based connection between re-formation of ruptured colloidal clay aggregates with a suspension's initial rheological parameters.

Thus, the objectives of this work are:

1. To investigate time dependent rheological properties of kaolinite clay using a concentric cylinder rheometer;
2. To identify shearing and energy input conditions favorable to floc structure breakdown and re-formation, respectively;
3. To establish a connection between the energy required for the above with suspension rheology; *and*
4. To determine the factors which have the greatest influence on re-aggregation potential.

## Chapter 3

# Experimental Method

### 3.1 Introduction

The experiments conducted in this study seek to establish a connection between initial kaolinite suspension rheology and the shearing conditions under which rheological properties may be influenced. All experiments were performed using a concentric cylinder rheometer. At constant rheometer shear rate (i.e. spindle speed), a continuous variation to the torque response indicates a change in the test suspension's resistance to shear. This in turn represents an evolution in the clay aggregate structure. In this chapter, sections [Section 3.2](#) and [Section 3.3](#) detail the materials and equipment used in sample preparation and testing. [Section 3.4](#) provides the procedures followed to prepare reproducible test samples, and the rheometer settings used to obtain rheological measurements. The experimental variables are also explained in this section. The determination of the shear energy required to induce clay aggregate structural breakdown and re-formation relied on intermediate experimental data, and is discussed in [Chapter 4](#). The flow chart in [Figure 3.1](#) summarizes the experimental procedure. Text boxes with dashed outline indicate steps that were varied or omitted as required over different experimental trials.

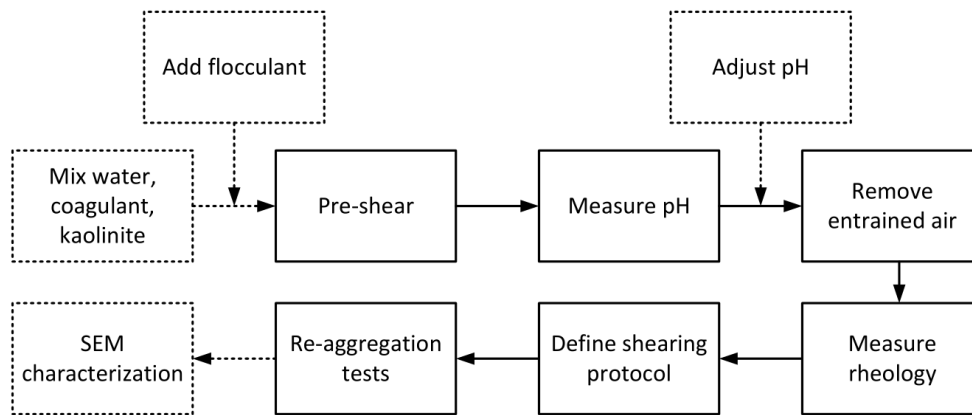


Figure 3.1: Experimental procedure flowchart. Dashed text boxes denote steps that were not included, or varied, for every experimental run.

## 3.2 Materials

### 3.2.1 Kaolinite clay

Kaolinite clay is a dominant component in oil sands tailings, and at similar solids concentrations in aqueous suspension, exhibits comparable rheological behaviour as fluid fine tailings [29]. For this reason, kaolinite clay is commonly used as an analogue to produce model tailings in tailings-related research [34]. The kaolinite used in the present study was supplied by Plainsman Pottery in Edmonton, Alberta. Based on the Saskatchewan Research Council's experience with this type of clay, the density was accepted to be  $2696 \text{ kg/m}^3$  [88]. Due to the potential introduction of ionic impurities during supplier production, all experiments were performed using a single batch of clay to minimize inconsistencies.

### 3.2.2 Water and pH adjustment

Edmonton tap water is regarded to have moderate hardness, with an average of 109 mg of calcium carbonate per liter [89]. The presence of undocumented cations such as calcium and magnesium can have a strong impact on kaolinite aggregate structures. Therefore, all clay suspension samples were prepared using de-ionized (DI) water from a Millipore Elix Advantage 5 water filtration system. Beakers and lab implements were washed with detergent and rinsed with DI water before and after use.

Where applicable, the pH of the suspensions was modified using aqueous solutions of sodium hydroxide (NaOH) and hydrochloric acid (HCl). Both NaOH and 1M HCl were purchased from Fisher Chemical. Dry NaOH was dissolved to prepare a 5M solution using DI water.

### 3.2.3 Thickening additives

Di-hydrated calcium chloride ( $\text{CaCl}_2 \cdot 2\text{H}_2\text{O}$ ) was purchased from Fisher Chemical and used as a coagulant salt to induce the formation of aggregates. When used, coagulant was dosed at a mass ratio of  $\text{CaCl}_2 \cdot 2\text{H}_2\text{O}:\text{kaolinite}=0.001$ .

Magnafloc<sup>®</sup> LT27AG is an anionic linear acrylamide and acrylic acid copolymer flocculant with a molecular weight of approximately 15 million Da. It was purchased as a powdered solid from Ciba Specialty Chemicals. Where applicable, the flocculant was dissolved, diluted, and dosed at 100 g per tonne of dry clay. Polymer flocculant preparation is further discussed in [Section 3.4.3](#).

## 3.3 Equipment

### 3.3.1 Sample Preparation

All mass measurements were made using an A&D FX-3000 electronic scale, accurate to 0.01g. Samples were mixed using an IKA RW 20 overhead mixer with 45° pitched bladed turbine (PBT) and Lightnin A310 hydrofoil impellers. Typical mixing tank geometry for all kaolinite suspension preparation is shown in [Figure 3.2](#). Impeller diameters are provided in [Table 3.1](#). To remove entrained air, samples were subjected to low pressure using a vacuum pump (Gast Manufacturing). The maximum vacuum provided by this pump is -14.98 kPag, insufficient to cause significant liquid loss by evaporation at 20°C. During the de-airing procedure, samples were continuously mixed using an IKA RCT basic IKAMAG dual purpose magnetic mixer and hot plate. The hot plate function was not used.

All pH measurements were made using a Mettler Toledo SevenMulti pH meter with new InLab Expert Pro-ISM probe. The probe was calibrated using buffers of pH 2.00, 4.00, 7.00, and 10.00 daily before use. The buffers were supplied by Fisher Chemical.

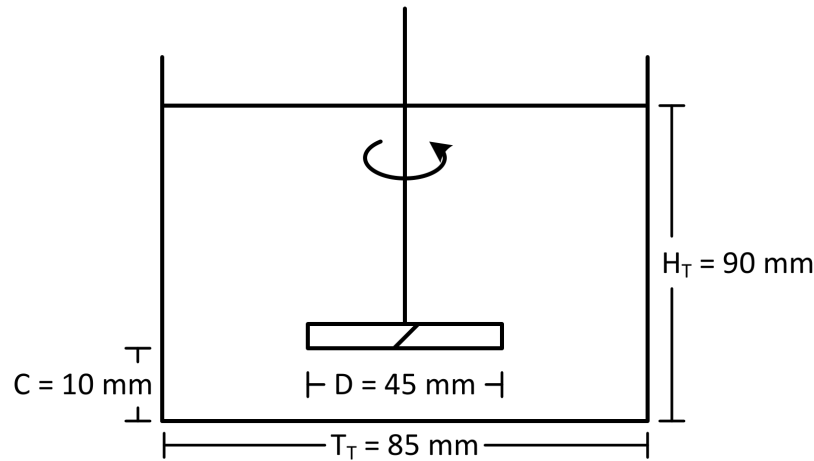


Figure 3.2: Typical mixing geometry used in the preparation of all kaolinite suspensions. Diagram is not to scale.

Table 3.1: Overhead mixer impeller types and sizes.

Impeller type	Diameter, D
45° PBT	45 mm
Lightnin A310	64 mm

### 3.3.2 Rheometer

Rheological measurements and shear energy input experiments were performed using a Discovery Hybrid rheometer (DHR-2) from TA Instruments. The rheometer was used in concentric cylinder configuration with DIN rotor, allowing for ease in obtaining rheological data. Energy input into the sample could also be precisely controlled. The technical specifications of the DHR-2 equipment are provided in [Table 3.2](#). For the majority of tests, the spindle and cup used were constructed from aluminum. A separate stainless steel spindle of the same dimensions, with sandblast roughened surface was used to check for wall slip. Rheometer readings were periodically checked against S60 standard oil with known viscosity, purchased from the Cannon Instrument Company. Standard oil measurements are provided in [Appendix A](#).

Table 3.2: DHR-2 rheometer technical specifications.

Description	Specification
Torque range	0.01 - 200,000 $\mu$ Nm
Minimum torque increment	0.10 nNm
Angular velocity range	0 - 300 rad/s
Angular velocity resolution	1.4E-9 rad/s
Temperature control	DI water cooled Peltier plate
Temperature range	-20°C to 150°C
Bearing type	Magnetic
Spindle radius ( $R_1$ )	14 mm
Cup radius ( $R_2$ )	15.2 mm
Spindle length (L)	42.03 mm
Operating gap	5.7 mm
Sample size	24 mL

## 3.4 Procedures

### 3.4.1 Experimental conditions investigated

To investigate the re-aggregation potential of kaolinite structures under varying suspension conditions, several values for a number of sample parameters were tested, and compared to a base case. With the exception of a flocculated sample, which required a unique preparation procedure, all parameters were varied one at a time from the base case. The base solids concentration was chosen to be 35 wt% kaolinite clay, which allowed for comparison at 28 wt% and 42 wt% while remaining within the expected solids concentration range of FFT [9]. The base suspension also had an unadjusted pH of 4.3, which did not vary significantly at the other solids concentrations. Since zeta-potential analysis showed EDL forces are expected to increase at higher pH, due to kaolinite edge surfaces acquiring a negative charge [45], re-aggregation was also examined at pH 7.3 and pH 9.8. To compress the repulsive EDL and encourage the formation of initial aggregates,  $\text{CaCl}_2 \cdot 2\text{H}_2\text{O}$  coagulant was dosed at a mass ratio of 0.1% to dry kaolinite clay, reproduced from previous procedures by Litzenberger [51] and Rahman [88]. A suspension variation where no calcium was added was also investigated. Finally, the capacity for re-aggregation was studied for a polymer flocculant amended suspension. Due to the flocculation procedure

followed, which was adapted from Neelakantan [23], the solids concentration of these samples was approximately 40 wt%. Flocculant was dispensed at 100 g/tonne of dry kaolinite. pH was not adjusted prior to flocculation. Table 3.3 summarizes the base case and all additional values tested for each parameter.

Table 3.3: Range of values tested for all experimental parameters.

Parameter	Base case value	Other values tested
Solid concentration (wt%)	35 wt%	28 wt%, 42 wt%
pH	4.3	7.3, 9.8
Coagulant mass ratio to dry clay	0.1%	None
Flocculant dosage	None	100 g/tonne kaolinite

### 3.4.2 Kaolinite suspension preparation

Kaolinite clay suspensions were prepared one day in advance of testing, and kept in sealed glass beakers. All samples were disposed immediately after use. The procedure below gives the steps for preparing the suspension. A more detailed safe work procedure is available in Appendix B.

1. Weigh desired amount of de-ionized water in 600 mL Pyrex glass beaker with 85 mm diameter;
2. Weigh appropriate mass of kaolinite clay;
3. Weigh di-hydrated calcium chloride coagulant such that the mass ratio of  $\text{CaCl}_2 \cdot 2\text{H}_2\text{O}$  : dry kaolinite clay = 0.1%;
4. Add coagulant salt to DI water, stir to dissolve; *and*
5. Gently add kaolinite clay, seal the beaker using laboratory film, and allow suspension to remain undisturbed overnight.

Although care was taken in the addition of kaolinite clay powder to water and mixing, some air entrainment is impossible to avoid. For fluids exhibiting a yield stress, entrained bubbles cannot escape the suspension unassisted, and would contribute to significant error during testing. The procedure below is modified from Rahman [88], and gives the steps to

remove any trapped air using a vacuum pump, and prepares the sample for rheometer testing.

1. With 45° PBT impeller placed 1 cm from container bottom, mix the sample thoroughly at 800 rpm until uniform. Take care to minimize air entrainment, though the priority is to produce a homogeneous slurry;
2. Gently pour the sample to a stoppered side arm vacuum filter flask;
3. Add a magnetic stir bar and connect vacuum hose to flask side arm;
4. Turn on magnetic mixer, set at 300 rpm. Turn on vacuum pump;
5. As entrained air is removed from sample under vacuum, periodically move the flask to provide even coverage by the magnetic stir bar, and swirl the flask by hand;
6. Remove sample from vacuum after a period of 30 minutes, or when no more bubbles appear;
7. Carefully decant slurry into clean, dry, 600 mL beaker;
8. Place 45° PBT impeller 1 cm from container bottom. Slowly increase impeller speed until suspension is fully mixed, but no vortex is formed. For a typical 35 wt% slurry, this is achieved at 780 rpm, but varies depending on sample conditions. Initial mixing speeds for suspensions with different solids concentrations are provided in [Table 3.4](#), but should be decreased as samples are withdrawn for testing;
9. Measure pH, and adjust using NaOH or HCl to the desired value if required; *and*
10. Allow sample to mix for at least 1 hour before proceeding to rheometer testing.

### 3.4.3 Flocculant preparation

A subset of samples was dosed with flocculant to examine the effects of polymer additives on the re-aggregation of kaolinite structures. Flocculant was prepared from dry Magnafloc<sup>®</sup> LT27AG powder. Stock solutions were prepared and kept for a maximum of two days. Fresh feed solutions of diluted flocculant were prepared immediately prior to dosing to

Table 3.4: Initial impeller speeds to ensure complete mixing, but no vortex formation for four kaolinite suspensions with differing solids concentration. Speed was decreased as samples were withdrawn for rheometer experiments.

Solids concentration	Typical mixing speed (rpm)
28 wt%	600
35 wt%	782
42 wt%	883
40 wt%, flocculated	816

ensure minimal degradation over time. Any left over feed flocculant was disposed of at the end of the day.

To prepare 1 wt% Magnafloc<sup>®</sup> stock polymer flocculant was prepared using the following procedure:

1. 1 g of dry Magnafloc<sup>®</sup> LT27AG polymer powder was added to 100 mL DI water in a 150 mL glass beaker with 53 mm diameter;
2. Set the overhead mixer to 260 rpm, with 45° PBT impeller placed at 5 mm clearance from beaker bottom; *and*
3. Clamp the beaker and leave solution to stir overnight.

The stock polymer flocculant was further diluted to 0.1 wt% feed solution prior to dispensing in kaolinite suspension:

1. 10 mL of stock polymer is removed by plastic syringe and combined with 90 mL DI water in a 150 mL glass beaker; *and*
2. Solution is mixed for 30 minutes using the 45° PBT at 200 rpm, placed 5 mm from the bottom of the beaker.

#### 3.4.4 Flocculated kaolinite suspension preparation

This procedure, developed by Neelakantan [23], allows one to consistently produce a flocculated sample approximately 40% solids by mass, beginning with a dilute clay suspension.

1. In a 1000 mL beaker, appropriate masses of water and kaolinite clay are weighed and combined to produce 8 wt% kaolinite suspension;
2. Suspension is mixed using Lightnin A310 hydrofoil impeller with 5 cm clearance from container bottom for 30 minutes, until homogeneous;
3. 0.1 wt% feed polymer solution is dispensed at a dosage of 100 g of flocculant per tonne of dry clay over 30 seconds;
4. Mixing continued for 30 seconds. The impeller is then switched off and flocculated clay is allowed to settle;
5. Clear supernatant water is decanted, and the flocculated solids is transferred to a coffee filter supported by wire mesh strainer to continue draining over 90 minutes;
6. De-watered flocculated clay is then transferred to a 600 mL beaker and sheared for a minimum of 2 hours using the 45° PBT impeller with 1 cm clearance at 900 rpm. Due to the extremely shear-sensitive nature of the flocculated suspensions, it is not possible to obtain meaningful rheological measurements without first applying a generous period of pre-shear; *and*
7. Any air entrained in the fully sheared suspension was removed under vacuum using the procedure outlined in [Section 3.4.2](#) above.

Density measurements confirmed this procedure resulted in a 40 wt% flocculated suspension.

#### 3.4.5 Rheological measurements

1. Turn on the DHR-2 rheometer and perform the necessary startup steps;
2. Turn off the overhead mixer. Using plastic syringe, withdraw 24 mL slurry from bulk sample container, gently transfer to rheometer cup;
3. Slowly increase the speed of the overhead mixer until the sample is once again fully mixed without vortex formation;

4. Rheological properties of the sample were obtained by steadily increasing, then decreasing the angular velocity of the rotating spindle while measuring torque response. Under commonly tested sample conditions, the angular velocity range was chosen to be between 1-60% of the full-scale angular velocity capability of the rheometer (3-180 rad/s). Typical rheological tests took 800 seconds to complete, and consisted of 80 data point measurements, allowing for 10 seconds of measuring time at each data point. Due to increased viscosity and yield stress, rheology for flocculated and 42 wt% samples was measured over a range of 3-270 rad/s, and each rheogram consisted of 120 points. The total test time was increased to 1200 seconds.
5. Any data points which fall below the minimum torque for complete shear across the concentric cylinder gap, or above the critical velocity to form Taylor vortices must be rejected from the rheological calculations. Refer to the discussions in [Section 2.7.1](#) and [Section 2.7.2](#) for the data acceptance criteria for rheological parameter determination.

Bulk sample rheology was measured hourly to ensure rheological properties remained consistent and well defined throughout multiple re-aggregation tests. The detailed safe work procedure for rheometer operation is provided in [Appendix B](#).

#### **3.4.6 Re-aggregation experiment program**

Each sample was subjected to a series of constant shear rates with the intent of breaking any existing aggregates apart, then re-building them through shearing. Aggregate structure change was quantified by monitoring rheometer torque response at constant shear rates. Determination of the appropriate shear energy input for breakdown and re-aggregation is discussed in detail in [Chapter 4](#).

### **3.5 SEM Imaging**

Although the bulk of the experimental results are in the form of rheometer torque measurements, Scanning Electron Microscopy (SEM) complements the data by providing a method to visually identify structural changes at the aggregate level due to energy input.

Microscopic imaging was performed on clay samples through the nanoFAB Characterization Center at the University of Alberta. Approximately 2 mL of clay suspension sample was removed from the rheometer at specific times to visually inspect for structural changes due to shear energy induced conditioning at the particle level. Before imaging using the SEM, the suspension must first be flash-frozen using liquid nitrogen (-196°C). This “cryo-vitrification” technique allows the preservation of the clay particle structure. The sample is stored in the Savant SuperModulo freeze dryer at -0.08 kPag and -50°C for a period of 24 hours. At low pressure and temperature, the interstitial ice sublimates, leaving the clay particle structure intact. A small amount of each sample was then carefully transferred on to a carbon-backed SEM stub. Eight nanometers of carbon was coated on to each sample to enhance conductivity and improve SEM image clarity using the Leica EM ACE600 high vacuum sputter coater. The samples were then imaged using the ZEISS Sigma Field Emission Scanning Electron Microscope (FE-SEM). This FE-SEM can detect particles less than 1  $\mu\text{m}$ , sufficient to clearly identify changes in kaolin structure. All equipment related to SEM sample characterization was owned and operated by nanoFAB staff.

# Chapter 4

## Results and Discussion

### 4.1 Introduction

In this chapter, the impact of suspension pH, coagulant / flocculant addition, and solids concentration on kaolinite suspension rheology and time-dependent characteristics are examined. Aggregate breakdown and re-growth in Taylor-Couette flow are independently studied and the concentric cylinder rheometer is verified as a well-suited instrument for monitoring these changes. The ability to predict energy requirements for re-aggregation is explored, and the structural strengthening potential for kaolinite suspensions under various conditions is quantified. The key findings are summarized as:

**Significance of shear history dependent properties** Rheological measurements in concentric cylinder Taylor-Couette flow are commonly obtained by continuously increasing, then decreasing the angular velocity of a rotating inner cylinder. Shear stress hysteresis indicates that exposure to certain levels of shear energy input can induce structural changes, and influence the suspension's resistance to flow.

**Induced structural re-aggregation in response to shearing** A steady increase in rheometer torque response — a direct indication of increased resistance to shear, or re-aggregation — was observed in all samples when exposed to specific shear rates. Although the rheological properties of the unique samples were significantly different, it has been shown that the shear rate required for maximum rheometer torque

increase can be determined through interpretation of the initial rheogram for each sample.

**Re-aggregation potential of suspensions under varying conditions** The percent increase in rheometer torque response over a 300 second shearing period was evaluated as a re-aggregation potential. Samples containing the highest mass fraction of clay solids showed the greatest potential for re-aggregation. Conversely, samples at similar solids concentration but dosed with polymer flocculant displayed the smallest capacity for re-aggregation.

The results from this study demonstrate a strong link between the shear energy required for re-aggregation, and easily obtainable information from a relatively simple bench-scale test.

## 4.2 Kaolinite Suspension Rheology

### 4.2.1 Interpretation of Bingham parameters from rheometer data

Figure 4.1 illustrates a typical flow curve obtained with the TA Instruments DHR-2 concentric cylinder rheometer. The graph shows torque response ( $T$ ) to continuous variation in spindle speed ( $\omega$ ) for a 35 wt% kaolinite suspension coagulated using di-hydrated calcium chloride ( $\text{CaCl}_2 \cdot 2\text{H}_2\text{O}$ ). These conditions, at an unadjusted suspension pH of 4.3, represent the base case kaolinite suspension in this study. All other samples are variations of these conditions, except where further deviation is explicitly stated. The two parameter Bingham model is well suited to represent the rheological behaviour of all suspensions tested in this study [21, 34]. To calculate the Bingham yield stress ( $\tau_B$ ) and plastic viscosity ( $\mu_p$ ) parameters, the complete data set must be modified to exclude the points past the onset of Taylor vortices and the values where there is incomplete shearing across the rheometer gap. The criterion for excluding these points was discussed in Sections 2.7.1 and 2.7.2. A linear trend line is then applied to the remaining data points.

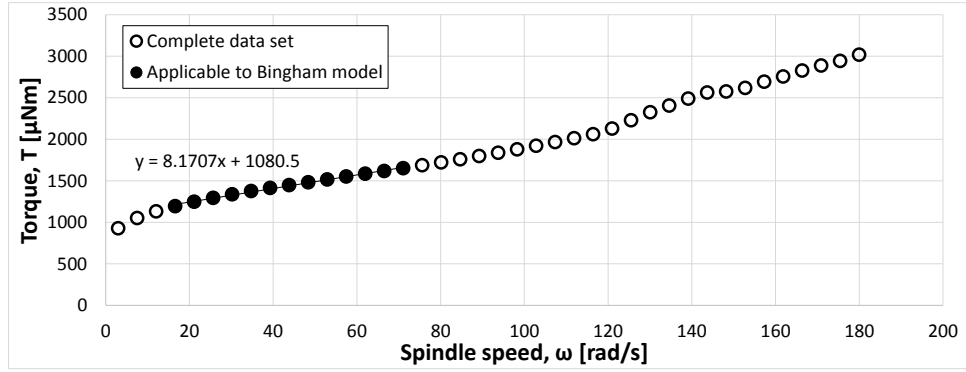


Figure 4.1: Typical rheogram for 35 wt% kaolinite clay. Linear regression applied to eligible data set to calculate Bingham parameters.

The integrated Bingham equation was given earlier as Equation (2.9) [73]:

$$T = 4\pi L \frac{R_1^2 R_2^2}{R_2^2 - R_1^2} \mu_p \omega + 4\pi L \ln \left( \frac{R_2}{R_1} \right) \frac{R_1^2 R_2^2}{R_2^2 - R_1^2} \tau_B$$

Using Equation (2.9),  $\mu_p$  can be calculated from the slope of the trend line, and  $\tau_B$  is obtained from the intercept. All other variables in Equation (2.9) are geometrical rheometer constants.

#### 4.2.2 Impact of suspension variation on Bingham parameters

Before proceeding to more complex concepts, it is beneficial to examine the effects of the different conditions studied on suspension rheology, and compare the results to expectations based on theory. Figures 4.2 and 4.3 summarize the variation in the Bingham parameters with changes in solids concentration, suspension pH, and coagulant and flocculant dosage.

Overall, solids concentration had the most significant impact on  $\mu_p$  and  $\tau_B$ . When the solids volume fraction was decreased to 28 wt%, both the plastic viscosity and yield stress decreased. Based on previous studies by Shamirzadi [55] and Neelakantan et al. [63], it is known that the apparent volume fraction of aggregates is an important determining factor of both viscosity and yield stress in a suspension. The same reasoning explains the high values of  $\mu_p$  and  $\tau_B$  observed in the 42 wt% suspension. For given solids concentration and calcium coagulant dosage, increasing pH resulted in a decrease in both the plastic

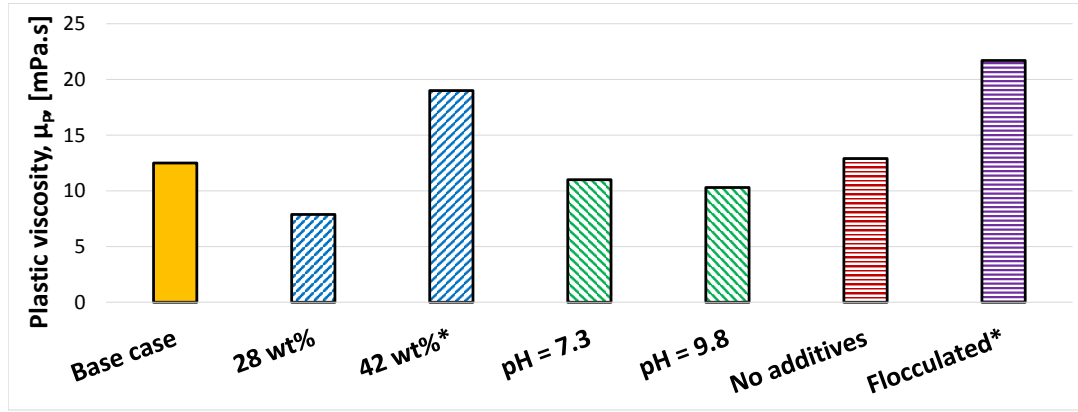


Figure 4.2: Variation of plastic viscosity with changes in suspension conditions. Due to high solids concentration, conditions marked with an asterisk denote a different rheometry procedure was used.

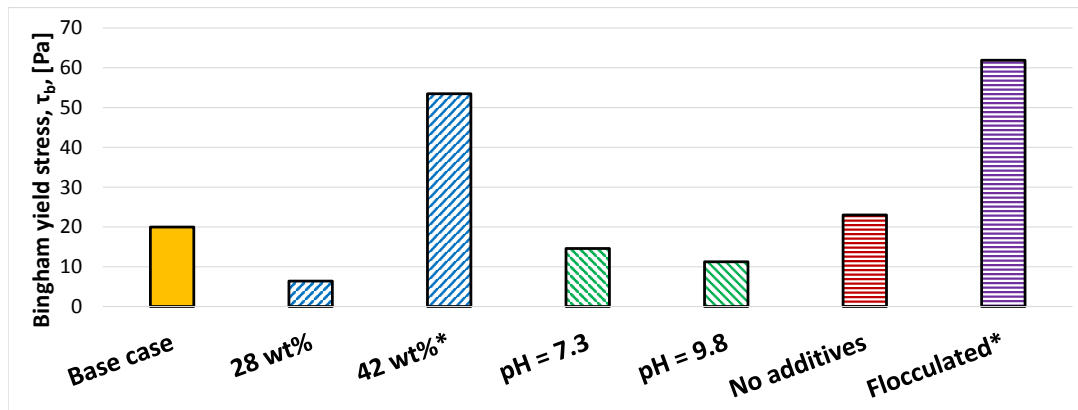


Figure 4.3: Variation of Bingham yield stress with changes in suspension conditions. Due to high solids concentration, conditions marked with an asterisk denote a different rheometry procedure was used.

viscosity and Bingham yield stress. While the charge on the siloxane face surface is negative regardless of pH [45], the isoelectric point of the aluminum oxide edge surface of kaolinite particles occurs at pH 7.0 [45]. As pH increases past 7, both edge and face planes of the kaolinite particles acquire an increasingly negative charge, which leads to stronger inter-particle repulsion. Marefatallah [90] observed a significant decrease in the particle size distribution of a kaolinite suspension when pH was increased to 11. Again, the reduction in the apparent volume fraction of aggregates explains the decrease in the rheological parameters.

Rheological parameters did not change appreciably in the absence of calcium coagulant for the 35 wt% kaolinite suspensions tested. The role of the calcium ions is to compress the repulsive electric double layer, and allow attractive van der Waals forces to induce the formation of aggregates [49]. However, at low suspension pH, large cardhouse floc structures are expected to form due to the charge difference on particle edge and face surfaces. Therefore, the effect of the coagulant was seemingly overshadowed. Similar observations were made by Nasser and James [44] who concluded that while the settling of dilute kaolinite suspensions occurred naturally at pH=2 for all electrolyte levels, sediment was only produced in alkaline suspensions with higher ionic concentration. Furthermore, Marefatallah [90] showed the coagulation effect of  $\text{CaCl}_2 \cdot 2\text{H}_2\text{O}$  became less pronounced as solids concentration increased.

Samples dosed with Magnafloc<sup>®</sup> LT27AG, a high molecular weight anionic PAM flocculant, formed a paste with high initial yield stress immediately after polymer addition. However, any exposure to shear caused immediate breakdown of the flocculated paste. Since the mixture was so shear-sensitive, no meaningful measurements of the suspension's Bingham parameters could be obtained with the concentric cylinder rheometer. Instead, the sample was subjected to 2 hours of pre-shearing before testing. This pre-shear significantly reduced the yield stress from the initial value, but allowed for a sample that could be analyzed with the rheometer. Due to the flocculation procedure followed, the solids concentration of this polymer-amended suspension was 40 wt%. After pre-shear, the Bingham yield stress and plastic viscosity were comparable to the un-flocculated 42 wt% suspension. The slightly higher rheological parameters may be explained by a small

remaining fraction of polymer bonds which resisted complete breakdown even after 2 hours of continuous shearing.

Due to the high solids concentration and resulting rheological properties, the flocculated suspension and 42 wt% suspensions required a modified rheology measurement protocol. The rheometer speed was limited between 3 to 180 rad/s for the majority of suspension conditions. When assessing the high solid concentration cases, the rheometer speed range was increased to 3 to 270 rad/s. This was done so that an important suspension characteristic could be properly observed: shear stress hysteresis.

### 4.3 Shear Stress Hysteresis

Rheopectic and thixotropic fluids exhibit time-dependent rheological behaviour. On a rheogram, time-dependent behaviour is observed as a discrepancy to the torque response to a consecutive increase and decrease in rheometer spindle speed, or hysteresis. Hysteresis is an indication of aggregate structural changes leading to altered resistance to deformation, and is a response to the shear energy input over the time of rheological measurement. [Figure 4.4](#) presents hysteresis indicative of rheopectic characteristics in three kaolinite suspensions. The circular and square data points correspond with increasing and decreasing spindle speed, respectively. Similar plots were obtained for all other conditions tested in this study, though as previously mentioned, the polymer flocculated condition required a period of pre-shear before measurement. When the solids concentration is increased to 42 wt% from 35 wt% ([Figure 4.4B](#)), there is a marked increase in the hysteresis present in the rheograms. Based on [Equation \(2.6\)](#), collision frequency between aggregates is directly proportional to the apparent solids volume fraction in Taylor-Couette flow. The increased statistical likelihood of forming new connections between broken aggregates results in more potential for growth in aggregate size. The subsequent increase to rheological properties leads to the pronounced hysteresis visible in the 42 wt% rheogram. Conversely, repulsive EDL forces dominate over all kaolinite particle surfaces when the 35 wt% suspension pH is adjusted to 9.8 ([Figure 4.4C](#)). Under these conditions, the particles tend to be dispersed and stable, and do not easily form new agglomerates. As a result,

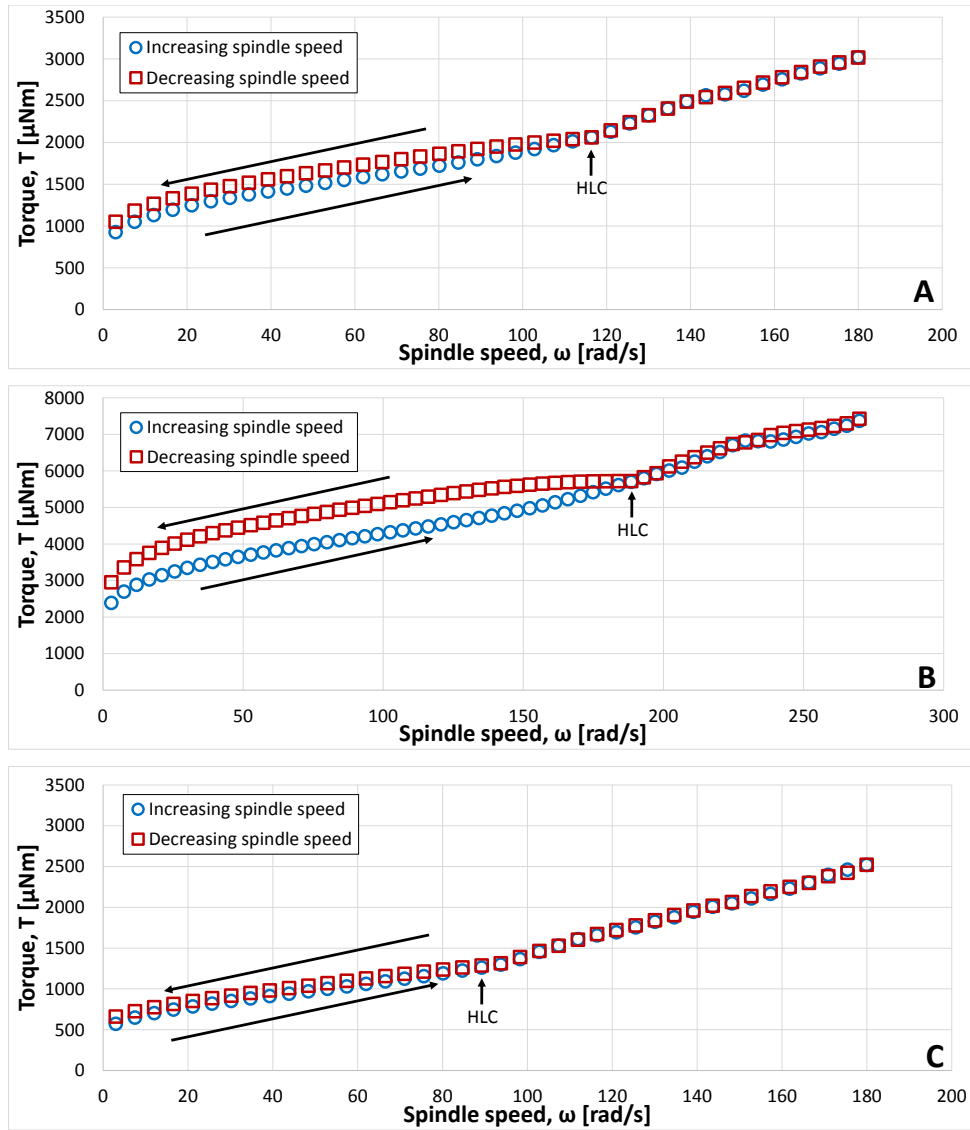


Figure 4.4: Rheograms for A) 35 wt%, B) 42 wt% and C) pH 9.8 (35 wt%) kaolinite suspensions all show a distinct difference in hysteresis.

the hysteresis feature is relatively diminished. From these plots, it can be inferred that the extent of rheological hysteresis depends on system properties, and is evidence that the potential for aggregate structural change is influenced by initial suspension conditions.

It is important to note that when spindle speed exceeds a certain value unique to each suspension, there is a change in rheological behaviour and hysteresis is no longer observed. This critical point is defined in this study as the Hysteresis Loop Closure—or HLC— point, and its importance is subsequently discussed.

### 4.3.1 Hysteresis loop closure

When the shear rate in the concentric cylinder rheometer exceeds the HLC point, the rheology of the test suspension exhibits shear history-*independent* characteristics, and indicates all aggregates have been reduced to primary flocs [37, 40]. All kaolinite suspensions examined in this study exhibit some degree of rheopectic characteristics, the HLC point can be observed on every rheogram. In the case of the 35 wt% suspension shown in [Figure 4.4](#), the HLC is observed at 116 rad/s. However, the location of the point varies considerably with changes in suspension rheology. Since this point marks the delineation between shear history-dependent and -independent properties in a substance, it is expected that shear-based treatment of suspensions would need to take this spindle speed into consideration. Because the cause of structural change is due to the shear energy input by the rotating spindle [22, 24, 63], the rate of energy dissipation at the HLC ( $\varepsilon_{HLC}$ ) was defined as a point of reference. Energy dissipation rate at any point on a rheogram can be calculated using [Equation \(2.10\)](#):

$$\varepsilon = \frac{T\omega}{m}$$

A comparison of the  $\varepsilon_{HLC}$  values for all test conditions is given in [Figure 4.5](#).  $\varepsilon_{HLC}$  differs immensely for each condition, but it was found to be a useful landmark in the development of the re-aggregation shearing experiment protocols.

Complete rheological data, including rheograms, calculated plastic viscosity, Bingham yield stress, and HLC for all samples are provided in [Appendix C](#).

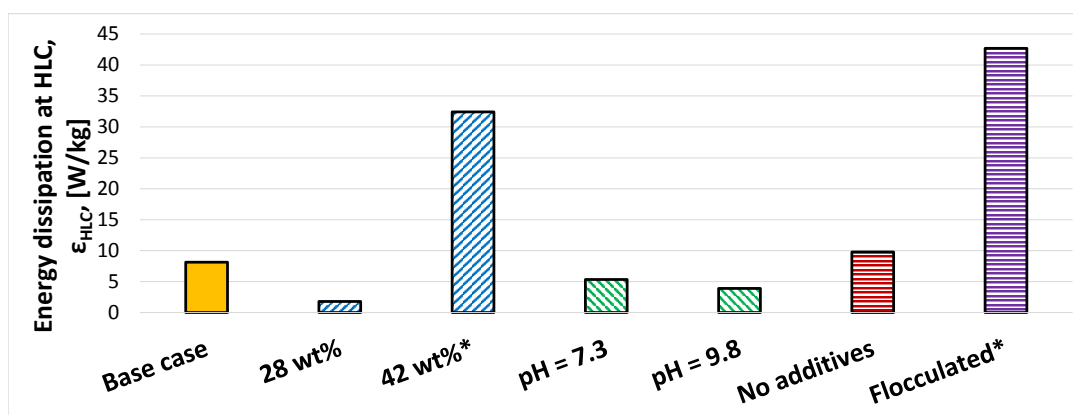


Figure 4.5: Variation of  $\epsilon_{HLC}$  with changes in sample conditions. Due to high solids concentration, conditions marked with an asterisk denote a different rheometry procedure was used.

#### 4.4 Development of Re-aggregation Experiments

A fundamental study by Michaels and Bolger [40] in 1962 showed that when an equilibrium state has not yet been reached between the formation and breaking of aggregate bonds in a colloidal suspension, the shear stress response to constant shear rate will vary continuously. In 2010, Treinen et al. [24] observed this phenomenon in a concentric cylinder viscometer as a decreasing torque response over time at constant spindle speed. This indicated the aggregates within the sample were undergoing breakdown. However, results from the current study show that at certain rheometer spindle speeds, an increase in torque response is instead observed, implying that equilibrium has been shifted to favor the formation of inter-particle bonds. Torque increase at constant shear rate is therefore an indication of re-aggregation in the test suspension, and forms the basis of the shearing experiments developed in this study.

Figure 4.6 shows the torque of a 35 wt% kaolinite suspension displaying evidence of re-aggregation in response to shear, and provides a valuable proof-of-concept. Inducing re-aggregation through shear energy input is referred to in this study as “conditioning”. The following section provides a discussion of how the energy input values that provided the most effective conditioning were determined.

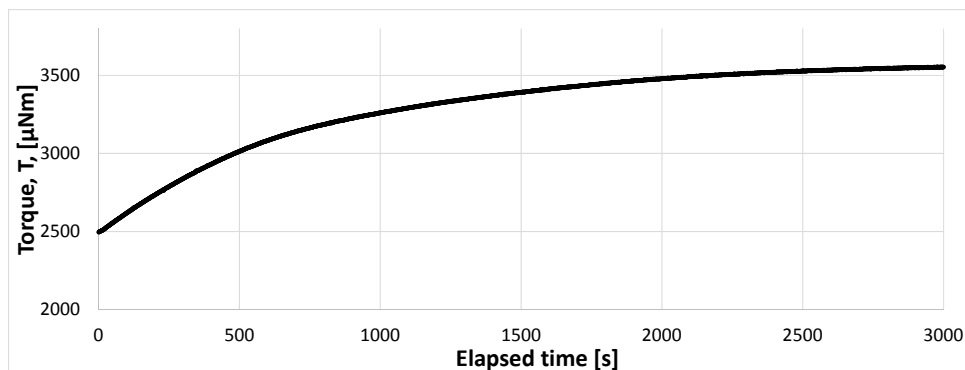


Figure 4.6: Continuous torque increase over time for constant spindle speed of 116 rad/s for 35 wt% kaolinite suspension, indicating structural re-aggregation and increased resistance to shear.

#### 4.4.1 Interval shearing experiments

To determine the energy input parameters where shear-conditioning gives the greatest amount of re-aggregation, samples were subjected to a 3-phase interval shearing test. Each phase is marked by a variation in shear energy input, controlled by setting rheometer spindle speed. Aggregate breakdown and re-structuring were observed through continuous monitoring of rheometer torque response at a constant spindle speed. Typical results for a shearing experiment are shown in Figure 4.7. Data from the first phase is required for comparison with third phase readings to determine the extent of breakdown. The high energy input over the second phase ensures that kaolinite aggregate structures within the suspension have been reduced in size as much as possible. Including this step is necessary

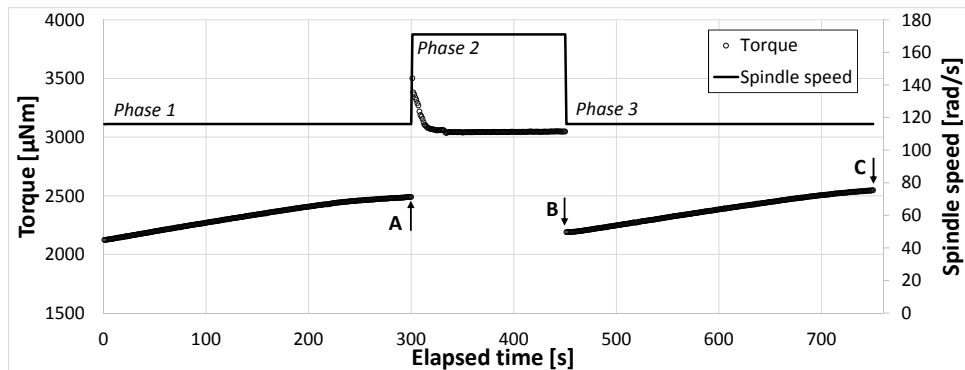


Figure 4.7: Typical results from 3-phase interval shearing test. Structural breakdown occurs over Phase 2; re-aggregation occurs in Phase 3.

so that re-aggregation for every test sample could be compared from the same initial aggregate conditions.

The breakdown and re-aggregation were quantified using the following:

$$\Delta T_{Break.} = \left( \frac{T_B}{T_A} - 1 \right) 100\% \quad (4.1)$$

$$\Delta T_{Cond.} = \left( \frac{T_C}{T_A} - 1 \right) 100\% \quad (4.2)$$

where  $T_A$ ,  $T_B$ , and  $T_C$  refer to the torque readings at points A, B, and C, as shown in Figure 4.7.

The second phase of the interval shearing method was used to determine the energy input requirements to achieve the most breakdown possible. For each test, the shear rate in Phase 2 was manipulated, while the shear rates in Phases 1 and 3 remained fixed. The rate of energy dissipation in Phase 2 was non-dimensionalized to a multiple of  $\varepsilon_{HLC}$ . The change in torque over Phase 2 was calculated using Equation (4.1). The results are shown in Figure 4.8. There is a sharp increase in the amount of breakdown achievable as energy dissipation increases from 1.0 to  $1.7\varepsilon_{HLC}$ . When the energy dissipation is further increased past  $1.7\varepsilon_{HLC}$ , there is insignificant change in  $\Delta T_{Break.}$  and thus little change in the magnitude of structural breakdown. Therefore, the rate of energy dissipation for the breakdown phase of all 3-phase interval tests was set to  $2\varepsilon_{HLC}$ .

The final stage of the 3-phase interval test was intended to determine the extent of

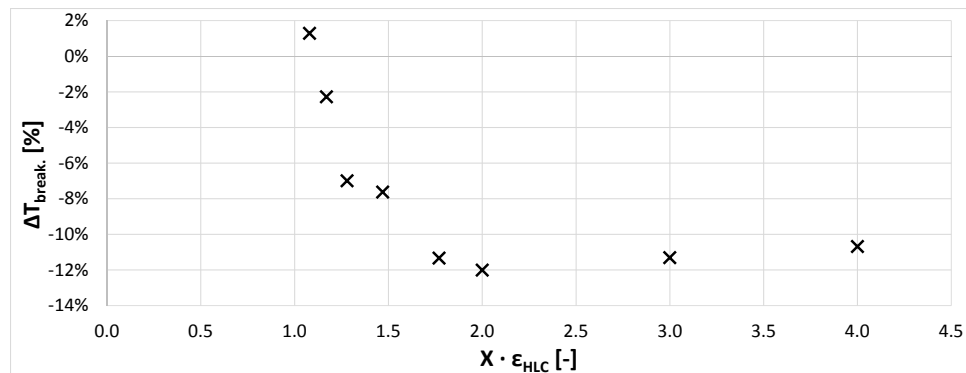


Figure 4.8: Torque decrease over breakdown period with respect to non-dimensionalized energy dissipation,  $\varepsilon_{HLC}$ .

re-aggregation achievable through shear energy conditioning. Torque increase over this conditioning interval was determined using Equation (4.2). Similar to the breakdown Phase, the rate of energy dissipation was non-dimensionalized as a multiple of  $\epsilon_{HLC}$ , unique to each suspension. The magnitude of re-aggregation achieved as a function of energy dissipation is discussed in detail in Section 4.6.1.

#### 4.4.2 Determination of time required for each interval

It is clearly observed from Figure 4.7 that torque readings reached steady state values well within 100 seconds over Phase 2. This was consistent for all 3-phase tests in this study. Based on this observation, the time allotted for Phase 2 was set at 150 seconds to allow for a margin of error. However, determination of a reasonable time period for Phases 1 and 3 was more complicated, since a steady state torque value was not achieved over 300 seconds. Figure 4.9 shows the torque at constant shear rate for 35 and 42 wt% kaolinite suspensions. As can be observed from this figure, it can easily take over 2000 seconds for these samples to reach steady state torque values during shear conditioning. However, it can also be shown that the torque values for both 35 and 42 wt% suspensions display growth in a similar, predictable fashion. Table 4.1 presents the torque increase values obtained from shearing these two suspensions, and shows that in both cases, approximately 35% of the final torque increase is achieved in the first 300 seconds. Due to the proportionality of the torque increase, it was decided to simply use 300 seconds for Phases 1 and 3. A shorter test period allowed for more experimental results to be obtained each day.

#### 4.4.3 Effect of multiple shearing cycles

Although the majority of the tests performed involve shearing the samples over 3 phases, a program with 5 conditioning phases and 4 breakdown phases was used to assess the repeatability of the re-aggregation effect. The results are provided in Figure 4.10. Based on the readings over multiple cycles, it is clear that the growth in torque has no time limit, nor is there evidence of a restriction on the number of times re-aggregation can take place. In fact, it can be inferred that some level of structural permanence is imparted through cycles of breakdown and shear: The local minimum torque reading at the beginning of each consecutive conditioning interval is observed to increase.

#### 4.4. DEVELOPMENT OF RE-AGGREGATION EXPERIMENTS

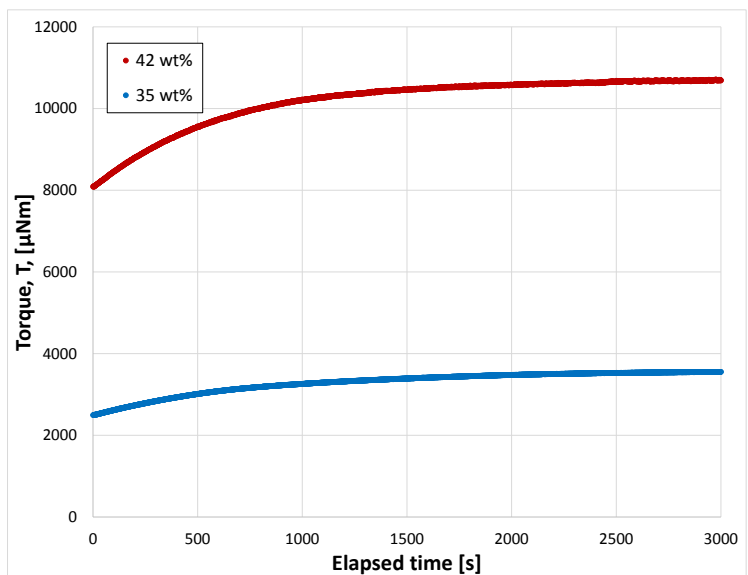


Figure 4.9: Torque increase trends for 35 and 42 wt% suspensions are similar in shape.

Table 4.1: Torque increase for 35 and 42 wt% suspensions, showing reading after 300 seconds is of similar proportion to equilibrium value for both cases.

35 wt%	Torque increase
Total	1058 $\mu\text{Nm}$
After 300 seconds	343 $\mu\text{Nm}$
% of total at 300 seconds	32%
42 wt%	
Total	2600 $\mu\text{Nm}$
After 300 seconds	997 $\mu\text{Nm}$
% of total at 300 seconds	38%

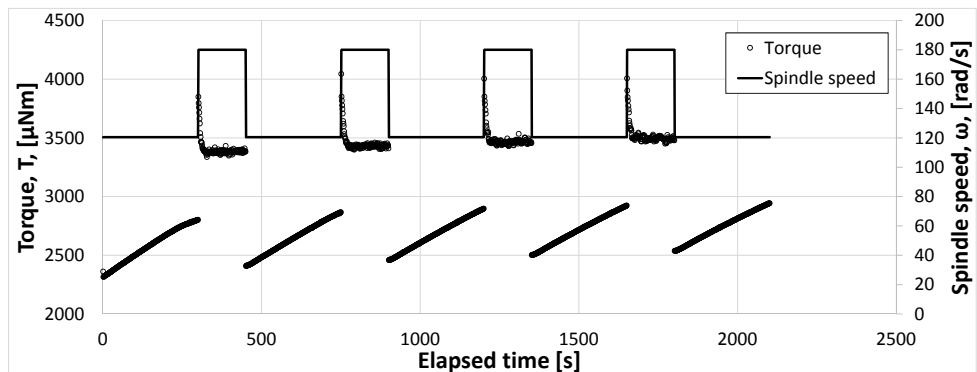


Figure 4.10: Torque response over repeat intervals of high and low shear, indicating that re-aggregation is reproducible, and there is seemingly no limit on the number of times an aggregate can be restructured.

## 4.5 Sources of Error

### 4.5.1 Wall slip

A major potential source of error in concentric cylinder rheometry of suspensions is the wall slip phenomena, caused by a near-wall depletion of the solid phase [76]. Previous studies have shown that wall slip effects can be mitigated by modifying the inner rotating spindle by applying a rough coating of particles, or by cutting vertical grooves into the rheometer geometries [75, 81–84]. In the current study, slip was investigated by comparing the Bingham parameters and value of  $\epsilon_{HLC}$  obtained using the default smooth aluminum spindle with a specialized roughened stainless steel rotor of the same dimensions. The results of this comparison are provided in [Figure 4.11](#) and [Table 4.2](#).

For the 35 wt% suspension, the comparison of rheological parameters obtained using smooth and roughened spindles shows good agreement. There was a 5% difference in the Bingham yield stress and plastic viscosity, with measurements made using the roughened spindle providing higher values, as expected. The small % difference indicates that wall slip was not a significant source of error for the majority of test cases in this study, which used a solid concentration at or below 35 wt%. The effects of wall slip are exacerbated at higher solids concentrations. There is a significant difference in the rheology measured by the smooth and roughened spindles for the 42 wt% suspension. A comparison of the calculated Bingham yield stress showed a 20% higher value for the roughened spindle. Fortunately, relatively few cases in this study used such a high mass fraction of solids. All experiments with samples greater than 35 wt% kaolinite content, including the flocculated suspension, were repeated using the roughened geometry to reduce the error from wall slip. For these cases, the results obtained using roughened geometry are presented.

### 4.5.2 Change in bulk suspension properties over time

Due to the settling nature of coagulant dosed clay suspensions, especially at low pH, the bulk suspension container required constant mixing while samples were withdrawn and tested. The energy imparted through mixing, coupled with evaporation effects, result in minute rheological changes which accumulate throughout the course of several

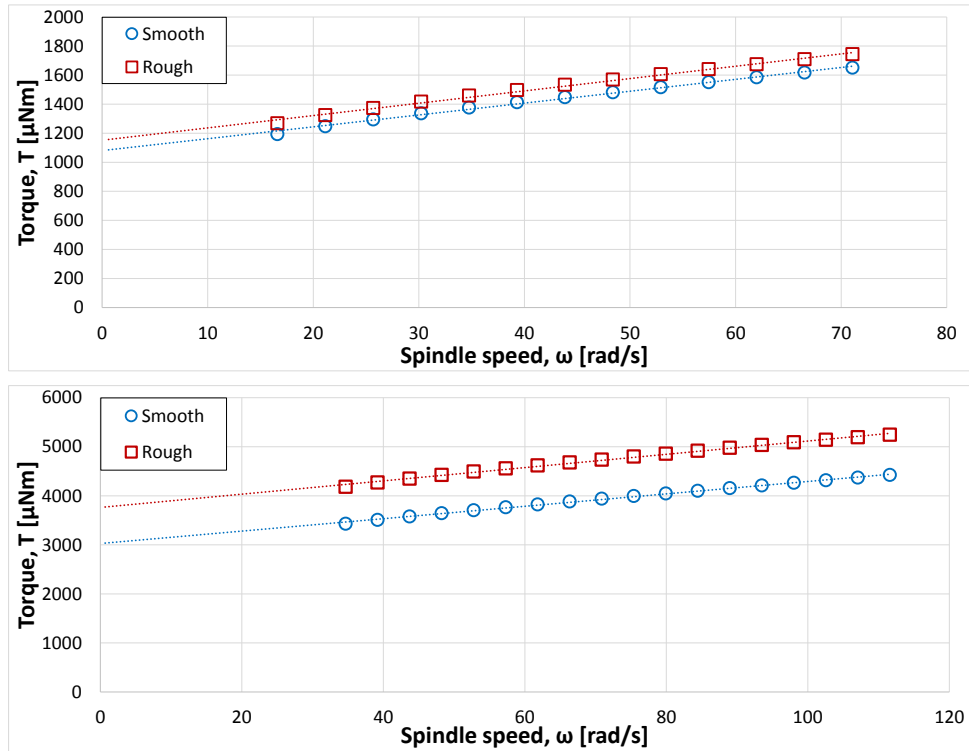


Figure 4.11: Comparison of rheology measurements using smooth and roughened spindles. Error due to slip was minor at 35 wt%, but became more apparent 42 wt%.

Table 4.2: Comparison of rheological parameters obtained using smooth vs. roughened geometry.

35 wt%	Smooth	Rough	% Difference
$\mu_p$ [mPa·s]	11.97	12.60	5.0%
$\tau_B$ [Pa]	19.25	20.45	5.8%
$\varepsilon_{HLC}$ [W/kg]	7.8	8.2	4.9%
<hr/>			
42 wt%	Smooth	Rough	% Difference
$\mu_p$ [mPa·s]	19.01	19.84	4.2%
$\tau_B$ [Pa]	53.47	67.02	20.2%
$\varepsilon_{HLC}$ [W/kg]	32.9	37.6	12.5%

experimental iterations. The present study examined the rheology of the suspensions once for every 3 re-aggregation tests. To ensure the initial rheological properties of each test case are well defined and representative, suspension rheology could be measured prior to every re-aggregation trial. However, bulk suspension volume and testing time requirements would increase proportionally. Changes in bulk suspension properties over time for one sample are provided in [Appendix D](#).

## 4.6 Shear-Induced Kaolinite Re-aggregation

This section presents the key results from the re-aggregation experiments. First, results from the base condition of the study are used to draw a link between torque measurements, aggregate structure, and energy dissipation rate. Next, the maximum torque increase achievable at each tested condition is compared, showing which structures under which conditions display the most potential for restructuring and re-formation after breaking. A connection is then established between initial suspension rheological measurements, and the energy dissipation required to maximize re-aggregation for all test cases. Finally, the theory developed from these experimental results is applied to an independent study, and seeks to clarify previously unexplained results.

### 4.6.1 Relationship between re-aggregation and energy dissipation rate

[Figure 4.12](#) presents the torque recovered over a 300 second conditioning interval as a function of non-dimensionalized energy dissipation rate,  $\varepsilon_{HLC}$ , for the base case of this study. The base case suspension was composed of 35 wt% kaolinite at an unadjusted pH of 4.3. Calcium coagulant was added at a ratio of 0.1% on a dry clay mass basis. A strong relationship is implied between re-aggregation and energy dissipation:  $\Delta T_{Cond.}$  over 300 seconds of conditioning increases as the energy dissipation rate approaches  $\varepsilon_{HLC}$ , then quickly falls as  $\varepsilon_{HLC}$  is surpassed. Michaels and Bolger [40] stated that when aggregate structures undergo a variation in size under shear, shear stress response will continue to change until a steady state is reached. Treinen et al. [24] and Gillies et al. [22] concluded the decrease in torque response in a suspension under shear was directly

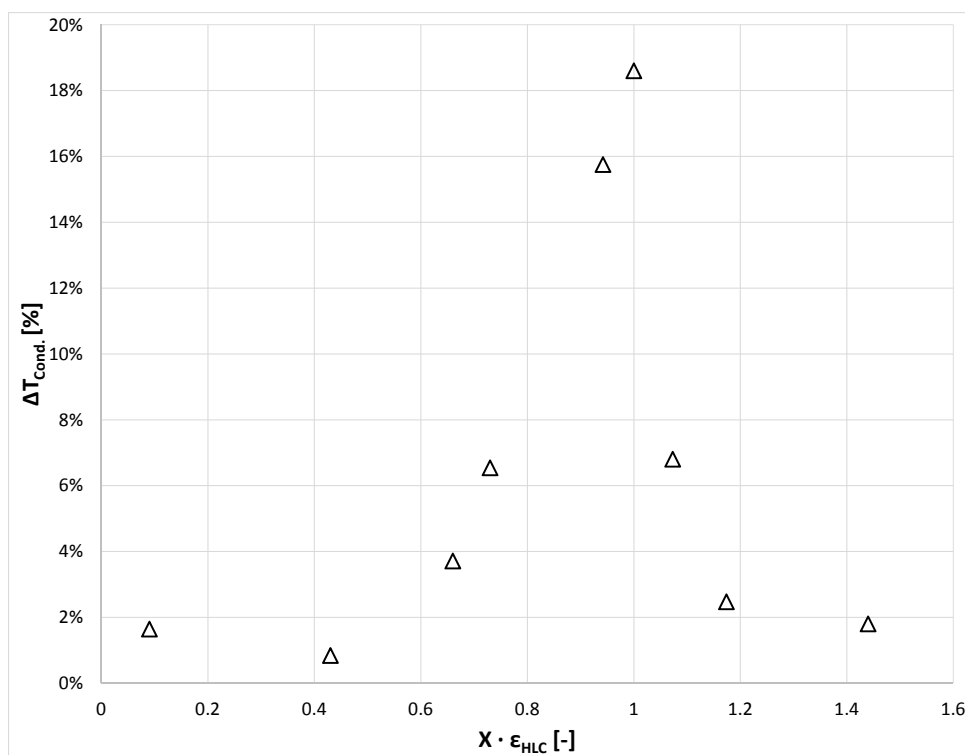


Figure 4.12: Torque increase as a function of non-dimensionalized energy dissipation rate,  $\epsilon_{HLC}$ , for 35 wt% kaolinite suspension.

caused by a reduction in rheology. In Figure 4.12, below  $0.6\epsilon_{HLC}$  and above  $1.2\epsilon_{HLC}$  minimal  $\Delta T_{Cond.}$  is observed. Below  $0.6\epsilon_{HLC}$ , the shear energy is seemingly insufficient to alter the weakly connected aggregates and primary flocs produced during the breakdown phase of testing. When energy dissipation rate is increased above  $1.2\epsilon_{HLC}$ , new connections between fractured aggregates are only able to form in short-lived transitional states, and rapidly break to a state of primary flocs. In both these regimes, less than 2% change in torque over 300 seconds is an indication that existing aggregate structures are not modified in any meaningful way, and re-aggregation is not taking place. Trends similar to those observed in Figure 4.12 were seen in all test cases, and is further discussed in Section 4.6.3.

Between  $0.6$  and  $1.2\epsilon_{HLC}$ , the shear energy is sufficient to fracture some existing aggregate structures, but not all. Fragments of these broken structures then have the opportunity to undergo repeated cycles of collision, aggregate formation, and breakdown until all structures formed are able to resist further fracturing at the presented rate of shear energy dissipation. In other words, an equilibrium state is reached. Suspensions becoming

more resistant to flow at constant shear rate is due to a change in aggregate structure. Both Shamirzadi [55] and Neelakantan et al. [63] have concluded that the apparent volume fraction of aggregates determines both the viscosity and the yield stress of a suspension. Therefore, torque increase indicates that aggregate structures are growing in response to shear. Conditioning the base case kaolinite suspension at  $\varepsilon_{HLC}$  induced the most effective re-aggregation: a 19% increase in torque over 300 seconds. Allowing the structures to reach their equilibrium state at this energy dissipation rate results in a torque increase of 42% after a period of 3000 seconds.

Scanning Electron Microscope (SEM) images of cryo-vitrified kaolinite aggregates obtained at the beginning and end of equilibrium conditioning reveal the shear-induced re-structuring in Figure 4.13. The two SEM images show an identical 35 wt% kaolinite suspension before (left) and after (right) shearing at  $\varepsilon_{HLC}$  for 3000 seconds, and maximum re-aggregation was expected. Equivalent magnification is used for both images. Figure 4.13(A) shows kaolinite aggregate structure immediately after a breakdown phase. The individual flocs are small but densely packed. Based on torque readings, these structural

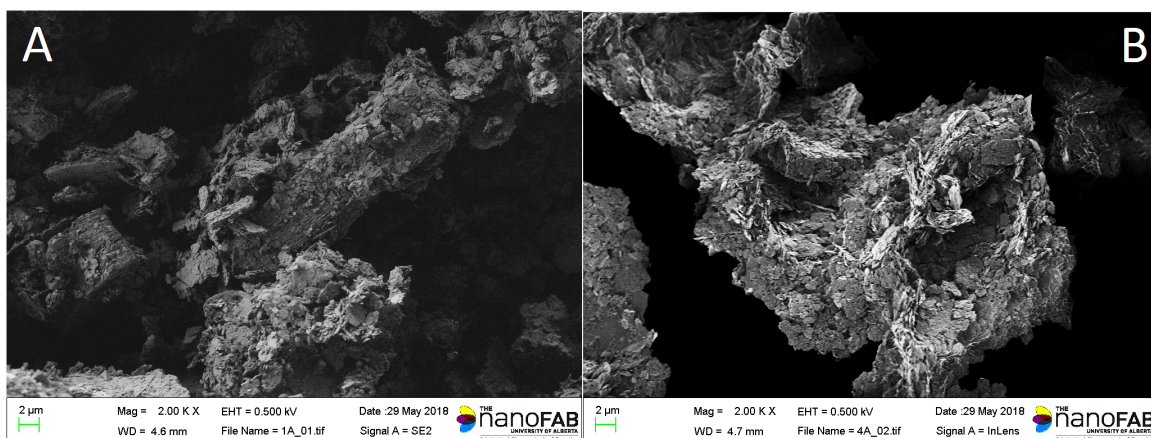


Figure 4.13: SEM characterization at 2000X magnification shows differences in kaolinite aggregate structure (A) before and (B) after exposure to 3000 seconds at  $\varepsilon_{HLC}$ .

elements were broken down as much as possible. Further magnification in Figure 4.14 clearly shows the structure of these flocs, with an abundance of face/face structures visible. This is consistent with results from Vaezi [26], who measured a significant decrease in the particle size distribution of dilute aggregate structures upon shearing. The relatively low rheometer torque response following the breakdown phase is due to the small apparent

volume fraction of aggregates in this state [40]. At structural equilibrium, shown in Figure 4.13(B), the majority of kaolinite particles have agglomerated into a few large aggregates. The smaller face/face oriented flocs predominant in Figure 4.13A have been covered up as these structures continue to grow by random collision. In this state, more particle edge/face “cardhouse” structures are seen, and the void fraction of the overall structure is higher. This evolution of kaolinite structure to larger aggregates of lower density after exposure to conditioning shear agrees well with previous findings by Vaezi [26]. The increase to apparent volume fraction through the more porous aggregate structure explains the increased resistance to shear [40].

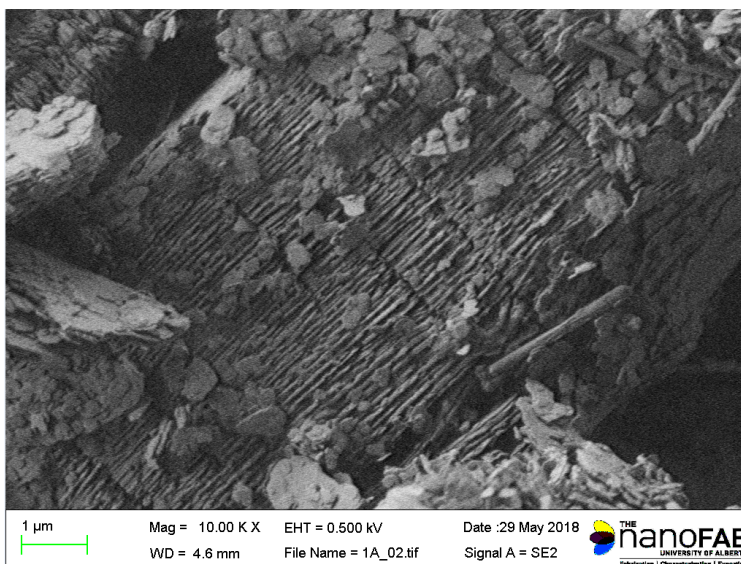


Figure 4.14: 10,000X magnification shows an abundance of face/face particle orientation in small kaolinite flocs following structural breakdown.

#### 4.6.2 Maximum torque increase achieved through conditioning

As described previously, for the 35 wt% base case suspension, the maximum torque increase over a 300 second conditioning phase was 19%. Graphs similar to Figure 4.12 were produced for each of the other conditions tested in this study. The maximum torque increase achieved for each case is summarized in Figure 4.15. Maximum achievable torque increase can also be considered to be the *re-aggregation potential* of a sample, or how amenable it is to structural reformation after fracture.

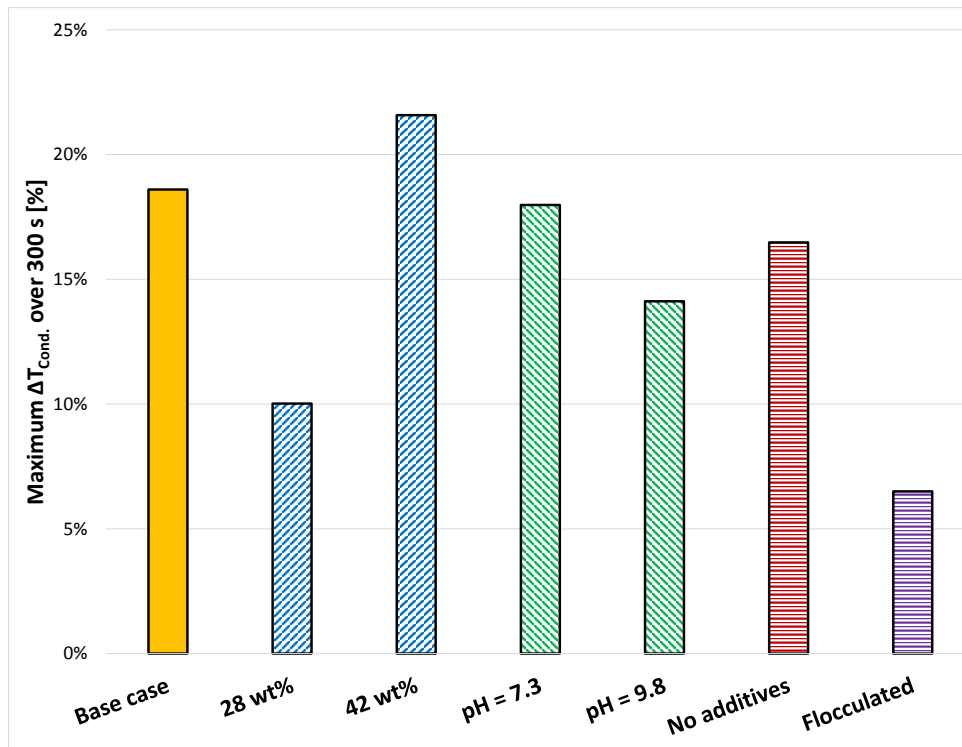


Figure 4.15: Maximum increase in torque achievable over a 300 second conditioning phase for the conditions tested in this study.

At low kaolinite mass fraction, re-aggregation was not very effective. The maximum torque increase achieved was only 10%, just over half of the base case. This is likely due to the decrease in the frequency of inter-particle collisions at lower solid concentration. For particles in flow, the probability of collision is dependent on  $\phi_F$ , the volume fraction of flocs [40]. At low solids fraction,  $\phi_F$  is diminished, leading to fewer expected collisions. The same reasoning explains the higher re-aggregation potential of the 42 wt% sample, for which the maximum torque increase was 22% over 300 seconds. As pH became increasingly alkaline, there was an accompanying decrease in the potential for structural re-growth. At a suspension pH of 7.3 maximum  $\Delta T_{Cond.}$  was 18% over 300 seconds. When pH was further increased to 9.8, maximum  $\Delta T_{Cond.}$  decreased to 14%. Lowering the suspension pH causes the dispersed clay edge surfaces to become negatively charged [44], and intensifies the pH-independent negative charge on the face surface, which results in more pronounced EDL repulsion [45]. Although the absence of di-hydrated calcium chloride coagulant did not significantly affect the Bingham parameters of kaolinite suspensions at low pH,

shearing tests results show that adding the coagulant increased the re-structuring potential of the suspension, as expected. When the coagulant was omitted from the suspension, maximum  $\Delta T_{Cond.}$  over 300 seconds decreased to 16% from 19%.  $Ca^{2+}$  is responsible for collapsing the electric double layer [49], allowing short range attractive Van der Waals forces to dominate [48], and improving kaolinite particle face to edge stacking potential. As a result, more collisions between aggregates would result in the successful formation of new aggregates. Finally, even though the solids fraction of the flocculated kaolinite was 40 wt%, the re-aggregation potential was lowest of all. The maximum torque increase for the flocculated samples was a mere 6.5%. During the pre-shear of the flocculated suspension, polymer links are broken [22, 24]. It is suspected that the fragmented flocculant remains adsorb on to and form a coating on solids particles, giving rise to steric repulsion between polymer overdosed surfaces [58] and hindering re-aggregation.

### 4.6.3 Connection between re-aggregation and rheology

To establish the connection between re-aggregation and energy dissipation rate under all tested cases, the normalized increase in torque during conditioning was plotted as a function of multiples of  $\epsilon_{HLC}$  in Figure 4.16. The multiple of  $\epsilon_{HLC}$  required to achieve maximum torque increase at each experimental condition was then summarized in Figure 4.17, and emphasizes a critical observation. Each kaolinite suspension examined in this study had unique rheological properties. Each showed distinct time-dependent behaviour, HLC and re-aggregation potential. Yet despite the differences in the suspensions, maximum re-aggregation was consistently obtained at an energy dissipation rate of, or within 15% of  $\epsilon_{HLC}$ .

For kaolinite suspensions showing shear history dependent behaviour, a connection has been established between suspension rheology, and the energy dissipation required for re-aggregation through the HLC reference point. This shows that not only can broken structures be induced to reform through shearing, the energy input requirements to do so can be determined from rheological measurements — a relatively simple bench-scale test.

#### 4.6. SHEAR-INDUCED KAOLINITE RE-AGGREGATION

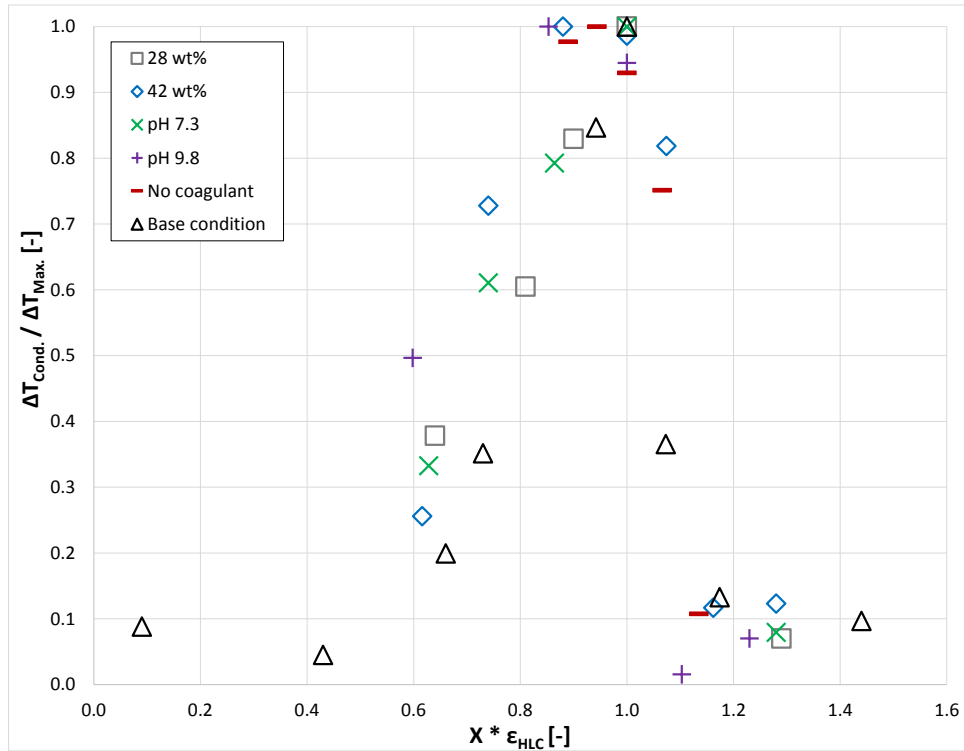


Figure 4.16: Comparison of torque increase by shear conditioning at various multiples of  $\epsilon_{HLC}$  for all tested sample conditions.

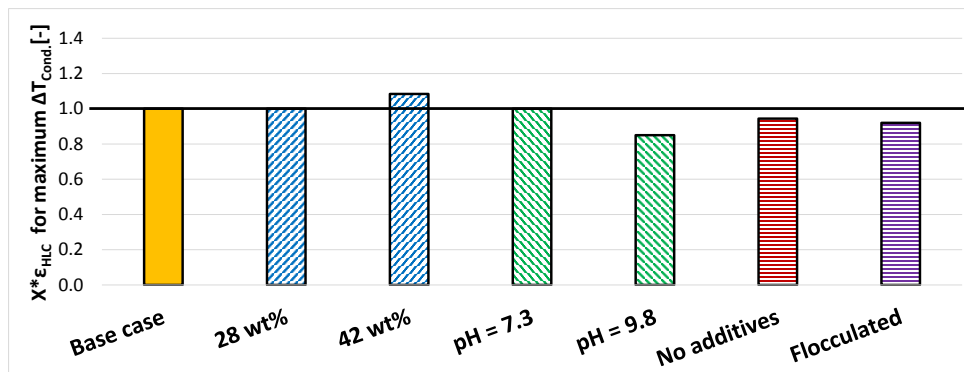


Figure 4.17: Multiple of  $\epsilon_{HLC}$  required to achieve maximum re-aggregation for all tested sample conditions.

#### 4.6.4 Application of theory to pipe flow results

In 2003, Litzenberger [51] conducted a study on the rheological parameters of concentrated kaolinite suspensions. The author unexpectedly observed a continuous increase in pipe line pressure drop, which persisted over several hours of flow. Pressure drop data from Litzenberger [51]’s study is reproduced in Figure 4.18. The effect was attributed to an increase in the rheological parameters of the suspension, but remained unexplained at the time. However, laboratory investigation ruled out any changes to pH, calcium ion concentration, electrophoretic mobility, or individual particle size.

The theoretical connection between suspension rheology, energy dissipation rate and structural change developed in the present study was applied to Litzenberger [51]’s pipe flow results. Viscometer data from Litzenberger [51]’s study was re-analyzed, and the calculated  $\varepsilon_{HLC}$  was compared to the rate of energy dissipation in the pipe loop. It was found that for all cases where the irreversible increase in rheology occurred, the energy dissipation rate due to pipe wall shear fell between  $0.51-1.3\varepsilon_{HLC}$ . In other words, the previously unexplained increase in rheological parameters from Litzenberger [51]’s study was observed to occur in the range of energy dissipation values where shear-induced re-aggregation is expected. Despite differences in geometry, applying the re-aggregation theory developed in this research provided a plausible suggestion for the previously unexplained thickening effect — though the increase in rheological parameters observed in pipe flow were significantly greater than what was achievable in Taylor-Couette flow.

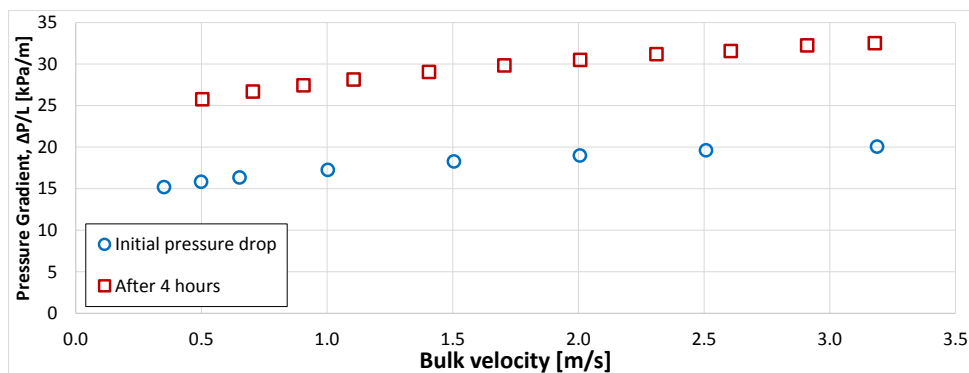


Figure 4.18: Continuous increase in pipeline pressure drop observed in pipe flow of concentrated kaolinite mixture. Reproduced from Litzenberger [51].

The re-aggregation of colloidal particle structures in pipe flow merits further investigation. The sample calculations for the determination of  $\varepsilon_{HLC}$  and pipe flow energy dissipation in Litzenberger [51]'s study are provided in [Appendix E](#).

## 4.7 Summary

This chapter presents results which illustrate a clear relationship between energy input, and both the re-aggregation and breakdown of microscopic kaolinite particle structures by shear. This relationship depends on the energy dissipation rate at the hysteresis loop closure point ( $\varepsilon_{HLC}$ ), a feature inherent to the rheogram of any shear history-dependent fluid. For all samples tested, constant exposure to  $\varepsilon_{HLC}$  resulted in the maximum re-aggregation of broken structures. Operating at  $2\varepsilon_{HLC}$  was shown to reduce the size of aggregates as much as possible. Finally, since re-structuring relies on collisions of flocs, samples with the highest solids fraction showed the greatest re-aggregation potential. However, when polymer flocculants were introduced, steric repulsion significantly hindered the level of restructuring possible.

The theory developed in this study was applied in the analysis of pipe flow tests. Shear-induced re-aggregation was offered as an interpretation for a previously unexplained increase in rheological parameters during flow. Despite the difference in geometry, calculation of pipe flow energy dissipation rate was found to fall within a range where re-aggregation can be expected to occur. Currently, the rheology reduction of thickened tailings due to shear in pipeline transport presents a challenge to tailings management. The ability to reverse aggregate breakdown would be highly beneficial to the oil sands industry. The results from this study indicate that the reformation of colloidal structures is possible, predictable, and warrants further investigation.

## Chapter 5

# Conclusion and Recommendations for Future Work

### 5.1 Conclusions

The main objectives of this study were to examine the shear history-dependent behaviour of kaolinite clay suspensions, and establish a method to induce the re-formation of aggregate structures following their rupture due to shear. The investigation was conducted using a concentric cylinder rheometer, both to obtain rheological data, and to input precise levels of shear energy into suspensions. The effects of varying solids concentration, suspension pH, and coagulant and flocculant dosage on rheology and re-aggregation potential were quantified.

The key findings of this work can be summarized as:

- Shear energy input was determined as a facilitator to the re-formation of fractured aqueous kaolinite aggregates. In all samples tested, it was demonstrated that specific constant rheometer shear rates were able to cause an increase to a shear-history dependent suspension's resistance to flow. The most likely explanation for this rheology increase was a growth of aggregate size and increase in apparent aggregate volume fraction, which is supported by SEM characterization and previous results reported in literature.

- Solids content is an important determining factor in the potential of a suspension to undergo re-aggregation. The most concentrated suspensions studied were 22% more resistant to shearing after just 300 seconds of conditioning at the appropriate rate of energy dissipation.
- As expected, the use of a calcium coagulant resulted in an overall increase in the ability of a suspension to re-aggregate by reducing inter-particle surface forces. However, polymer-amended suspensions were not receptive to shear-induced restructuring, even at high solids fraction. Repulsive forces between polymer-saturated surfaces was the most likely explanation.
- Increasing pH had a mild impact on re-aggregation. As suspensions become more alkaline, repulsive electric double layer forces dominate over the entire surface of kaolinite particles. As a result, the potential for re-formation of ruptured aggregates diminishes as pH is increased from 4.3 to 9.8.
- The hysteresis loop closure point — present in all rheograms showing shear history-dependent behaviour — was established as a key point of reference for determining the energy input required to achieve re-aggregation. Through extensive testing, it was found that exposing a suspension to a rate of energy dissipation equivalent to that at the hysteresis loop closure invariably resulted in good re-aggregation behaviour. This observation was independent of the initial suspension properties and conditions. Moreover, applying twice the energy dissipation rate of the reference point reduced the aggregate suspension to primary flocs, and further increases to shear rate did not produce any further decrease to floc size.
- The theory of re-aggregation developed in this research was applied in the analysis of an independent study's pipe flow results, and provided a plausible interpretation for a previously unexplained increase to rheological parameters.

## 5.2 Recommendations for future work

1. It is recommended that more experimental runs be completed following the procedures developed in this study. Further runs under a broader range of  $\epsilon_{HLC}$  multiples investigated in the present research would help to solidify the understanding of kaolinite structural behaviour as a function of energy input. More pH conditions should also be tested, especially at values closer to true industrial tailings.
2. SEM characterization provided interesting insight into the evolution of aggregate structures through shear conditioning, and is worthwhile to repeat. Due to the fragile, brittle nature of the cryo-vitrified kaolinite and the subsequent difficulty in loading the SEM stubs, improvements to the procedure can potentially be made by drying the suspension on fine filter paper. Since only a miniscule surface is required for SEM imaging, the dried clay can be fractured to expose the structure immediately prior to loading. Making this procedure change should also improve the carbon coat attachment and allow for images with higher clarity.
3. In the current study, changes to aggregate size were interpreted from torque measurements. Although SEM characterization was used to visualize changes to kaolinite aggregate structure change, they cannot be used as a direct measurement of size. Future studies in the same vein should investigate re-aggregation in larger volumes, so that non-invasive particle size measurements such as FBRM may be used. Furthermore, large sample volumes would allow for vane measurements to determine true suspension yield stress.
4. Future work, if conducted in Taylor-Couette flow, should take greater pains to avoid and eliminate wall slip errors. This can be done by using grooved cylinders. Incorporating use of the vane geometry to impart shear should also be considered.
5. The present study only investigated re-aggregation in a rheometer. Although results from previous study support evidence of aggregate growth in pipe geometry, the effect was only observed as an unintended consequence. It is recommended that efforts be undertaken to repeat the re-aggregation study in a pipe loop to determine

if structural re-formation of aggregates can also be predicted as a function of  $\epsilon_{HLC}$ , and if the maximum re-aggregation potential is affected by the new geometry. Furthermore, it is important to examine the re-aggregation of real industrial tailings, which contain bitumen, coarse particles, and other chemicals, which may impact the potential for fractured fines to re-structure.

6. It is well established that polymer-amended tailings are particularly susceptible to shear degradation during pipe flow. If the re-formation of industrial tailings fine aggregates can be proven effective in pipe geometry, it would be worthwhile to investigate the deferment of flocculant dispensation for in-line thickening. The advantages to delaying polymer injection to the final portion of the tailings pipeline are twofold: It ensures the structures to be flocculated have the larger size and higher yield stress granted by re-aggregation, and minimizes the breakdown of polymers through exposure to shear.
7. Finally, although this study was undertaken in the context of industrial oil sand tailings transport, the findings could have far-reaching implications for other colloidal systems. Further tests using similar methodology on other rheopectic suspensions could yield valuable insights for other applications where growth in aggregate size is desired.

# References

- [1] Government of Alberta. [Alberta Oil Sands Facts and Statistics](#), (2018).
- [2] CAPP and Canadian Association of Petroleum Producers. [Crude Oil Forecast, Market and Transportation](#). Technical report, Canadian Association of Petroleum Producers, (2017).
- [3] Canada's Oil Sands. [Recovering the Oil](#), (2018).
- [4] R. S. Sanders, J. Schaan, R. Hughes, C. Shook, W. Crescent, and S. Albert. [Performance of sand slurry pipelines in the oil sands industry](#). *The Canadian Journal of Chemical Engineering*, 82(August):850–857, (2004).
- [5] J. Masliyeh, J. Czarnecki, and Z. Xu. *Handbook on Theory and Practice of Bitumen Recovery from Athabasca Oil Sands Volume 1: Theoretical Basis*. Kingsley Knowledge Publishing, (2011).
- [6] Suncor Energy Inc. [Report on Sustainability 2018](#). Technical report, Suncor Energy Inc., Calgary, Canada, (2018).
- [7] Canadian Association of Petroleum Producers. [Canada's Oil Sands: Water](#), (2018).
- [8] CAPP. Frequently used statistics. Technical report, Canada's Oil and Natural Gas Producers, (2018).
- [9] J. Ellis. [Directive 085](#). Technical Report October, Alberta Energy Regulator, Calgary, (2016).
- [10] D. Mcfadyen. Directive 074. Technical Report February, Energy Resources Conservation Board, Calgary, (2009).
- [11] Alberta Research Council. Clay tailings from Alberta oil sands and other sources : a review. Technical report, Alberta Research Council, Edmonton, Canada, (1978).
- [12] O. Omotoso, R. J. Mikula, and P. W. Stephens. Surface Area of Interstratified Phyllosilicates in Athabasca Oil Sands From Synchrotron XRD. *Advances in X-ray Analysis*, 45:391–396, (2002).

- [13] L. Kotlyar, H. Kodama, and J. Ripmeester. Possible Identification of Poorly Crystalline Inorganic Matter Present in Athabasca Oil Sands. *Applied Clay Science*, 5:1–12, (1990).
- [14] J. Scott, M. Dusseault, and W. Carrier. Behaviour of the Clay/Bitumen/Water Sludge System from Oil Sands Extraction Plants. *Applied Clay Science*, 1:207–218, (1985).
- [15] P. Mercier, Y. Le Page, Y. Tu, and L. Kotlyar. [Powder X-Ray Diffraction Determination of Phyllosilicate Mass and Area Versus Particle Thickness Distributions for Clays from the Athabasca Oilsands NRC Publications Archive \( NPArc \) Archives des publications du CNRC \( NPArc \) Powder x-ray diffraction de](#). *Petroleum Science and Technology*, 26:307–321, (2008).
- [16] E. Cloutis, M. Gaffey, and T. Moslow. Characterization of Minerals in Oil Sands by Reflectance Spectroscopy. *Fuel*, 74(6):874–879, (1995).
- [17] R. N. Yong and A. J. Sethi. [Mineral Particle Interaction Control of Tar Sand Sludge Stability](#). *Journal of Canadian Petroleum Technology*, 17(4):76–83, (1978).
- [18] F. W. Camp. [Processing Athabasca Tar Sands — Tailings Disposal](#). *The Canadian Journal of Chemical Engineering*, 55(5):581–591, (1977).
- [19] X. Yuan and W. Shaw. [Novel Processes for Treatment of Syncrude Fine Transition and Marine Ore Tailings](#). *Canadian Metallurgical Quarterly*, 43(3):265–272, (2013).
- [20] A. S. Michaels and J. C. Bolger. [Particle interactions in aqueous kaolinite dispersions](#). *Industrial and Engineering Chemistry Fundamentals*, 3(1):14–20, (1964).
- [21] J. Schaan, R. Sanders, R. Gilles, M. McKibben, C. Litzenberger, R. Sun, and C. Shook. Effects of Shear History on the Flow Properties of Flocculant-Dosed, Thickened Tailings Slurries. *Hydrotransport 16*, pages 403–414, (2004).
- [22] R. Gillies, R. Spelay, R. Sun, A. Goldszal, and C. Li. Pipeline Transport of Thickened Oil Sands Tailings. In *International Oil Sands Tailings Conference*, page 15, Edmonton, Canada, (2012).
- [23] R. Neelakantan. *Effect of Shear Energy Input on the Rheology of Flocculant- Dosed Kaolinite Suspensions*. Msc, University of Alberta, (2016).
- [24] J. Treinen, R. Cooke, and C. Salinas. Energy Induced Rheology Reduction of Flocculated Slurries. *18th Int. Conf. Hydraulic Transport of Solids*, pages 487–499, (2010).
- [25] C. Salinas, R. Martinson, R. Cooke, and O. Ferrada. Shear and Rheology Reduction for Flocculated Thickened Tailings. *Paste*, (2009).
- [26] F. G. Vaezi. *Effect of Laminar Shear on the Aggregate Structure of Flocculant- dosed Kaolinite Slurries*. Phd, University of Alberta, (2013).

- 
- [27] M. A. Yukselen and J. Gregory. [The reversibility of floc breakage](#). *International Journal of Mineral Processing*, 73(2-4):251–259, (2004).
- [28] J. Gregory. Monitoring floc formation and breakage. *Water Science and Technology*, 50(12):163–170, (2004).
- [29] B. Derakhshandeh. [Kaolinite suspension as a model fluid for fluid dynamics studies of fluid fine tailings](#). *Rheologica Acta*, 55(9):749–758, (2016).
- [30] N. de Nevers. *Fluid Mechanics for Chemical Engineers*. McGraw-Hill, New York, 3rd edition, (2005).
- [31] R. B. Bird, W. E. Stewart, and E. N. Lightfoot. *Transport Phenomena*. John Wiley & Sons, Singapore, 2nd edition, (2005).
- [32] D. C. Bogue and J. L. White. *Engineering Analysis of Non-Newtonian Fluids*. Harford House, London, (1970).
- [33] R. Sanders. Course Notes - CHE 614: Introduction to Fluid-Particle Systems, (2018).
- [34] C. Litzenberger and R. Sumner. Flow Behavior of Kaolin Clay Slurries. In *Hydrotransport 16*, pages 77–91, Santiago, Chile, (2004). BHR Group.
- [35] J. Mewis and N. J. Wagner. [Thixotropy](#). *Advances in Colloid and Interface Science*, 147-148(C):214–227, (2009).
- [36] H. Barnes. [Thixotropy - A review](#). *Journal of non-Newtonian fluid mechanics*, 70(97):1–33, (1997).
- [37] L. Schramm. Colloid Rheology. In *Emulsions, Foams, Suspensions, and Aerosols: Microscience and Applications*, chapter 6, pages 209–258. John Wiley & Sons, Inc., 2 edition, (2018).
- [38] H. Green and R. N. Weltmann. [Equations of Thixotropic Breakdown for the Rotational Viscometer](#). *Industrial and Engineering Chemistry - Analytical Edition*, 18(3):167–172, (1946).
- [39] T. Divoux, V. Grenard, and S. Manneville. [Understanding rheological hysteresis in soft glassy materials](#). *Physical Review Letters*, 110, (2013).
- [40] A. S. Michaels and J. C. Bolger. [The plastic flow behavior of flocculated kaolin suspensions](#). *Industrial and Engineering Chemistry Fundamentals*, 1(3):153–162, (1962).
- [41] S. Yariv and H. Cross. *Geochemistry of Colloid Systems for Earth Scientists*. Springer-Verlag, Berlin, (1979). ISBN 3-540-08980-2.

- [42] BGC Engineering Inc. [Oil Sands Tailings Technology Review](#). Technical report, Oil Sands Research and Information Network, University of Alberta, School of Energy and the Environment, Edmonton, Alberta, (2010).
- [43] A. S. Michaels and J. C. Bolger. [Settling rates and sediment volumes of flocculated kaolin suspensions](#). *Industrial and Engineering Chemistry Fundamentals*, 1(1):24–33, (1962).
- [44] M. S. Nasser and A. E. James. [Settling and sediment bed behaviour of kaolinite in aqueous media](#). *Separation and Purification Technology*, 51(1):10–17, (2006).
- [45] S. Johnson, G. Franks, P. Scales, D. Boger, and T. Healy. [Surface chemistry-rheology relationships in concentrated mineral suspensions](#). *International Journal of Mineral Processing*, 58(1-4):267–304, (2000).
- [46] J. N. Israelachvili. *Intermolecular and Surface Forces*. Elsevier Inc., Santa Barbara, USA, 3rd edition, (2011). ISBN 9780123751829.
- [47] H.-J. Butt, K. Graf, and M. Kappl. *Physics and Chemistry of Interfaces*. Wiley, Weinheim, (2003). ISBN 3527404139.
- [48] P. F. Luckham and S. Rossi. [Colloidal and rheological properties of bentonite suspensions](#). *Advances in Colloid and Interface Science*, 82(1):43–92, (1999).
- [49] M. G. Cacace, E. M. Landau, and J. J. Ramsden. The Hofmeister series: salt and solvent effects on interfacial phenomena. *Quarterly Reviews of Biophysics*, 30(3):241–277, (1997).
- [50] J. Lyklema. [Coagulation by multivalent counterions and the Schulze-Hardy rule](#). *Journal of Colloid and Interface Science*, 392(1):102–104, (2013).
- [51] C. G. Litzenger. [Rheological Study of Kaolin Clay Slurries](#). Msc thesis, University of Saskatchewan, (2003).
- [52] F. Mietta, C. Chassagne, and J. C. Winterwerp. [Shear-induced flocculation of a suspension of kaolinite as function of pH and salt concentration](#). *Journal of Colloid and Interface Science*, 336(1):134–141, (2009).
- [53] M. S. Zbik, R. S. C. Smart, and G. E. Morris. [Kaolinite flocculation structure](#). *Journal of Colloid and Interface Science*, 328(1):73–80, (2008).
- [54] V. Gupta, M. A. Hampton, J. R. Stokes, A. V. Nguyen, and J. D. Miller. [Particle interactions in kaolinite suspensions and corresponding aggregate structures](#). *Journal of Colloid and Interface Science*, 359(1):95–103, (2011).

- [55] A. Shamirzadi. *The Effect of Fine Flocculating Particles and Fine Inerts on Carrier Fluid Viscosity*. Msc, University of Alberta, (2012).
- [56] J. Gregory and S. Barany. *Adsorption and flocculation by polymers and polymer mixtures*. *Advances in Colloid and Interface Science*, 169(1):1–12, (2011).
- [57] J. A. Kitchener. *Principles of Action of Polymeric Flocculants*. *British Polymer Journal*, 4(September 1971):217–229, (1972).
- [58] S. Biggs. *Steric and Bridging Forces between Surfaces Bearing Adsorbed Polymer: An Atomic Force Microscopy Study*. *Langmuir*, 11(1):156–162, (1995).
- [59] A. Chu, T. Paradis, V. Wallwork, and J. Hurdal. *Non Segregating Tailings at the Horizon Oil Sands Project*. In *International Oil Sands Tailings Conference*, pages 3–12, Edmonton, Alberta, (2008).
- [60] S. Jeeravipoolvarn, J. Scott, R. Chalaturnyk, W. Shaw, and N. Wang. *Sedimentation and Consolidation of In-Line Thickened Fine Tailings*. In *International Oil Sands Tailings Conference*, pages 209–223, Edmonton, Alberta, (2008).
- [61] F. G. Vaezi, R. S. Sanders, and J. H. Masliyah. *Flocculation kinetics and aggregate structure of kaolinite mixtures in laminar tube flow*. *Journal of Colloid and Interface Science*, 355(1):96–105, (2011).
- [62] R. Cooke. *Thickened and Paste Tailings Pipeline Systems : Design Procedure – Part 1. Paste*, pages 1–10, (2006).
- [63] R. Neelakantan, F. Vaezi G., and R. S. Sanders. *Effect of shear on the yield stress and aggregate structure of flocculant-dosed, concentrated kaolinite suspensions*. *Minerals Engineering*, 123(November 2017):95–103, (2018).
- [64] I. Reich and R. D. Vold. *Flocculation-Deflocculation in Agitated Suspensions. I. Carbon and Ferric Oxide in Water*. *J. Physcial Chemistry*, 63(10):1497–1501, (1959).
- [65] S. Mason and W. Bartok. Chapter 2. In C. Mill, editor, *Rheology of Disperse Systems*, chapter 2. Pergamon Press, London, (1956).
- [66] J. Duan and J. Gregory. *Coagulation by hydrolysing metal salts*. *Advances in Colloid and Interface Science*, 100-102(SUPPL.):475–502, (2003).
- [67] Y. Chu, B. Gao, Q. Yue, and Y. Wang. *Investigation of dynamic processing on aluminum floc aggregation: Cyclic shearing recovery and effect of sulfate ion*. *Science in China, Series B: Chemistry*, 51(4):386–392, (2008).
- [68] P. Jarvis, B. Jefferson, and S. Parsons. *The duplicity of floc strength*. *Water Science and Technology*, 50(12):63–70, (2004).

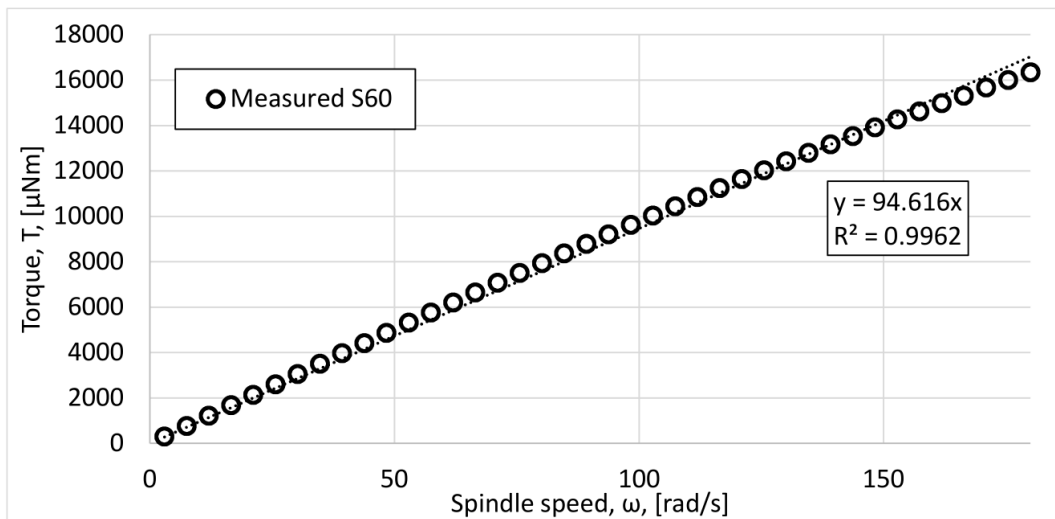
- [69] J. Gregory and V. Dupont. Properties of flocs produced by water treatment coagulants. *Water Science and Technology*, 44(10):231–236, (2001).
- [70] Q. Q. Lin, H. Peng, Q. Q. Lin, and G. Yin. [Formation, breakage and re-formation of flocs formed by cationic starch](#). *Water Science and Technology*, 68(6):1352–1358, (2013).
- [71] K. McCurdy, K. Carlson, and D. Gregory. [Floc morphology and cyclic shearing recovery: Comparison of alum and polyaluminum chloride coagulants](#). *Water Research*, 38(2):486–494, (2004).
- [72] T. Kim and H. Park. [Controlling floc sizes in a pipe between pump and membrane inlet](#). *Desalination*, 249(3):960–968, (2009).
- [73] C. A. Shook and M. Roco. *Slurry Flow: Principles and Practice*. Butterworth-Heinemann, Boston, (1991). ISBN 0-7506-9110-7.
- [74] J. L. Smith. *Measurement of Carrier Fluid Viscosities for Oil Sand Extraction and Tailings Slurries*. Msc, University of Alberta, (2013).
- [75] R. Buscall, J. I. McGowan, and A. J. Morton-Jones. [The rheology of concentrated dispersions of weakly attracting colloidal particles with and without wall slip](#). *Journal of Rheology*, 37(4):621–641, (1993).
- [76] H. Barnes. [A review of the slip \(wall depletion\) of polymer solutions, emulsions and particle suspensions in viscometers: its cause, character, and cure](#). *Journal of Non-Newtonian Fluid Mechanics*, 56(3):221–251, (1995).
- [77] H. A. Barnes and Q. D. Nguyen. Rotating vane rheometry — a review. *Journal of non-Newtonian fluid mechanics*, 98:1–14, (2001).
- [78] C. Chang and P. A. Smith. [Rheological characterization of nuclear waste slurries](#). *Particulate Science and Technology*, 14(2):165–180, (1996).
- [79] Q. Nguyen and D. Boger. Measuring the Flow Properties of Yield Stress Fluids. *Victoria*, pages 47–88, (1992).
- [80] T. Kiljański. [A method for correction of the wall-slip effect in a Couette rheometer](#). *Rheologica Acta*, 28(1):61–64, (1989).
- [81] S. Van Kao, L. E. Nielsen, and C. T. Hill. [Rheology of concentrated suspensions of spheres. I. Effect of the liquid-solid interface](#). *Journal of Colloid And Interface Science*, 53(3):358–366, (1975).
- [82] S. B. Savage and S. McKeown. [Shear stresses developed during rapid shear of concentrated suspensions of large spherical particles between concentric cylinders](#). *Journal of Fluid Mechanics*, 127:453–472, (1983).

- 
- [83] H. Green. [High-Speed Rotational Viscometer of Wide Range Confirmation of the Reiner Equation of Flow](#). *Industrial and Engineering Chemistry - Analytical Edition*, 14 (7):576–585, (1942).
- [84] G. Cokelet, E. Merrill, E. Gilliland, H. Shin, A. Britten, and R. Wells. [The rheology of human blood—measurement near and at zero shear rate](#). *Journal of Rheology*, 7(1):303, (1963).
- [85] Q. Nguyen and D. Boger. [Yield Stress Measurement for Concentrated Suspensions](#). *Journal of Rheology*, 27(1983):321, (1983).
- [86] Q. Nguyen and D. Boger. [Direct Yield Stress Measurement with the Vane Method](#). *Journal of Rheology*, 29(3):335, (1985).
- [87] D. Fisher, S. Clayton, D. Boger, and P. Scales. [The bucket rheometer for shear stress-shear rate measurement of industrial suspensions](#). *Journal of Rheology*, 51(5):821–831, (2007).
- [88] H. Rahman. *Yield Stresses of Mixtures with Bimodal Size Distributions*. Msc, University of Alberta, (2011).
- [89] EPCOR. *Summary of Major Chemicals, Microbiological, and Physical Parameters of Edmonton Drinking Water Produced at Water Treatment Plants*. Technical Report May, EPCOR, Edmonton, (2018).
- [90] M. Marefatallah. *Effect of Sonication on the Particle Size of Kaolinite Clays*. Msc, University of Alberta, (2013).

# Appendix A

## Rheometer calibration data

Standard oil:	S60	Rheometer specifications:	
Geometry	Concentric cylinder	Spindle radius [mm]:	14
Test temperature [°C]:	20	Cup radius [mm]:	15.2
Standard viscosity, 20°C [mPa.s]:	139.3	Spindle length [mm]:	42.03
Measured viscosity, 20°C [mPa.s]:	138.6	Sample volume [mL]:	24
Error [%]:	0.488%	Operating gap [mm]:	5.7



## **Appendix B**

# **Safe work procedures**

## B.1 Safe Work Procedure for preparing 35 wt% kaolinite suspension

Location: Lab 2-156, CME Building

<b>Job title:</b> 35% kaolinite suspension preparation	<b>Last Updated:</b> March 2018
<b>Written by:</b> Simon Sun	<b>Conducted by:</b> Simon Sun
<b>Required protective equipment:</b> Safety glasses, nitrile gloves, lab coat, full length pants, closed toe shoes	
<b>Hazards present:</b> Dust inhalation Care should be taken in the handling of any samples to avoid spilling, broken glassware, and creating a messy work environment.	
<b>First aid measures:</b> No extraordinary first aid measures are relevant for kaolinite suspension. Sperian disposable dust masks are available on the shelf by the front door. Antiseptic wash, gauze pads, adhesive tapes, bandage, instant cold pack, spill kit, burn relief gel are available in the first-aid kit. Eye wash station is located at the lab sink.	

The following step-by-step procedure is used to prepare 35 wt% kaolinite suspension, and remove entrained air from the sample. For different solids concentrations, the mass of kaolinite weighed in step 2 should be adjusted accordingly. To ensure consistency, all kaolinite for any group of experiments should be taken from the same bulk bag purchased from the supplier.

	<b>Instructions</b>	<b>Additional Comments</b>
0	Ensure all glassware is cleaned with detergent, rinsed with DI water, and dried before use.	The presence of ions such as calcium and magnesium commonly found in tap water will introduce undocumented effects in aggregate formation.
1	In a 600 mL beaker, weigh 400 g DI water on laboratory scale and set aside.	
2	Calculate the mass of kaolinite clay powder (A) required to produce a suspension of known solids concentration using the following formula: $A = \frac{400 \times M}{(1 - M)}$ where M is the desired solids weight fraction.	For 35 wt% kaolinite suspension, 215.38 g kaolinite should be weighed.
3	Weigh the mass of clay calculated as A in a separate beaker.	Sperian disposable dust mask should be worn when handling dry clay.
4	Weigh the appropriate mass of CaCl <sub>2</sub> 2H <sub>2</sub> O (B) on a piece of clean weighing paper: $B = 0.001A$	Based on a mass ratio of CaCl <sub>2</sub> 2H <sub>2</sub> O : kaolinite = 0.1%
5	Transfer the CaCl <sub>2</sub> 2H <sub>2</sub> O to the DI water beaker. Stir to dissolve.	

6	Using a small scoop, slowly transfer kaolin into water and allow it to settle.	Sperian disposable dust mask should be worn when handling dry clay. Care must be taken not to generate unnecessary dust.
7	Seal the beaker containing clay suspension, and allow it to remain overnight.	Parafilm is located on the shelf at the rear of the laboratory.

Some amount of air entrainment during sample preparation is inevitable, and causes errors during rheometer operation. For fluids such as kaolinite suspensions which exhibit a yield stress, entrained air does not naturally escape. The following steps detail the procedure used to remove entrained air.

	<b>Instructions</b>	<b>Additional Comments</b>
1	Unseal the beaker, and mix the suspension using the 45° pitched bladed turbine (PBT) impeller on overhead mixer to re-suspend the solids. Impeller should be set to approximately 800 rpm. Mix continuously for 5 minutes.	Moving the impeller around the sample is useful for ensuring all solids are re-integrated into a homogeneous suspension.
2	Wash and dry a 1000 mL side-arm filter flask and connect the side-arm to the vacuum pump using rubber tubing. Add a 1.5" magnetic stir bar. Place filter flask on magnetic mixer.	Ensure hot plate function is turned off. Hot plate is not required in kaolinite suspension preparation.
3	Using a funnel, gently transfer homogeneous clay suspension to filter flask.	Care should be taken not to cause splashing, as this will waste sample.
4	Stopper the filter flask and turn on vacuum pump and magnetic mixer. Bubbles of entrained air will begin to form.	Magnetic mixer speed should be set at a range where no vortex is formed, but the suspension is adequately agitated. 300 rpm is typically an appropriate value, but may need to be adjusted accordingly.
5	Periodically rotate the position of the magnetic stir bar to increase coverage, and gently swirl the flask by hand. Repeat until no more bubbles appear on the surface.	Air removal typically takes 30 minutes.
6	Gently pour the de-aired sample into a clean, dry beaker.	Ensure the magnetic stir bar does not fall into the beaker.
7	Place the 45°PBT in the center of the de-aired, homogenous sample, with 1 cm clearance from the container bottom. Slowly increase the impeller speed until the suspension is fully mixed, but no vortex is formed.	
8	Measure the suspension using a freshly calibrated pH probe. If necessary, adjust the pH by dropwise addition of aqueous NaOH or HCl.	Mixer should be turned off before inserting pH probe into the sample. Never use the probe to stir the sample.
9	Allow the sample to be mixed continuously for at least 1 hour.	The sample can now proceed to rheometer measurement.

Waste disposal instructions:

0	All waste should be placed in a bucket or other sealable container with properly fitting lid. Content labels should be prepared and affixed to lid and container	Ensure lid is secured on the waste bucket before leaving the lab.
1	When waste bucket is nearing full, contact Simon with the following information: Size of bucket Amount of waste Type of waste Contents on waste bucket (by percentage)	Clearly state all chemicals, especially potentially reactive or toxic substances
2	Once the Chematix slip is prepared, inform Simon that waste is available for pickup.	

Once experiment is completed, tidy the lab area. Wash all equipment and hang on drying rack. Ensure all waste is properly labelled and placed in the appropriate waste disposal area. Contact Simon to inform him of waste that needs to be disposed.

Simon Sun

Ph: xxx-xxx-xxxx

E-mail: xxxxxxxx@ualberta.ca

## B.2 Safe Work Procedure for rheometer operation

Location: Lab 2-156, CME Building

<b>Job title:</b> AR-G2 and DHR-2 Rheometer Operation	<b>Last Updated:</b> August 2018
<b>Written by:</b> Simon Sun	<b>Conducted by:</b> Simon Sun
<b>Required protective equipment:</b> Safety glasses, nitrile gloves, lab coat, full length pants, closed toe shoes	
<b>Hazards present:</b> No major hazards to personnel inherent to rheometer operation. Care should be taken in the handling of any samples to avoid spilling, broken glassware, or other sample specific dangers such as toxic chemicals	
<b>First aid measures:</b> No extraordinary first aid measures are relevant for kaolinite suspension. Antiseptic wash, gauze pads, adhesive tapes, bandage, instant cold pack, spill kit, burn relief gel are available in the first-aid kit. Eye wash station is located at the lab sink.	

A step-by-step procedure detailing rheometer testing is as follows:

	<b>Instructions</b>	<b>Additional Comments</b>
1	Open valve to rheometer air supply and ensure pressure is set at 32 psi.	Low air pressure does not properly support the magnetic bearing and causes serious damage to the instrument
2	Remove bearing lock from rheometer and ensure the spindle bearing moves freely.  <b>Important:</b> Always tighten or loosen the spindle shaft or bearing lock from above! The magnetic bearing on the bottom is extremely sensitive to minute disturbances.	If the bearing lock is not removed, the initial torque applied can cause breakage or twisting. As a result the shape and/or angle of this part will change. Measurement will be impossible or with huge errors.
3	Turn on computer, rheometer and temperature control system. Open instrument software and ensure computer and instrument communication is initiated. Check liquid level in the temperature control reservoir.	The water level in the reservoir must be full up to the lower part of the neck. If it is not enough, use de-ionized water to top up. If there is insufficient water, fatal damage to the instrument will occur within 4 hours.
4	Calibrate rheometer <b>without</b> any attached geometry: calibration menu > calibration tab > calibrate inertia > "Accept"	Avoid any physical disturbance that causes vibration. If there is any background vibration, the system calibration will have major errors

5	Attach conical DIN rotor to rheometer bearing. Geometry menu> select concentric cylinder geometry	Always tighten the shaft from above. Avoid putting any pressure on the geometry as it is sensitive to any minute changes in shape/angle.
6	With the geometry attached, select “inertial calibration”.	Requires 30 seconds
7	Perform “frictional calibration”.	Requires 30 seconds
8	Perform rotational mapping: Calibration menu> rotational mapping tab> precision mapping, 2 iterations> “Calibrate”	Precision mapping with 2 iterations takes 10 minutes to complete.
9	Adjust temperature set-point to desired value. Wait for temperature to reach equilibrium.	Check the temperature reading under the instrument display for a constant value.
10	Perform zero gap measurement. Instrument menu> “Zero Gap Click “Start”.	
11	Experiment menu> create test procedure appropriate for sample	
12	Using a large syringe, add 24 mL of sample to the rheometer cup. Click the green triangular “play” button on the Home menu.	
13	At the end of each test, raise the rotor bearing, remove the rotor and cup. Clean and dry thoroughly.  Important: Always use the “Raise to loading gap” button in the TRIOS software to raise the rheometer head from the sample.	Never lift the geometry manually as the force may warp the rotor and cause damage to the device. Again, always loosen or tighten any attachment from above.
14	When testing is complete turn off computer, rheometer and temperature control system. Replace bearing lock and turn off rheometer air supply. Carefully replace rheometer geometries back into holders.	

## Appendix C

# Rheological data for tested samples

## C.1 Raw data for 35 wt% kaolinite suspension, base case

Raw Data			
Increasing		Decreasing	
Velocity	Torque	Velocity	Torque
rad/s	$\mu\text{N}\cdot\text{m}$	rad/s	$\mu\text{N}\cdot\text{m}$
3.00	925.99	180.00	3014.43
7.54	1049.70	175.46	2957.07
12.08	1129.86	170.92	2907.38
<b>16.62</b>	<b>1192.70</b>	166.38	2841.16
<b>21.15</b>	<b>1247.18</b>	161.85	2779.75
<b>25.69</b>	<b>1293.91</b>	157.31	2715.47
<b>30.23</b>	<b>1336.21</b>	152.77	2653.69
<b>34.77</b>	<b>1375.62</b>	148.23	2590.07
<b>39.31</b>	<b>1412.33</b>	143.69	2541.72
<b>43.85</b>	<b>1447.01</b>	139.16	2486.90
<b>48.38</b>	<b>1481.05</b>	134.62	2404.45
<b>52.92</b>	<b>1515.49</b>	130.08	2324.49
<b>57.46</b>	<b>1550.40</b>	125.54	2241.65
<b>62.00</b>	<b>1583.82</b>	121.00	2142.51
<b>66.54</b>	<b>1617.12</b>	<u>116.46</u>	<u>2059.89</u>
<b>71.08</b>	<b>1650.80</b>	111.92	2037.89
75.62	1685.69	107.38	2018.56
80.15	1721.02	102.85	1997.77
84.69	1757.61	98.31	1974.30
89.23	1796.22	93.77	1948.98
93.77	1836.08	89.23	1922.03
98.31	1876.86	84.69	1892.90
102.85	1919.95	80.15	1862.50
107.38	1964.83	75.62	1830.91
111.92	2012.08	<b>71.08</b>	<b>1798.69</b>
<u>116.46</u>	<u>2060.48</u>	<b>66.54</b>	<b>1765.57</b>
121.00	2127.37	<b>62.00</b>	<b>1732.54</b>
125.54	2227.06	<b>57.46</b>	<b>1698.73</b>
130.08	2324.50	<b>52.92</b>	<b>1664.53</b>
134.62	2404.31	<b>48.38</b>	<b>1629.68</b>
139.15	2489.11	<b>43.85</b>	<b>1594.10</b>
143.69	2561.95	<b>39.31</b>	<b>1556.72</b>
148.23	2575.10	<b>34.77</b>	<b>1517.06</b>
152.77	2616.66	<b>30.23</b>	<b>1476.07</b>
157.31	2692.40	<b>25.69</b>	<b>1432.32</b>
161.85	2753.90	<b>21.15</b>	<b>1384.35</b>
166.39	2825.93	<b>16.62</b>	<b>1329.74</b>
170.92	2886.13	12.08	1265.10
175.46	2942.96	7.54	1182.06
180.00	3017.91	3.00	1049.12

### Rheological Summary

#### Increasing spindle speed

Plastic viscosity, $\mu_p$ , [mPa.s]	12.0
Bingham yield stress, $\tau_B$ , [Pa]	19.2

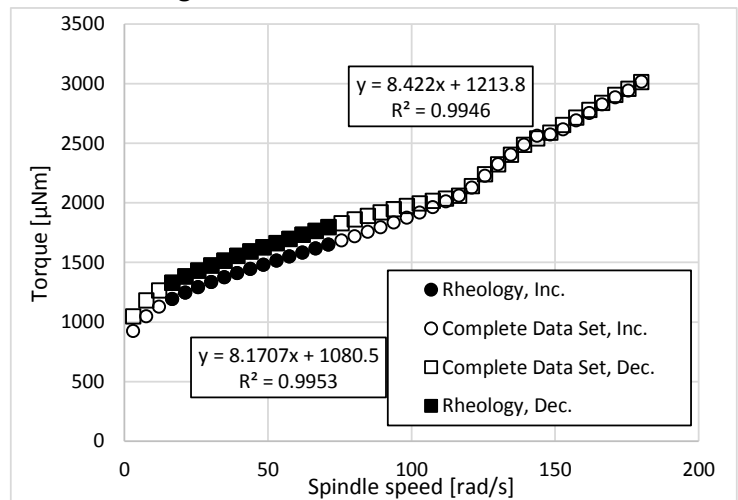
#### Decreasing spindle speed

Plastic viscosity, $\mu_p$ , [mPa.s]	12.3
Bingham yield stress, $\tau_B$ , [Pa]	21.6

$\omega_{\text{HLC}}$  [rad/s] 116.5

$\epsilon_{\text{HLC}}$  [W/kg] 7.7

### Rheogram:



Full data set of increasing and decreasing spindle speeds.

Filled data points indicate subset used for rheological calculations.

## C.2 Raw data for 28 wt% kaolinite suspension

Raw Data			
Increasing		Decreasing	
Velocity	Torque	Velocity	Torque
rad/s	$\mu\text{N}\cdot\text{m}$	rad/s	$\mu\text{N}\cdot\text{m}$
3.00	325.90	180.00	1941.75
7.54	380.10	175.46	1879.29
<b>12.08</b>	<b>417.50</b>	170.92	1835.63
<b>16.62</b>	<b>448.21</b>	166.38	1779.81
<b>21.15</b>	<b>475.20</b>	161.85	1723.35
<b>25.69</b>	<b>499.74</b>	157.31	1668.09
<b>30.23</b>	<b>523.11</b>	152.77	1612.29
<b>34.77</b>	<b>546.60</b>	148.23	1557.12
<b>39.31</b>	<b>569.87</b>	143.69	1502.12
<b>43.85</b>	<b>592.80</b>	139.15	1447.63
<b>48.38</b>	<b>616.13</b>	134.62	1395.08
52.92	639.89	130.08	1344.39
57.46	664.32	125.54	1310.45
62.00	689.42	121.00	1282.10
66.54	715.52	116.46	1234.62
71.08	742.74	111.92	1193.70
<u>75.62</u>	<u>773.46</u>	107.38	1146.36
80.15	847.21	102.85	1104.36
84.69	905.43	98.31	1057.80
89.23	958.22	93.77	1003.62
93.77	986.74	89.23	969.52
98.31	1041.80	84.69	914.44
102.85	1088.47	80.15	856.19
107.38	1131.34	<u>75.62</u>	<u>784.80</u>
111.92	1176.95	71.08	761.05
116.46	1220.07	66.54	741.09
121.00	1266.67	62.00	721.01
125.54	1311.85	57.46	700.08
130.08	1346.40	52.92	678.06
134.62	1406.13	<b>48.38</b>	<b>655.34</b>
139.15	1456.71	<b>43.85</b>	<b>632.22</b>
143.69	1522.56	<b>39.31</b>	<b>608.93</b>
148.23	1596.02	<b>34.77</b>	<b>585.50</b>
152.77	1652.74	<b>30.23</b>	<b>561.46</b>
157.31	1708.76	<b>25.69</b>	<b>536.14</b>
161.85	1764.67	<b>21.15</b>	<b>510.46</b>
166.38	1799.05	<b>16.62</b>	<b>483.13</b>
170.92	1837.79	<b>12.08</b>	<b>452.55</b>
175.46	1890.02	7.54	415.62
180.00	1948.90	3.00	362.08

### Rheological Summary

#### Increasing spindle speed

Plastic viscosity,  $\mu_p$ , [mPa.s] 7.9

Bingham yield stress,  $\tau_B$ , [Pa] 6.4

#### Decreasing spindle speed

Plastic viscosity,  $\mu_p$ , [mPa.s] 8.1

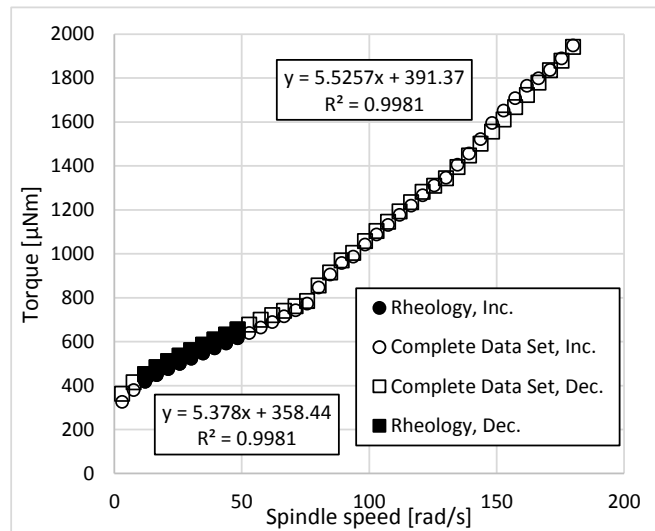
Bingham yield stress,  $\tau_B$ , [Pa] 7.0

#### Hysteresis loop closure

$\omega_{\text{HLC}}$  [rad/s] 75.6

$\epsilon_{\text{HLC}}$  [W/kg] 2.0

### Rheogram:



Full data set of increasing and decreasing spindle speeds.

Filled data points indicate subset used for rheological calculations.

*Bolded data set used for rheology calculations.*

*Underlined values indicate HLC.*

### C.3 Raw data for 42 wt% kaolinite suspension

Raw Data			
Increasing		Decreasing	
Velocity	Torque	Velocity	Torque
rad/s	$\mu\text{N.m}$	rad/s	$\mu\text{N.m}$
3.00	2382.77	270.00	7424.03
7.53	2690.97	265.47	7295.15
12.05	2880.12	260.95	7228.39
16.58	3023.76	256.42	7173.19
21.10	3142.09	251.90	7125.27
25.63	3246.25	247.37	7085.74
<b>30.15</b>	<b>3342.31</b>	242.85	7037.83
<b>34.68</b>	<b>3428.83</b>	238.32	6975.04
<b>39.20</b>	<b>3506.13</b>	233.80	6842.58
<b>43.73</b>	<b>3576.80</b>	229.27	6778.94
<b>48.25</b>	<b>3642.24</b>	224.75	6730.69
<b>52.78</b>	<b>3704.43</b>	220.22	6615.11
<b>57.31</b>	<b>3763.40</b>	215.70	6496.54
<b>61.83</b>	<b>3821.57</b>	211.17	6373.01
<b>66.36</b>	<b>3881.47</b>	206.64	6249.09
<b>70.88</b>	<b>3940.72</b>	202.12	6119.25
<b>75.41</b>	<b>3993.68</b>	197.59	5931.84
<b>79.93</b>	<b>4044.46</b>	193.07	5825.04
<b>84.46</b>	<b>4101.04</b>	<u>188.54</u>	<u>5719.06</u>
<b>88.98</b>	<b>4155.48</b>	184.02	5716.56
<b>93.51</b>	<b>4207.60</b>	179.49	5714.29
<b>98.03</b>	<b>4262.61</b>	174.97	5710.24
<b>102.56</b>	<b>4315.57</b>	170.44	5701.17
<b>107.09</b>	<b>4368.91</b>	165.92	5688.96
111.61	4422.09	161.39	5669.34
116.14	4475.70	156.86	5650.47
120.66	4532.92	152.34	5620.02
125.19	4591.10	147.81	5589.60
129.71	4648.47	143.29	5557.80
134.24	4706.93	138.76	5518.98
138.76	4770.24	134.24	5477.85
143.29	4835.04	129.71	5434.62
147.81	4903.74	125.19	5390.39
152.34	4976.24	120.66	5340.94
156.86	5053.52	116.14	5293.24
161.39	5136.96	111.61	5243.98
165.92	5223.86	<b>107.09</b>	<b>5193.98</b>
170.44	5316.71	<b>102.56</b>	<b>5142.87</b>
174.97	5414.82	<b>98.03</b>	<b>5091.04</b>
179.49	5512.07	<b>93.51</b>	<b>5039.00</b>
184.02	5608.33	<b>88.98</b>	<b>4985.25</b>
<u>188.54</u>	<u>5695.62</u>	<b>84.46</b>	<b>4932.65</b>
193.07	5794.33	<b>79.93</b>	<b>4875.01</b>
197.59	5914.34	<b>75.41</b>	<b>4819.67</b>
202.12	6004.41	<b>70.88</b>	<b>4762.04</b>
206.64	6088.63	<b>66.36</b>	<b>4701.93</b>
211.17	6248.48	<b>61.83</b>	<b>4640.01</b>
215.70	6393.91	<b>57.31</b>	<b>4576.59</b>
220.22	6513.98	<b>52.78</b>	<b>4511.35</b>
224.75	6701.87	<b>48.25</b>	<b>4442.60</b>
229.27	6827.21	<b>43.73</b>	<b>4369.29</b>
233.80	6809.33	<b>39.20</b>	<b>4291.79</b>
238.32	6801.73	<b>34.68</b>	<b>4206.92</b>
242.85	6855.76	<b>30.15</b>	<b>4113.24</b>
247.37	6925.59	25.63	4008.87
251.90	7020.72	21.10	3889.65
256.42	7056.44	16.58	3751.87
260.95	7150.33	12.05	3583.15
265.47	7233.90	7.53	3355.77
270.00	7367.39	3.00	2948.22

#### Rheological Summary

##### Increasing spindle speed

Plastic viscosity, $\mu_p$ , [mPa.s]	19.0
Bingham yield stress, $\tau_B$ , [Pa]	53.5

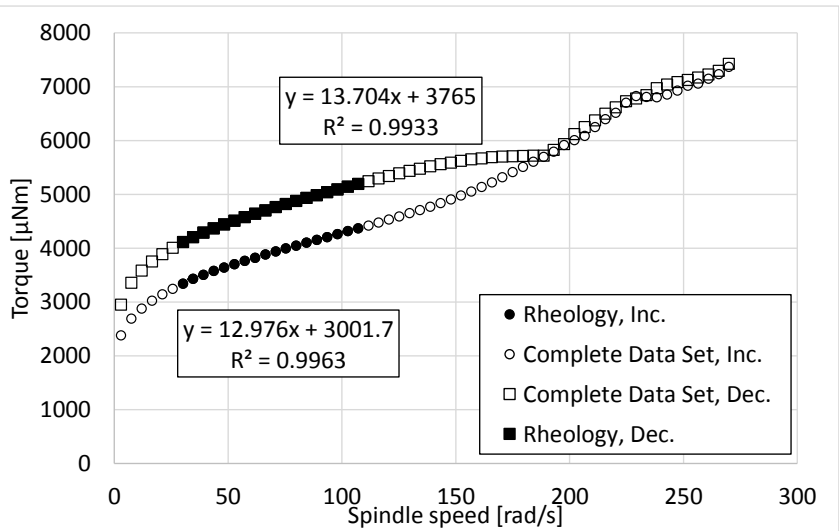
##### Decreasing spindle speed

Plastic viscosity, $\mu_p$ , [mPa.s]	20.1
Bingham yield stress, $\tau_B$ , [Pa]	67.1

##### Hysteresis loop closure

$\omega_{HLC}$ [rad/s]	188.5
$\epsilon_{HLC}$ [W/kg]	32.4

#### Rheogram:



Full data set of increasing and decreasing spindle speeds.

Filled data points indicate subset used for rheological calculations.

*Bolded data set used for rheology calculations.*

*Underlined values indicate HLC.*

## C.4 Raw data for 35 wt% kaolinite suspension, pH = 7.3

Raw Data			
Increasing		Decreasing	
Velocity	Torque	Velocity	Torque
rad/s	$\mu\text{N}\cdot\text{m}$	rad/s	$\mu\text{N}\cdot\text{m}$
3.00	712.57	180.00	2723.54
7.54	813.24	175.46	2672.87
12.08	878.84	170.92	2617.23
<b>16.62</b>	<b>930.95</b>	166.38	2558.55
<b>21.15</b>	<b>975.68</b>	161.85	2500.14
<b>25.69</b>	<b>1015.12</b>	157.31	2443.38
<b>30.23</b>	<b>1052.33</b>	152.77	2376.13
<b>34.77</b>	<b>1086.73</b>	148.23	2319.15
<b>39.31</b>	<b>1119.96</b>	143.69	2258.50
<b>43.85</b>	<b>1152.19</b>	139.15	2187.06
<b>48.38</b>	<b>1184.71</b>	134.62	2116.92
<b>52.92</b>	<b>1217.31</b>	130.08	2071.39
<b>57.46</b>	<b>1249.85</b>	125.54	2013.31
<b>62.00</b>	<b>1282.34</b>	121.00	1936.79
<b>66.54</b>	<b>1315.38</b>	116.46	1859.74
71.08	1349.09	111.92	1790.58
75.62	1384.03	<u>107.39</u>	<u>1688.94</u>
80.15	1419.15	102.85	1639.79
84.69	1456.48	98.31	1617.28
89.23	1494.43	93.77	1595.42
93.77	1534.41	89.23	1571.93
98.31	1576.90	84.69	1546.68
102.85	1619.87	80.15	1520.33
<u>107.39</u>	<u>1674.13</u>	75.62	1492.51
111.92	1755.94	71.08	1463.59
116.46	1835.09	<b>66.54</b>	<b>1433.07</b>
121.00	1911.25	<b>62.00</b>	<b>1402.67</b>
125.54	1989.62	<b>57.46</b>	<b>1371.20</b>
130.08	2033.00	<b>52.92</b>	<b>1339.58</b>
134.62	2091.65	<b>48.38</b>	<b>1307.61</b>
139.15	2157.67	<b>43.85</b>	<b>1275.24</b>
143.69	2219.53	<b>39.31</b>	<b>1242.08</b>
148.23	2290.17	<b>34.77</b>	<b>1207.79</b>
152.77	2365.04	<b>30.23</b>	<b>1172.28</b>
157.31	2418.31	<b>25.69</b>	<b>1134.62</b>
161.85	2487.63	<b>21.15</b>	<b>1093.82</b>
166.39	2545.14	<b>16.62</b>	<b>1048.32</b>
170.92	2602.19	12.08	995.30
175.46	2671.34	7.54	928.76
180.00	2730.63	3.00	826.73

### Rheological Summary

#### Increasing spindle speed

Plastic viscosity,  $\mu_p$ , [mPa.s] 11.0

Bingham yield stress,  $\tau_B$ , [Pa] 14.6

#### Decreasing spindle speed

Plastic viscosity,  $\mu_p$ , [mPa.s] 11.1

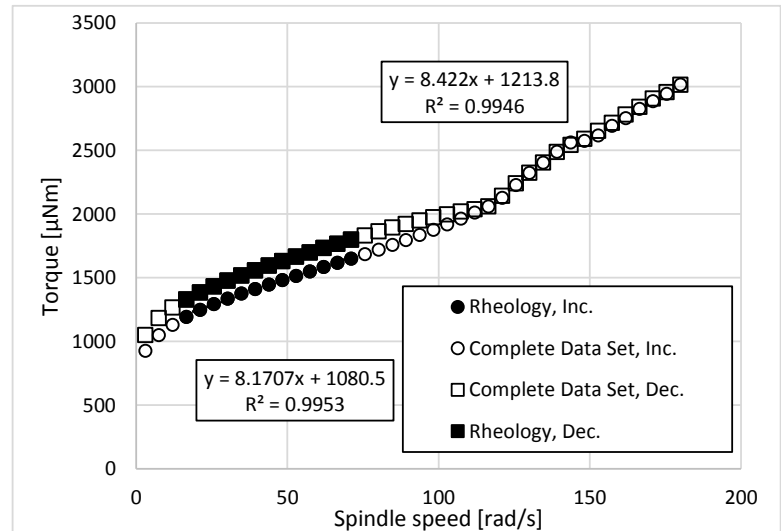
Bingham yield stress,  $\tau_B$ , [Pa] 16.7

#### Hysteresis loop closure

$\omega_{\text{HLC}}$  [rad/s] 107.4

$\epsilon_{\text{HLC}}$  [W/kg] 5.8

### Rheogram:



Full data set of increasing and decreasing spindle speeds.

Filled data points indicate subset used for rheological calculations.

## C.5 Raw data for 35 wt% kaolinite suspension, pH = 9.8

Raw Data			
Increasing		Decreasing	
Velocity rad/s	Torque μN.m	Velocity rad/s	Torque μN.m
3.00	570.41	180.00	2519.80
7.54	646.69	175.46	2422.01
<b>12.08</b>	<b>701.26</b>	170.92	2380.48
<b>16.62</b>	<b>746.04</b>	166.38	2298.34
<b>21.15</b>	<b>784.45</b>	161.85	2250.06
<b>25.69</b>	<b>818.77</b>	157.31	2193.92
<b>30.23</b>	<b>850.63</b>	152.77	2136.83
<b>34.77</b>	<b>880.99</b>	148.23	2063.76
<b>39.31</b>	<b>910.73</b>	143.69	2018.09
<b>43.85</b>	<b>940.21</b>	139.15	1959.88
<b>48.38</b>	<b>969.85</b>	134.62	1903.18
<b>52.92</b>	<b>999.55</b>	130.08	1839.32
<b>57.46</b>	<b>1029.73</b>	125.54	1777.16
62.00	1060.52	121.00	1719.53
66.54	1091.54	116.46	1670.46
71.08	1123.09	111.92	1602.61
75.62	1155.27	107.39	1527.98
80.15	1188.54	102.85	1463.56
84.69	1223.31	98.31	1389.97
89.23	1259.33	<u>93.77</u>	<u>1312.53</u>
<u>93.77</u>	<u>1295.75</u>	89.23	1286.27
98.31	1362.96	84.69	1261.48
102.85	1453.28	80.15	1236.41
107.39	1529.63	75.62	1210.57
111.92	1608.33	71.08	1183.62
116.46	1653.97	66.54	1155.84
121.00	1693.36	62.00	1127.47
125.54	1753.15	<b>57.46</b>	<b>1098.15</b>
130.08	1822.31	<b>52.92</b>	<b>1068.57</b>
134.62	1876.20	<b>48.38</b>	<b>1038.89</b>
139.15	1943.21	<b>43.85</b>	<b>1009.11</b>
143.69	2006.36	<b>39.31</b>	<b>979.75</b>
148.23	2046.61	<b>34.77</b>	<b>949.32</b>
152.77	2108.10	<b>30.23</b>	<b>917.21</b>
157.31	2163.76	<b>25.69</b>	<b>884.72</b>
161.85	2227.96	<b>21.15</b>	<b>850.85</b>
166.39	2303.39	<b>16.62</b>	<b>814.56</b>
170.92	2396.58	<b>12.08</b>	<b>774.02</b>
175.46	2460.23	7.54	725.91
180.00	2518.40	3.00	659.54

### Rheological Summary

#### Increasing spindle speed

Plastic viscosity, $\mu_p$ , [mPa.s]	10.3
Bingham yield stress, $\tau_B$ , [Pa]	11.2

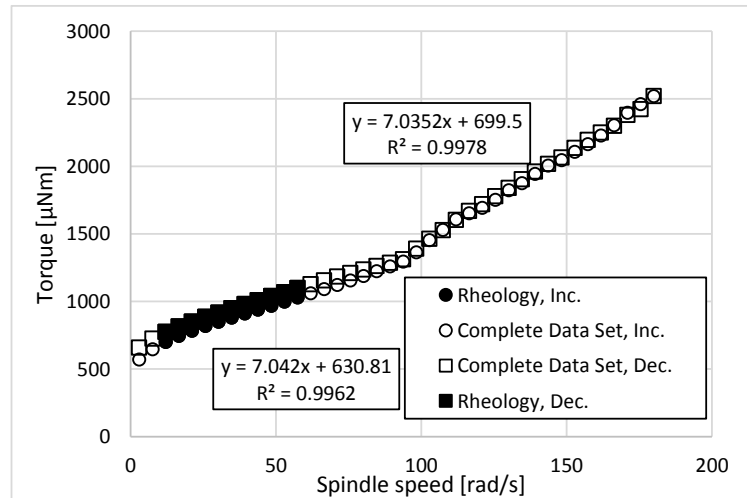
#### Decreasing spindle speed

Plastic viscosity, $\mu_p$ , [mPa.s]	10.3
Bingham yield stress, $\tau_B$ , [Pa]	12.5

#### Hysteresis loop closure

$\omega_{HLC}$ [rad/s]	93.8
$\epsilon_{HLC}$ [W/kg]	3.9

### Rheogram:



Full data set of increasing and decreasing spindle speeds.

Filled data points indicate subset used for rheological calculations.

## C.6 Raw data for 35 wt% kaolinite suspension, no additives

Raw Data			
Increasing		Decreasing	
Velocity	Torque	Velocity	Torque
rad/s	$\mu\text{N}\cdot\text{m}$	rad/s	$\mu\text{N}\cdot\text{m}$
3.00	1097.20	180.00	3367.93
7.54	1240.97	175.46	3286.78
12.08	1334.26	170.92	3159.08
<b>16.62</b>	<b>1406.76</b>	166.39	3085.35
<b>21.15</b>	<b>1468.59</b>	161.85	3064.21
<b>25.69</b>	<b>1522.66</b>	157.31	3010.58
<b>30.23</b>	<b>1569.66</b>	152.77	2960.39
<b>34.77</b>	<b>1613.26</b>	148.23	2871.07
<b>39.31</b>	<b>1653.96</b>	143.69	2779.73
<b>43.85</b>	<b>1691.56</b>	139.15	2689.67
<b>48.38</b>	<b>1727.81</b>	134.62	2600.40
<b>52.92</b>	<b>1763.62</b>	130.08	2485.86
<b>57.46</b>	<b>1799.79</b>	<u>125.54</u>	<u>2414.82</u>
<b>62.00</b>	<b>1835.47</b>	121.00	2395.19
<b>66.54</b>	<b>1869.50</b>	116.46	2376.79
<b>71.08</b>	<b>1903.27</b>	111.92	2356.38
75.62	1937.70	107.38	2333.48
80.15	1973.43	102.85	2308.26
84.69	2010.26	98.31	2280.07
89.23	2047.86	93.77	2249.36
93.77	2085.44	89.23	2217.75
98.31	2122.98	84.69	2185.58
102.85	2163.08	80.15	2152.00
107.39	2206.38	75.62	2118.58
111.92	2251.58	<b>71.08</b>	<b>2084.10</b>
116.46	2301.06	<b>66.54</b>	<b>2049.62</b>
121.00	2349.60	<b>62.00</b>	<b>2014.62</b>
<u>125.54</u>	<u>2399.80</u>	<b>57.46</b>	<b>1979.22</b>
130.08	2468.33	<b>52.92</b>	<b>1943.01</b>
134.62	2546.57	<b>48.38</b>	<b>1906.18</b>
139.15	2675.73	<b>43.85</b>	<b>1867.71</b>
143.69	2762.16	<b>39.31</b>	<b>1827.66</b>
148.23	2855.34	<b>34.77</b>	<b>1785.94</b>
152.77	2946.52	<b>30.23</b>	<b>1741.55</b>
157.31	3006.20	<b>25.69</b>	<b>1693.56</b>
161.85	3040.42	<b>21.15</b>	<b>1639.83</b>
166.39	3049.23	<b>16.62</b>	<b>1578.09</b>
170.92	3107.49	12.08	1504.02
175.46	3200.48	7.54	1408.27
180.00	3270.05	3.00	1252.59

### Rheological Summary

#### Increasing spindle speed

Plastic viscosity, $\mu_p$ , [mPa.s]	12.9
Bingham yield stress, $\tau_B$ , [Pa]	23.0

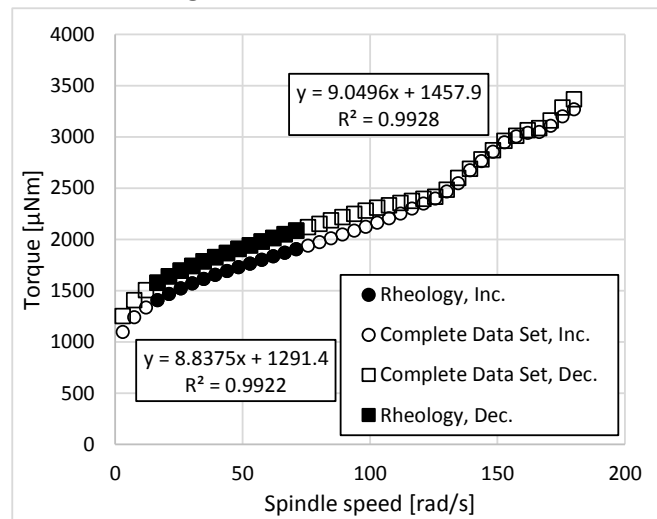
#### Decreasing spindle speed

Plastic viscosity, $\mu_p$ , [mPa.s]	13.3
Bingham yield stress, $\tau_B$ , [Pa]	26.0

#### Hysteresis loop closure

$\omega_{\text{HLC}}$ [rad/s]	125.5
$\epsilon_{\text{HLC}}$ [W/kg]	9.8

### Rheogram:



Full data set of increasing and decreasing spindle speeds.

Filled data points indicate subset used for rheological calculations.

*Bolded data set used for rheology calculations.*

*Underlined values indicate HLC.*

## C.7 Raw data for 40 wt% kaolinite suspension, flocculated

Raw Data			
Increasing		Decreasing	
Velocity	Torque	Velocity	Torque
rad/s	$\mu\text{N.m}$	rad/s	$\mu\text{N.m}$
3.00	2722.84	270.00	8433.48
7.53	3068.87	265.47	8284.43
12.05	3283.44	260.95	8163.96
16.58	3448.73	256.42	8084.74
21.10	3586.43	251.90	8009.50
25.63	3709.93	247.37	8009.91
<b>30.15</b>	<b>3827.51</b>	242.85	7884.81
<b>34.68</b>	<b>3933.11</b>	238.32	7742.67
<b>39.20</b>	<b>4029.77</b>	233.80	7600.61
<b>43.73</b>	<b>4117.49</b>	229.27	7445.21
<b>48.25</b>	<b>4199.19</b>	224.75	7288.27
<b>52.78</b>	<b>4277.36</b>	220.22	7134.81
<b>57.31</b>	<b>4351.75</b>	215.70	6970.07
<b>61.83</b>	<b>4423.56</b>	211.17	6815.52
<b>66.36</b>	<b>4489.73</b>	<u>206.64</u>	<u>6590.97</u>
<b>70.88</b>	<b>4556.50</b>	202.12	6471.08
<b>75.41</b>	<b>4622.38</b>	197.59	6414.56
<b>79.93</b>	<b>4690.72</b>	193.07	6368.12
<b>84.46</b>	<b>4756.19</b>	188.54	6322.52
<b>88.98</b>	<b>4818.50</b>	184.02	6283.25
<b>93.51</b>	<b>4876.88</b>	179.49	6241.10
<b>98.03</b>	<b>4933.50</b>	174.97	6203.82
<b>102.56</b>	<b>4990.20</b>	170.44	6167.82
<b>107.09</b>	<b>5047.09</b>	165.92	6121.40
<b>111.61</b>	<b>5106.49</b>	161.39	6078.99
<b>116.14</b>	<b>5162.62</b>	156.86	6026.92
<b>120.66</b>	<b>5219.60</b>	152.34	5975.31
<b>125.19</b>	<b>5274.84</b>	147.81	5924.74
129.71	5324.59	143.29	5866.49
134.24	5377.55	138.76	5809.44
138.76	5433.57	134.24	5752.98
143.29	5486.58	129.71	5693.97
147.81	5543.21	<b>125.19</b>	<b>5634.54</b>
152.34	5604.94	<b>120.66</b>	<b>5574.91</b>
156.86	5672.57	<b>116.14</b>	<b>5513.83</b>
161.39	5745.85	<b>111.61</b>	<b>5453.04</b>
165.92	5824.32	<b>107.09</b>	<b>5391.48</b>
170.44	5902.50	<b>102.56</b>	<b>5329.84</b>
174.97	5982.13	<b>98.03</b>	<b>5270.28</b>
179.49	6066.42	<b>93.51</b>	<b>5207.31</b>
184.02	6152.14	<b>88.98</b>	<b>5146.42</b>
188.54	6235.99	<b>84.46</b>	<b>5082.91</b>
193.07	6306.95	<b>79.93</b>	<b>5019.91</b>
197.59	6357.33	<b>75.41</b>	<b>4955.96</b>
202.12	6421.50	<b>70.88</b>	<b>4889.84</b>
<u>206.64</u>	<u>6598.85</u>	<b>66.36</b>	<b>4818.34</b>
211.17	6784.75	<b>61.83</b>	<b>4745.72</b>
215.69	6953.28	<b>57.31</b>	<b>4675.92</b>
220.22	7119.51	<b>52.78</b>	<b>4605.24</b>
224.75	7291.82	<b>48.25</b>	<b>4533.32</b>
229.27	7466.29	<b>43.73</b>	<b>4459.11</b>
233.80	7629.97	<b>39.20</b>	<b>4379.66</b>
238.32	7800.49	<b>34.68</b>	<b>4293.03</b>
242.85	7966.75	<b>30.15</b>	<b>4196.82</b>
247.37	8135.64	25.63	4090.16
251.90	8306.10	21.10	3970.17
256.42	8172.07	16.58	3832.01
260.95	8186.68	12.05	3666.65
265.47	8310.34	7.53	3451.25
270.00	8400.87	3.00	3101.29

### Rheological Summary

#### Increasing spindle speed

Plastic viscosity,  $\mu_p$ , [mPa.s] 21.7

Bingham yield stress,  $\tau_B$ , [Pa] 61.9

#### Decreasing spindle speed

Plastic viscosity,  $\mu_p$ , [mPa.s] 21.7

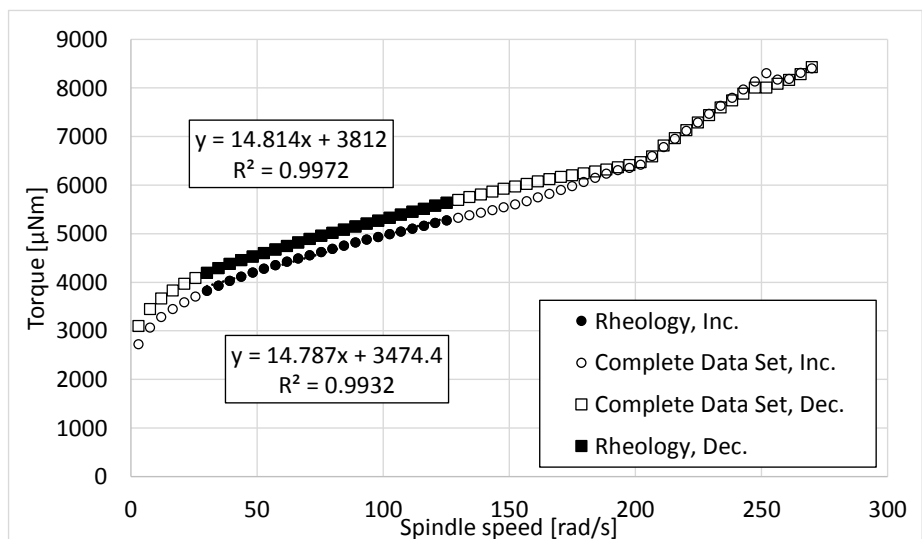
Bingham yield stress,  $\tau_B$ , [Pa] 67.9

#### Hysteresis loop closure

$\omega_{\text{HLC}}$  [rad/s] 206.6

$\epsilon_{\text{HLC}}$  [W/kg] 42.7

### Rheogram:



Full data set of increasing and decreasing spindle speeds.

Filled data points indicate subset used for rheological calculations.

*Bolded data set used for rheology calculations.*

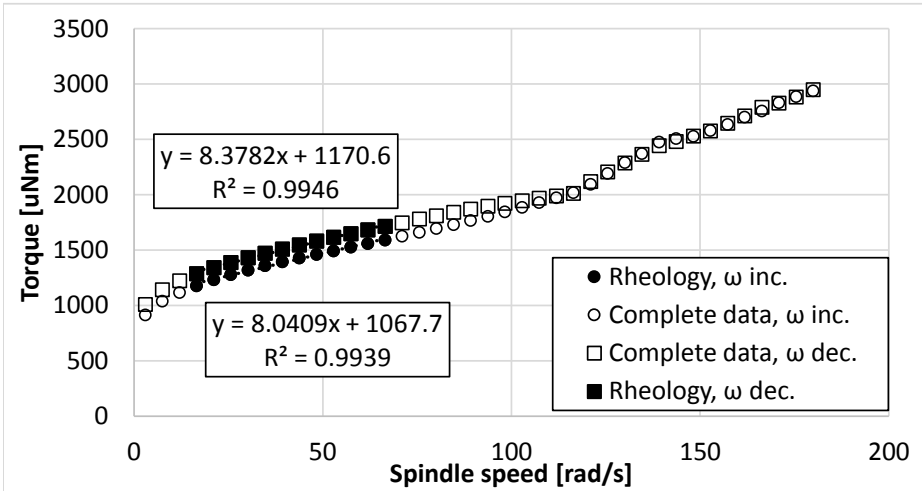
*Underlined values indicate HLC.*

## **Appendix D**

# **Rheological variation of sample over testing period**

## D.1 Rheological variation of 35 wt% kaolinite suspension over 2 hours

Rheology, time = 0 min



Increasing spindle speed

$\mu_p$  (mPa.s): **11.8**

$\tau_B$  (Pa): **19.0**

Decreasing spindle speed

$\mu_p$  (mPa.s): **12.3**

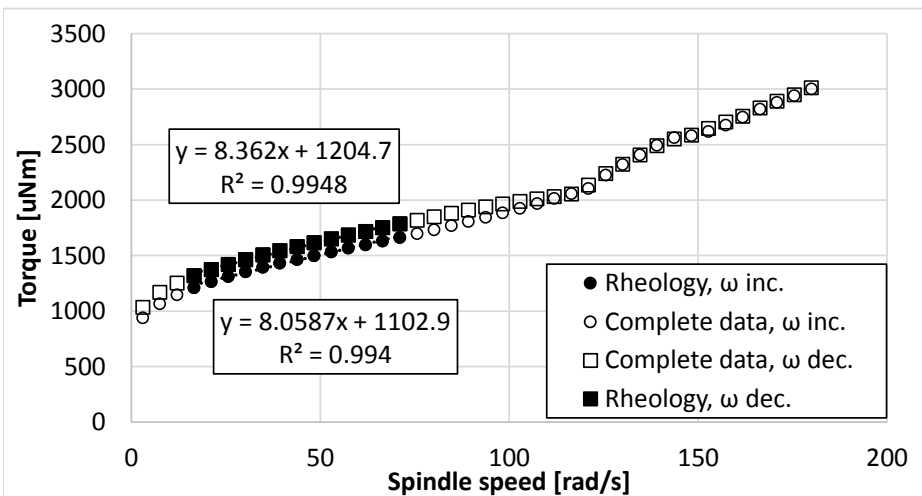
$\tau_B$  (Pa): **20.9**

Hysteresis loop closure

$\omega_{HLC}$  [rad/s]: **116.5**

$\epsilon_{HLC}$  [W/kg]: **7.5**

Rheology, time = 25 min



Increasing spindle speed

$\mu_p$  (mPa.s): **11.8**

$\tau_B$  (Pa): **19.6**

Decreasing spindle speed

$\mu_p$  (mPa.s): **12.3**

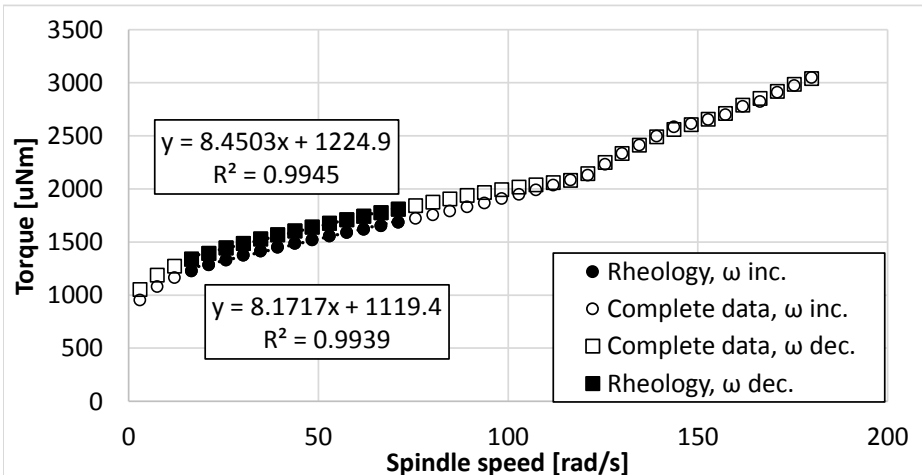
$\tau_B$  (Pa): **21.5**

Hysteresis loop closure

$\omega_{HLC}$  [rad/s]: **116.5**

$\epsilon_{HLC}$  [W/kg]: **7.7**

Rheology, time = 50 min



Increasing spindle speed

$\mu_p$  (mPa.s): **12.0**

$\tau_B$  (Pa): **19.9**

Decreasing spindle speed

$\mu_p$  (mPa.s): **12.4**

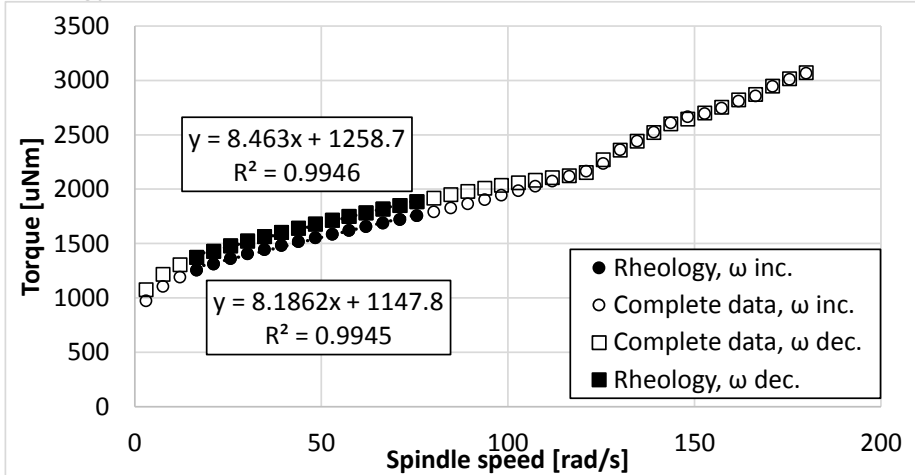
$\tau_B$  (Pa): **21.8**

Hysteresis loop closure

$\omega_{HLC}$  [rad/s]: **116.5**

$\epsilon_{HLC}$  [W/kg]: **7.8**

**Rheology, time = 75 min**



Increasing spindle speed

$\mu$ p (mPa.s): **12.0**  
 $\tau$ B (Pa): **20.4**

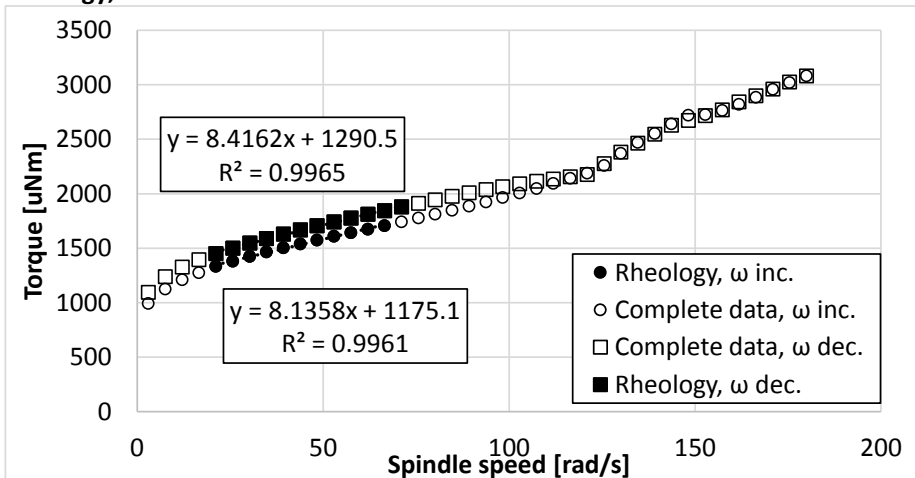
Decreasing spindle speed

$\mu$ p (mPa.s): **12.4**  
 $\tau$ B (Pa): **22.4**

Hysteresis loop closure

$\omega_{HLC}$  [rad/s]: **116.5**  
 $\epsilon_{HLC}$  [W/kg]: **7.9**

**Rheology, time = 97 min**



Increasing spindle speed

$\mu$ p (mPa.s): **11.9**  
 $\tau$ B (Pa): **20.9**

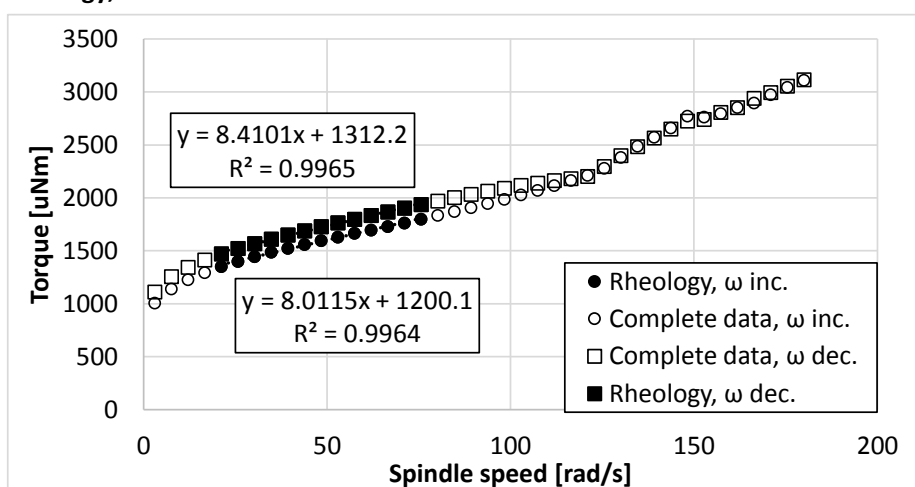
Decreasing spindle speed

$\mu$ p (mPa.s): **12.3**  
 $\tau$ B (Pa): **23.0**

Hysteresis loop closure

$\omega_{HLC}$  [rad/s]: **121.0**  
 $\epsilon_{HLC}$  [W/kg]: **8.5**

**Rheology, time = 117 min**



Increasing spindle speed

$\mu$ p (mPa.s): **11.7**  
 $\tau$ B (Pa): **21.4**

Decreasing spindle speed

$\mu$ p (mPa.s): **12.3**  
 $\tau$ B (Pa): **23.4**

Hysteresis loop closure

$\omega_{HLC}$  [rad/s]: **121.0**  
 $\epsilon_{HLC}$  [W/kg]: **8.6**

## Appendix E

# Sample calculation for energy dissipation in pipeline

This appendix provides a sample calculation which shows the calculation of  $\varepsilon_{HLC}$  and shearing due to pipe flow in the study conducted by Litzenberger [51]. Raw data was obtained from Litzenberger's original thesis, and re-analyzed using the theory developed in this study.

### E.1 Determination of $\varepsilon_{HLC}$ from viscometry data

Table E.1 provides the geometry and suspension specifications obtained from Litzenberger [51]'s study. The suspension was 19 vol% kaolinite (G2000201 / G2000202). Rheograms produced at the initial suspension condition, and the condition after 4 hours of continuous shearing are shown in Figures E.1 and E.2.

The best estimates of the HLC point have been marked. To calculate the energy dissipation rate at HLC, the following equation is used:

$$\varepsilon = \frac{T\omega}{\rho V}$$

where V is the volume of sheared suspension in the Haake MV3 geometry, and assumed to only be the volume between concentric cylinders due to the recessed spindle end. Therefore, for the initial condition:

$$\varepsilon_{HLC, Initial} = \frac{(11340 \mu Nm)(37.91 rad/s)}{(1322.24 kg/m^3)(7.43 mL)}$$

$$\varepsilon_{HLC, Initial} = 43.76 W/kg$$

E.1. DETERMINATION OF  $\epsilon_{HLC}$  FROM VISCOMETRY DATA

Table E.1: Haake RV3 viscometer geometry and kaolinite mixture specifications.

Description	Specification
Spindle radius, $R_1$	20 mm
Cup radius, $R_2$	21 mm
Spindle length, $L$	60 mm
Volume between cylinders, $V$	7.43 mL
Suspension density, $\rho_m$	1322.24 kg/m <sup>3</sup>

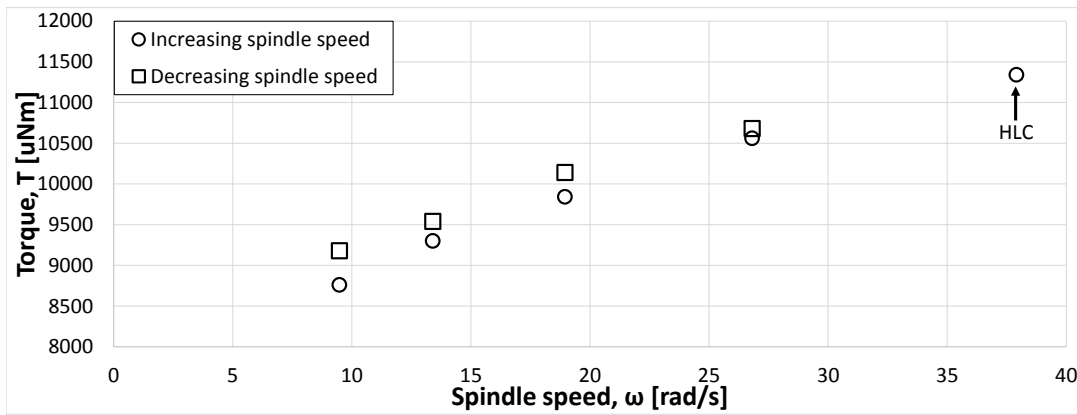


Figure E.1: Viscometer data at initial mixture conditions. Reproduced from Litzenberger [51].

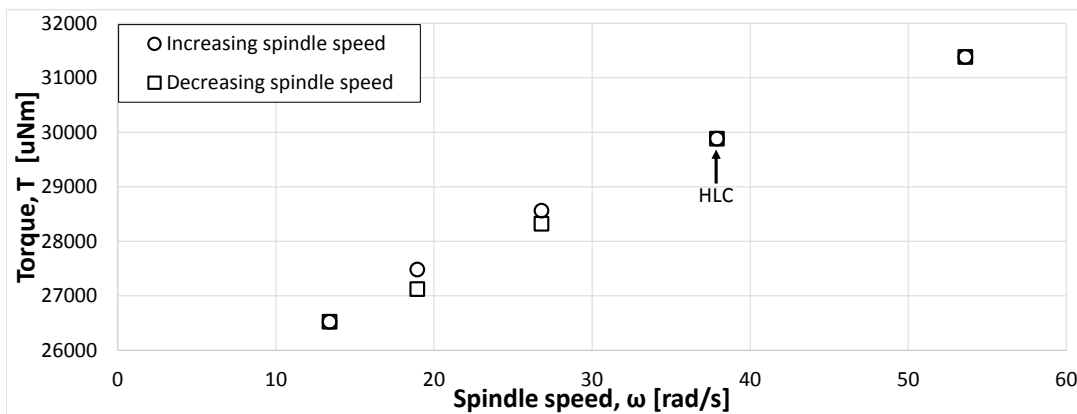


Figure E.2: Viscometer data after 4 hours pipe loop flow. Reproduced from Litzenberger [51].

Similarly, it can be shown that:

$$\varepsilon_{HLC, 4Hrs} = 115.27 \text{ W/kg}$$

## E.2 Determination of shearing from pipe flow

Pipe loop specifications are listed in [Table E.2](#). The total length of pipe was calculated based on the provided pipe diameter and volume, and assumes the entire pipe loop has the same diameter throughout. Pressure drop data is plotted on [Figure E.3](#).

The Mechanical Energy Balance is rearranged to show that:

$$\tau_w = \left( \frac{\Delta P}{L} \right) \frac{D}{4}$$

The following calculation procedure was described in [Section 2.4.1](#). For the initial condition, with a pipe loop superficial velocity ( $V$ ) of 3.2 m/s, the measured pressure drop was 11.0024 kPa/m. Therefore:

$$\tau_w = (11.0024 \text{ kPa/m}) \frac{0.0258 \text{ mm}}{4}$$

$$\tau_w = 70.965 \text{ Pa}$$

Based on the shear stress decay law and a calculated Bingham yield stress of 51.7 Pa, the radius of the unsheared plug is:

$$r_{plug} = \frac{\tau_B}{\tau_w} R_P$$

$$r_{plug} = \frac{51.7 \text{ Pa}}{70.965 \text{ Pa}} (0.0129 \text{ m})$$

$$r_{plug} = 0.00940 \text{ m}$$

The mass of the sheared annulus is:

$$m_{an} = \pi \left( R_P^2 - r_{plug}^2 \right) L \rho$$

Table E.2: Pipe loop geometry specifications.

Description	Specification
Total volume, $V$	11.95 L
Pipe diameter, $D_P$	25.8 mm
Pipe radius, $R_P$	12.9 mm
Flow area, $A_P$	522 mm <sup>2</sup>
Total length (calculated), $L_P$	22.86 m

## E.2. DETERMINATION OF SHEARING FROM PIPE FLOW

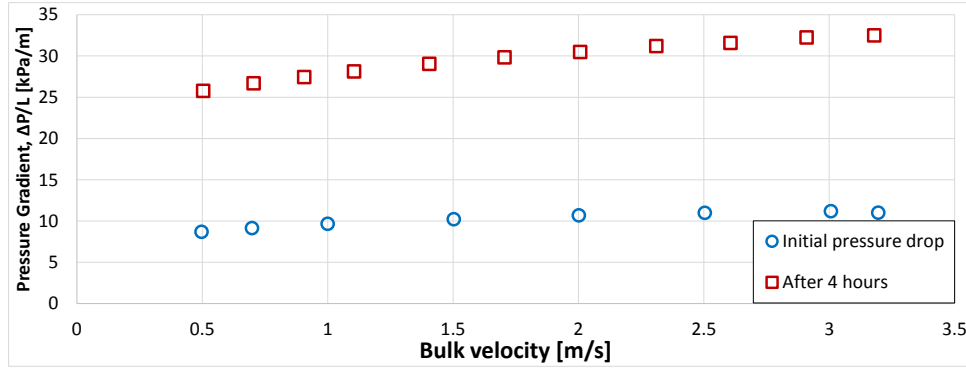


Figure E.3: Pipe loop pressure drop data. Reproduced from Litzenberger [51].

$$m_{an} = \pi [(0.0129 \text{ m})^2 - (0.0094 \text{ m})^2] (22.86 \text{ m})(1322.24 \text{ kg/m}^3)$$

$$m_{an} = 7.412 \text{ kg}$$

The total mass flow rate in the loop is:

$$\dot{m} = A_P V \rho_m$$

$$\dot{m} = (0.000524 \text{ m}^2)(3.2 \text{ m/s})(1322.24 \text{ kg/m}^2)$$

$$\dot{m} = 2.213 \text{ kg/s}$$

Lost work in the pipe loop due to frictional shearing is given by:

$$\ell_w = \frac{4\tau_w L}{\rho D_P}$$

$$\ell_w = \frac{4(70.965 \text{ Pa})(22.86 \text{ m})}{(1322.24 \text{ kg/m}^2)(0.0258 \text{ m})}$$

$$\ell_w = 190.22 \text{ J/kg}$$

The lost power due to frictional shearing can be calculated:

$$\dot{W}_l = \ell_w \dot{m}_{total}$$

$$\dot{W}_l = (190.22 \text{ J/kg})(2.213 \text{ kg/s})$$

$$\dot{W}_l = 420.96 \text{ J/s}$$

Finally since this energy is dissipated into the mass of the sheared annulus only, the energy dissipation is calculated by:

$$\varepsilon_{pipe} = \frac{\dot{W}_l}{m_{an}}$$

## E.2. DETERMINATION OF SHEARING FROM PIPE FLOW

---

$$\varepsilon_{pipe} = \frac{(420.96 \text{ J/s})}{(7.412 \text{ kg})}$$

$$\varepsilon_{pipe} = 56.79 \text{ W/kg}$$

This method was repeated at all bulk pipe loop velocities at the initial condition, and at the condition after 4 hours of loop operation. A summary of the  $\varepsilon_{HLC}$  values calculated with comparison to pipe loop frictional energy dissipation is given in [Table E.3](#).

Table E.3: Summary of calculated  $\varepsilon_{HLC}$  in comparison to pipe loop shearing.

Initial	Value
$\varepsilon_{HLC}$	43.76 W/kg
Range of $\varepsilon_{pipe}$	22.12-56.55 W/kg
Multiple of $\varepsilon_{HLC}$	0.51-1.29
After 4 hours	
$\varepsilon_{HLC}$	115.27 W/kg
Range of $\varepsilon_{pipe}$	46.82-155.18 W/kg
Multiple of $\varepsilon_{HLC}$	0.41-1.35